

Review

# Charge Carrier Processes and Optical Properties in TiO<sub>2</sub> and TiO<sub>2</sub>-Based Heterojunction Photocatalysts: A Review

Stefano Lettieri <sup>1,\*</sup>, Michele Pavone <sup>2</sup>, Ambra Fioravanti <sup>3</sup>, Luigi Santamaria Amato <sup>4</sup> and Pasqualino Maddalena <sup>5</sup>

- <sup>1</sup> Institute of Applied Sciences and Intelligent Systems “E. Caianiello”, Consiglio Nazionale delle Ricerche (CNR-ISASI), Complesso Universitario di Monte S. Angelo, Via Cupa Cintia 21, 80126 Napoli, Italy
- <sup>2</sup> Department of Chemical Sciences, University of Naples “Federico II”, Complesso Universitario di Monte S. Angelo, Via Cupa Cintia 21, 80126 Napoli, Italy; michele.pavone@unina.it
- <sup>3</sup> Institute of Science and Technology for Sustainable Energy and Mobility, Consiglio Nazionale delle Ricerche (CNR-STEMS), Via Canal Bianco 28, 44124 Ferrara, Italy; ambra.fioravanti@stems.cnr.it
- <sup>4</sup> Italian Space Agency (ASI), Space Geodesy Center “G. Colombo”, 75100 Matera, Italy; luigi.santamaria@asi.it
- <sup>5</sup> Department of Physics “E. Pancini”, University of Naples “Federico II”, Complesso Universitario di Monte S. Angelo, Via Cupa Cintia 21, 80126 Napoli, Italy; pasqualino.maddalena@unina.it
- \* Correspondence: stefano.letteri@isasi.cnr.it; Tel.: +39-081676809

**Abstract:** Photocatalysis based technologies have a key role in addressing important challenges of the ecological transition, such as environment remediation and conversion of renewable energies. Photocatalysts can in fact be used in hydrogen (H<sub>2</sub>) production (e.g., via water splitting or photo-reforming of organic substrates), CO<sub>2</sub> reduction, pollution mitigation and water or air remediation via oxidation (photodegradation) of pollutants. Titanium dioxide (TiO<sub>2</sub>) is a “benchmark” photocatalyst, thanks to many favorable characteristics. We here review the basic knowledge on the charge carrier processes that define the optical and photophysical properties of intrinsic TiO<sub>2</sub>. We describe the main characteristics and advantages of TiO<sub>2</sub> as photocatalyst, followed by a summary of historical facts about its application. Next, the dynamics of photogenerated electrons and holes is reviewed, including energy levels and trapping states, charge separation and charge recombination. A section on optical absorption and optical properties follows, including a discussion on TiO<sub>2</sub> photoluminescence and on the effect of molecular oxygen (O<sub>2</sub>) on radiative recombination. We next summarize the elementary photocatalytic processes in aqueous solution, including the photogeneration of reactive oxygen species (ROS) and the hydrogen evolution reaction. We pinpoint the TiO<sub>2</sub> limitations and possible ways to overcome them by discussing some of the “hottest” research trends toward solar hydrogen production, which are classified in two categories: (1) approaches based on the use of engineered TiO<sub>2</sub> without any cocatalysts. Discussed topics are highly-reduced “black TiO<sub>2</sub>”, grey and colored TiO<sub>2</sub>, surface-engineered anatase nanocrystals; (2) strategies based on heterojunction photocatalysts, where TiO<sub>2</sub> is electronically coupled with a different material acting as cocatalyst or as sensitizer. Examples discussed include TiO<sub>2</sub> composites or heterostructures with metals (e.g., Pt-TiO<sub>2</sub>, Au-TiO<sub>2</sub>), with other metal oxides (e.g., Cu<sub>2</sub>O, NiO, etc.), direct Z-scheme heterojunctions with g-C<sub>3</sub>N<sub>4</sub> (graphitic carbon nitride) and dye-sensitized TiO<sub>2</sub>.

**Keywords:** photocatalysis; charge lifetimes; absorption; photoluminescence; O<sub>2</sub> sensing; composite photocatalyst; charge transfer; heterostructures; hydrogen production; ecological transition



**Citation:** Lettieri, S.; Pavone, M.; Fioravanti, A.; Santamaria Amato, L.; Maddalena, P. Charge Carrier Processes and Optical Properties in TiO<sub>2</sub> and TiO<sub>2</sub>-Based Heterojunction Photocatalysts: A Review. *Materials* **2021**, *14*, 1645. <https://doi.org/10.3390/ma14071645>

Academic Editor: Juan M. Coronado

Received: 11 February 2021

Accepted: 23 March 2021

Published: 27 March 2021

**Publisher’s Note:** MDPI stays neutral with regard to jurisdictional claims in published maps and institutional affiliations.



**Copyright:** © 2021 by the authors. Licensee MDPI, Basel, Switzerland. This article is an open access article distributed under the terms and conditions of the Creative Commons Attribution (CC BY) license (<https://creativecommons.org/licenses/by/4.0/>).

## Table of Contents

1. Introduction: why TiO <sub>2</sub> ?	page 2
2. The role of TiO <sub>2</sub> among photocatalysts.	page 3
3. Historical facts.	page 7
4. Electronic properties and fundamental charge carrier processes in TiO <sub>2</sub> .	page 9
4.1. Charge trapping and electronic states.	page 9

4.2.	Electron trapping: trapping energies, nature of trap sites and time scales.	page 10
4.3.	Hole trapping: trapping energies, nature of trap sites and time scales.	page 13
5.	Optical processes, charge recombination and photoluminescence in TiO <sub>2</sub> .	page 13
5.1.	Optical absorption.	page 13
5.2.	Electron-hole recombination and photoluminescence (PL) in TiO <sub>2</sub> .	page 17
5.2.1.	Relevance of photoluminescence analysis in TiO <sub>2</sub> .	page 17
5.2.2.	Basic properties of charge carrier recombination and PL in TiO <sub>2</sub> .	page 18
5.2.3.	Anatase photoluminescence.	page 19
5.2.4.	Rutile photoluminescence.	page 22
5.3.	Interplay between photogenerated charges and molecular O <sub>2</sub> adsorption: the O <sub>2</sub> -dependent PL.	page 23
5.3.1.	O <sub>2</sub> -anatase interaction.	page 23
5.3.2.	O <sub>2</sub> -rutile interaction.	page 25
5.3.3.	Applications of O <sub>2</sub> -dependent PL of TiO <sub>2</sub> .	page 26
6.	Intrinsic TiO <sub>2</sub> as photocatalyst: mechanisms and limits.	page 28
6.1.	Basic photocatalytic processes and their characteristic times.	page 28
6.2.	Limitations of intrinsic TiO <sub>2</sub> as photocatalyst.	page 30
7.	Present and future trends for TiO <sub>2</sub> -based heterostructure photocatalysts and engineered TiO <sub>2</sub> .	page 31
7.1.	Engineered TiO <sub>2</sub> nanocrystals.	page 31
7.1.1.	Black TiO <sub>2</sub> .	page 31
7.1.2.	Facet engineered TiO <sub>2</sub> .	page 34
7.2.	TiO <sub>2</sub> -based heterojunction photocatalysts.	page 38
7.2.1.	TiO <sub>2</sub> /metal heterostructures.	page 39
7.2.2.	TiO <sub>2</sub> /metal oxide semiconductors.	page 41
7.2.3.	TiO <sub>2</sub> /g-C <sub>3</sub> N <sub>4</sub> heterostructures.	page 42
7.2.4.	Dye-sensitized TiO <sub>2</sub> .	page 44
8.	Conclusions.	page 46

## 1. Introduction: Why TiO<sub>2</sub>?

In the last three decades, titanium dioxide (TiO<sub>2</sub>, also named as titania) has been a major subject of study in materials science and technology for its functional properties and its versatility toward different applications. Hence, it can be reasonably said that TiO<sub>2</sub> is—by itself—not a “novel” material. Nevertheless, the many interests in it have neither waned nor slowed down over the past few years. Why is this?

Several answers to such a question can be given, but ultimately most of them are related to its *photocatalytic properties* and to the potentialities of photocatalytic technologies as a tool to tackle some of the most important challenges in modern society, such as environmental and energy issues. Photocatalysis finds application in important fields such as—to name some of the most important examples—CO<sub>2</sub> photoreduction [1,2], pollutant removal and pollution mitigation [3,4], hydrogen production via water splitting [5–7] or via photo-reforming of alcohols [8,9] and bactericidal activity [10–12]. Hence, *photocatalytic materials are widely regarded as keystones for addressing some major problems we will face in the near future*. Developing reliable, efficient, stable and unexpensive photocatalytic materials is thus regarded as a research field of great relevance.

TiO<sub>2</sub> is undoubtedly one of the most widely studied and exploited photocatalysts, and often considered as a sort of benchmark in the field for the reasons that will be discussed next. Some of the contemporary “hot topics” in energy conversion and in light-based transformational materials/systems involve composites based on TiO<sub>2</sub> (e.g., composites with g-C<sub>3</sub>N<sub>4</sub>, with graphene, with transition metal dichalcogenides, etc). In short, it can be stated that TiO<sub>2</sub> represents an “evergreen” photocatalyst and—most importantly—that

having a basic knowledge of the fundamental processes occurring in it is of paramount importance, especially for scientists working in the development of novel (TiO<sub>2</sub>—including) composite materials/systems.

A huge number of application-oriented papers is published every year on TiO<sub>2</sub> and on TiO<sub>2</sub>-based composites. We think that it would be unrealistic (to say the least) to set up a review aiming at covering even briefly all the state-of-art related to the practical applications of TiO<sub>2</sub>-based materials. On another hand, the importance of papers that focus on some of the *fundamental processes* that define the electronic and/or photo-physical properties of TiO<sub>2</sub> as an “intrinsic” metal-oxide semiconductor should not be underestimated, since these notions are often given for granted.

Based on these considerations, this review will be centered on *highlighting and reviewing some selected topics* for providing the reader with a *general picture of the basic electronic processes and optical properties* of TiO<sub>2</sub>. For example, photochemical and photoelectrochemical reactions on TiO<sub>2</sub> surfaces are not discussed in detail in this work, considering that excellent reviews on these topics are already available in literature [3,13–19]. Instead, we will deal with fundamental notions and processes such as the position of excited and defect states, trap states, trapping/detrapping processes, optical absorption and radiative recombination (photoluminescence) and, in general, dynamics of photo-generated carriers and their interaction with environmental oxygen, as these are the fundamental processes that ultimately affect the applicative performances of pristine and modified forms of TiO<sub>2</sub>.

The present review is organized as follows:

In Sections 2 and 3 we summarize the role of TiO<sub>2</sub> among photocatalytic materials, highlighting the pros and cons of this material with also a brief historical introduction on the early findings of TiO<sub>2</sub> photocatalytic properties.

In Section 4 we give an overview of elementary charge-carrier processes, i.e., electronic properties, in TiO<sub>2</sub>. The section focuses on single-particle properties of the charge carriers—namely energy levels, nature of the trapping states and their lifetimes. Separated discussions on electrons and holes are carried out for the sake of clarity.

Section 5 deals with optical properties and light emission (photoluminescence—shortened as PL) of TiO<sub>2</sub>, discussing why the study of such a phenomenon in controlled environment is interesting for photocatalytic materials and illustrating the dominant models and hypothesis that explain the fundamental mechanisms (i.e., radiative recombination channels) of PL in both anatase and rutile. The special case of the interplay between charge recombination and O<sub>2</sub> adsorption is discussed, this being both a scientifically intriguing topic and a potentially useful phenomenon for O<sub>2</sub> sensing.

Section 6 discusses the primary oxidation/reduction processes that define the photocatalytic behavior of TiO<sub>2</sub> and the typical kinetics and lifetimes of the different steps of typical TiO<sub>2</sub>-based photocatalytic transformations in aqueous environment.

Finally, Section 7 summarizes the paper and briefly sketches some of the most recent routes currently employed to develop functional TiO<sub>2</sub>-based materials.

## 2. The Role of TiO<sub>2</sub> among Photocatalysts

Based on the considerations made in the previous section, it is useful to start here by briefly summarizing what is meant by the term *photocatalyst* and which are the characteristics that a good photocatalyst shall exhibit.

A photocatalyst is any material that exhibits photocatalytic properties, i.e., the ability to foster and accelerate specific chemical reactions upon stimulation by light of suitable wavelength. The photocatalytic processes occur via the participation of free charges generated in the photocatalyst through quantum-mechanical transition of electrons into a mobile state via annihilation of the absorbed photons. As these free charges that diffuse toward the materials surface, they can then initiate redox reaction between reactants adsorbed at the photocatalyst surface. Hence, the “suitable” wavelengths mentioned earlier refers to wavelengths which are efficiently absorbed by the photocatalyst.

A material in which photogenerated free charge carriers (also “free carriers” for brevity) are present is not in a thermodynamically stable state: the photogenerated charges will remain in the excited (and mobile) state only for a transient amount of time (carrier lifetime) whose value ultimately depend on the probabilities associated to the various quantum-mechanical decay processes, including all possible non-radiative processes and spontaneous emission (i.e., radiative recombination or luminescence). Longer lifetimes imply greater probability that the free carrier will go into contact with the reagents and (possibly) foster a chemical reaction. From that it follows that conductors (metals) are not suitable as photocatalysts, due to their remarkably short lifetime associated to infra-band electron–electron scattering. Instead, photocatalysts of practical interest are typically semiconductors and, as a consequence, the light-induced free charge carriers involved in fostering redox reactions are electrons and holes belonging to the conduction and valence band (respectively) of the semiconductor.

The photocatalytic action involves conduction band electrons as reactant-reducing agents and valence holes as reactant-oxidizing agents, as schematically shown in Figure 1 for a generic semiconductor. The efficiency of a specific redox reaction will depend on the relative values of the conduction (or valence) band energy of the semiconductor and the reduction (or oxidation) electrode potential of the specific half-reaction, as shown schematically in the caption of Figure 1. Additional examples of the energy position of conduction and valence band edges vs. various standard half-reaction potentials are reported in Figure 2.

A quantitative condition expressing the “suitability” of the wavelengths supposed to activate a given photocatalyst refers to the comparison between the quantum-mechanical energy  $E = h\nu$  of the photon and the semiconductor bandgap  $E_g$ . The photogeneration of free charges can occur only if  $E > E_g$ , i.e.,

$$E = h\nu = \frac{hc}{\lambda} > E_g \Leftrightarrow \lambda(nm) < \frac{1240}{E_g(eV)} \quad (1)$$

The simple relation in Equation (1) uses the numerical values of the speed of light ( $c$ ) and of Planck constant ( $h$ ) and indicates the optical “activation edge” of the photocatalyst. Radiation of wavelength longer than the band-edge value of Equation (1) are not suitable to activate photocatalytic effects, unless some specific modification of the material is made to induce additional sub-bandgap optical absorption (e.g., creation of defect states and/or sensitization with a different material). Obviously, activation edges lying in the far ultraviolet (e.g., UV-A and UV-B regions) are unpractical: photocatalysts working in this optical range would require artificial light, as UV-A and UV-B are blocked by the Earth atmosphere.

Although non-oxide semiconductors (e.g., transition metal-based monochalcogenides such as CdS and ZnS) and even completely different materials such as carbon quantum dots, MXenes and g-C<sub>3</sub>N<sub>4</sub> also exhibit interesting photocatalytic properties, the most commonly employed photocatalysts are selected among metal oxides. Examples of photocatalytic metal-oxide semiconductors are represented by TiO<sub>2</sub>, ZnO, SnO<sub>2</sub>, CeO<sub>2</sub>, ZrO<sub>2</sub>, WO<sub>3</sub>, MoO<sub>3</sub>, Fe<sub>2</sub>O<sub>3</sub> and Fe<sub>2</sub>O<sub>3</sub>.

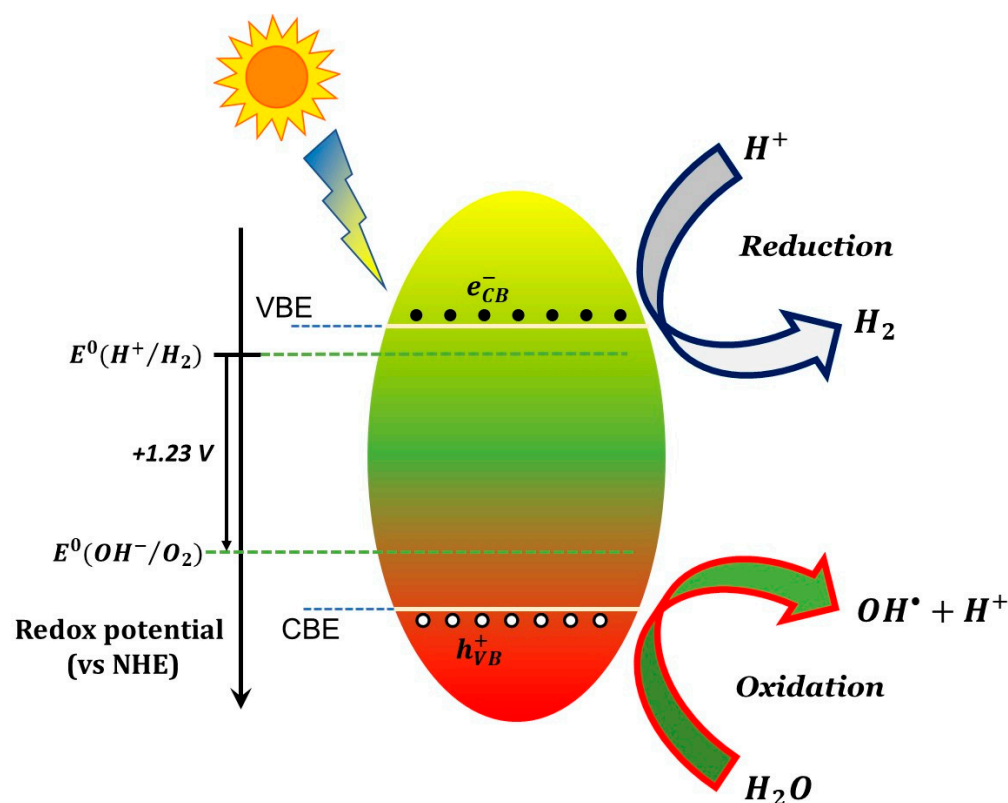


**Figure 1.** Elementary scheme for a basic photocatalytic process (here, water splitting) caused by illumination of a semiconductor photocatalyst. The scheme shows the reduction of  $H^+$  through electrons photogenerated in the conduction band and the oxidation of hydroxyl ions with formation of hydroxyl radicals through photogenerated holes in the valence band. In order for the two processes to occur the electrostatic potential associated to the conduction band edge (CBE) and valence band edge (VBE) have to be lower and greater (respectively) than the electrode potential of  $H^+ \rightarrow H_2$  and  $OH^- \rightarrow O_2$  semi-reactions. The two half-reaction potential are separated by 1.23 Volts and thus a viable photocatalyst for water splitting shall have an energy gap of at least 1.23 eV. Larger gaps are actually needed to compensate for various sources of potential losses (“overpotential”). Similar considerations can be made for other redox reactions, using the corresponding electrode potentials.

There are plenty of available reviews on the photocatalytic properties of the above-mentioned materials, and here we will just mention some of the most recent ones, including some specifically relating with  $TiO_2$ —based materials [20–23] and on other novel trends and topics of materials science for photocatalysis-related applications [24–26].

Apart from the mentioned issue of the optical activation energy, there are several other factors that can limit the photocatalytic efficiency of a semiconductor. The most important ones are:

- (1) Large electron-hole recombination rates, as they would prevent the photogenerated charges from reaching the catalyst surface where the reaction between the adsorbed reactants shall occur.
- (2) Susceptibility to photocorrosion, which decreases their photocatalytic efficiency.
- (3) Scarce versatility of the material. By “versatility” here we mean the existence of reliable technological means to process/modify the material accordingly to the practical needs. For example: tuning of bandgap energy and/or modifying the optical spectrum of the material.
- (4) Other practical issues, such as poor chemical stability, scarce biocompatibility, scarce affordability of the material synthesis/processing, etc.

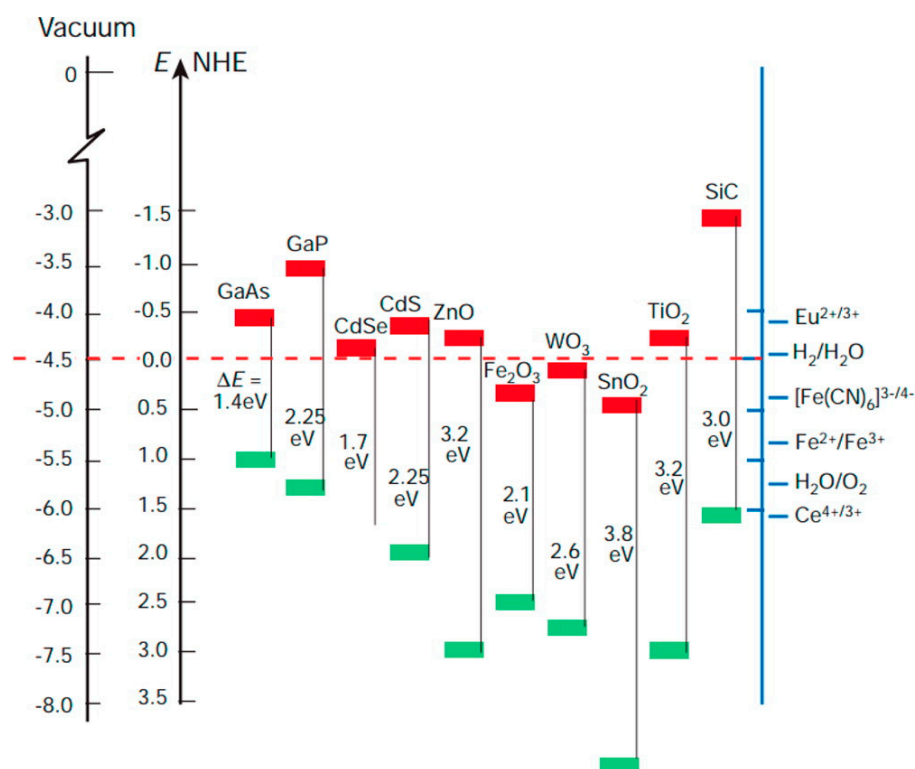


**Figure 2.** Energy position of conduction and valence band edges for selected semiconductors vs. various standard half-reaction potentials. The energy is represented in the vertical axis on the left as referenced to the vacuum level and to the normal hydrogen electrode (NHE) level. Reprinted with permission from Reference [27]. Copyright 2014 American Chemical Society.

A significant number of semiconductors have been investigated for their potential suitability as catalysts in photoelectrochemical reaction, including both oxides and non-oxides and with band gaps ranging from  $\approx 1.4$  eV (e.g., GaAs) to  $\approx 3.5$  eV (e.g., SnO<sub>2</sub> [28]). Among them, TiO<sub>2</sub> is widely studied and employed due to several reasons:

- (1) It is cost-effective, i.e., can be produced at reasonable costs also in view of large-scale uses;
- (2) It is photostable and resistant to corrosion;
- (3) It shows a satisfactorily photocatalytic efficiency (at least once UV illumination is used for undoped TiO<sub>2</sub>, as will be discussed in more detail next);
- (4) Several well-known chemical and physical techniques to produce TiO<sub>2</sub> in form of porous films and nanoparticulate powders are available and well-developed [29–37];
- (5) Finally, in recent years the problem of scarce activation by visible sunlight (that will be discussed next) has been mitigated: novel strategies of doping development of novel composites—some of which will be discussed in the present work—is allowing to obtain interesting results also in the field of visible light-activated photocatalysis.

Historically, TiO<sub>2</sub> has been widely used as pigment for paints [38–40] and for other products such as toothpastes [41] and sunscreens [42–44]. A historical breakthrough took place with the discovery of photocatalytic water splitting on a TiO<sub>2</sub> electrode illuminated by UV light [45], that brought large interest and efforts toward the scientific and technological research on titania. At the present days, the most important applications of TiO<sub>2</sub> can be roughly classified in two categories, namely environmental and energy applications. For the reasons discussed in the next sections, these applications often rely on modified forms of TiO<sub>2</sub>, some examples including doped TiO<sub>2</sub> and/or TiO<sub>2</sub>-based composites and heterostructures.

### 3. Historical Facts

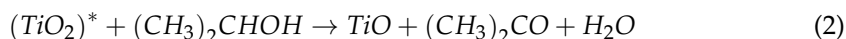
As mentioned, the interest in TiO<sub>2</sub> has been massively fostered by research in electrochemistry, and in particular by the mentioned 1972 achievement of photoelectrochemical water splitting by Fujishima and Honda [45]. It is to be noted that the position of the TiO<sub>2</sub> band edges (vs. standard hydrogen electrode) indicates that conduction band electrons are good reducing agents toward hydrogen, whereas the valence band holes are strong oxidizing agents toward water (see Figure 2). This explains the light-induced decomposition of water into oxygen and hydrogen without the application of an external bias. Before that breakthrough, the photophysical and photo-transformative properties of TiO<sub>2</sub> (and of other semiconductor metal oxides as well) had been already evidenced: here we briefly sketch an historical outline of this subject.

Titania has been used for centuries as pigment in paints. As a consequence, it has been recognized since long ago that it activates specific photochemical processes, manifesting in the “chalking” of exterior paints when exposed to intense sunlight [46,47]. By chalking it is meant here that a powder-like white substance tended to be formed and to fall away from the painting, in a fashion similar to the chalk on a blackboard. Even from this simple description we can recognize this phenomenon as a manifestation of what is today called “self-cleaning” property of TiO<sub>2</sub>. At the time, the chalking was correctly recognized as the effect of a partial removal of the organic component in the paint, leaving the TiO<sub>2</sub> exposed. For example, an earlier report by Renz in 1921 discussed how TiO<sub>2</sub> surfaces with adsorbed organic compound (such as glycerol) were partially reduced when exposed to sunlight. The reduction macroscopically manifested itself via a change in the color of titania, turning from white to grey, blue or black. Similar results were described in the same paper also for other metal oxides, such as Nb<sub>2</sub>O<sub>5</sub>, Ta<sub>2</sub>O<sub>5</sub> and CeO<sub>2</sub> [46].

Few year later, Baur and Perret reported about the photocatalytic deposition of a silver salt of ZnO to produce metallic silver [48], hypothesizing that the key element of the reaction was the photogeneration of free charges of opposite sign in ZnO that provided simultaneously oxidation of hydroxyl ions and reduction of Ag<sup>+</sup> ions, i.e.,  $ZnO + \hbar\omega \rightarrow e^- + h^+$ ,  $h^+ + OH^- \rightarrow (1/4)O_2 + (1/2)H_2O$  and  $e^- + Ag^+ \rightarrow Ag^0$ .

In 1927, the ability of photoexcited ZnO to activate redox reaction was again invoked to explain the production of H<sub>2</sub>O<sub>2</sub> from decomposition of formaldehyde [49]. Later studies on formation of metallic silver and gold confirmed that these observed processes were indeed photocatalytic reductions activated by different light-exposed metal oxides, including Nb<sub>2</sub>O<sub>5</sub> and TiO<sub>2</sub> [50]. Other evidence of the specific photocatalytic characteristics of TiO<sub>2</sub> were provided by study of photo-induced decompositions of dyes on TiO<sub>2</sub> powder [51,52].

While during the 1950s the photocatalytic oxide of major interest was considered ZnO [53,54], the research on TiO<sub>2</sub> was also developing. Kennedy and coworkers in a 1958 study on photo-adsorption of O<sub>2</sub> underlined that photoexcited electrons were transferred to O<sub>2</sub> then adsorbed as O<sub>2</sub><sup>-</sup> species on the TiO<sub>2</sub> surface [55]. Such an ability to photo-adsorb the O<sub>2</sub> was found to be correlated to the efficiency of photodecomposition of tested dye. Interestingly, some results also evidenced the possible involvement of oxygen lattice atoms of TiO<sub>2</sub> in photocatalytic reaction of organic compounds. For example, a study of the photocatalytic oxidation of isopropanol to acetone on TiO<sub>2</sub> suggested the following surface reaction [56]:



This process involves the formation of a surface oxygen vacancy, which can next be healed by dissociative adsorption of atmospheric O<sub>2</sub>, i.e.,  $TiO + (1/2)O_2 \rightarrow TiO_2$ .

The 1960s witnessed the publication of the first studies demonstrating the possibility to fully decompose (oxidize) organic compounds to water and CO<sub>2</sub> via TiO<sub>2</sub>-based photocatalysis. One example was reported in 1965 by McLintock and Ritchie, who investigated the photo-decomposition of ethylene and propylene on TiO<sub>2</sub> [57]. In the same decade, early photoelectrochemistry studies of TiO<sub>2</sub> by Fujishima triggered interest as they evidenced that gaseous O<sub>2</sub> could be evolved at electrode potentials referred vs. standard hydrogen

electrode (“SHE”) quite shifted with respect to the expected values. For example, the experimental onset for  $O_2$  evolution obtained at about  $-0.25$  V (vs. SHE) compared to the standard potential of  $+0.95$  V in pH 4.7 aqueous buffer [58] indicated that the energy conversion (from photon energy to chemical energy) in  $TiO_2$  occurred with small losses, so that the photogenerated holes could react directly with water (according to the water photooxidation semi-reaction  $2h^+ + H_2O \rightarrow (1/2)O_2 + 2H^+$ ).

After the mentioned work of 1972 in which Fujishima and Honda reported about the ability to simultaneously generate hydrogen in a photoelectrochemical reactor (i.e., to achieve full water splitting), the field of photoelectrochemistry received a significant boost in attention and paved the way for the role of  $TiO_2$  in energy-based applications.

We conclude this brief overview by also mentioning earlier reports on “environmental” applications. Works published 1977 by Frank and Bard studied the photocatalytic oxidation of cyanide and sulfite to cyanate and sulfate provided by photocatalytic activity of some semiconductor metal oxides, namely:  $TiO_2$ ,  $ZnO$ ,  $Fe_2O_3$  and  $WO_3$  [59,60]. An example of their experimental findings is reported in Figure 3, showing the data for the reaction of cyanide in aqueous solution due to photooxidation caused by anatase  $TiO_2$  [59]. The authors hence proposed the use of these photocatalyst for remediation of water via photo-induced decomposition of pollutants and focused in particular of photo-assisted oxidation of a number of organic and inorganic chemicals by polycrystalline  $TiO_2$  electrodes [61]. Since then, the non-selective oxidation of organic compounds/pollutants for water and air remediation is still an active field of study, as demonstrated by review papers published up to recent years. For example, we cite References [62–65] for water remediation and References [66–68] for air remediation.

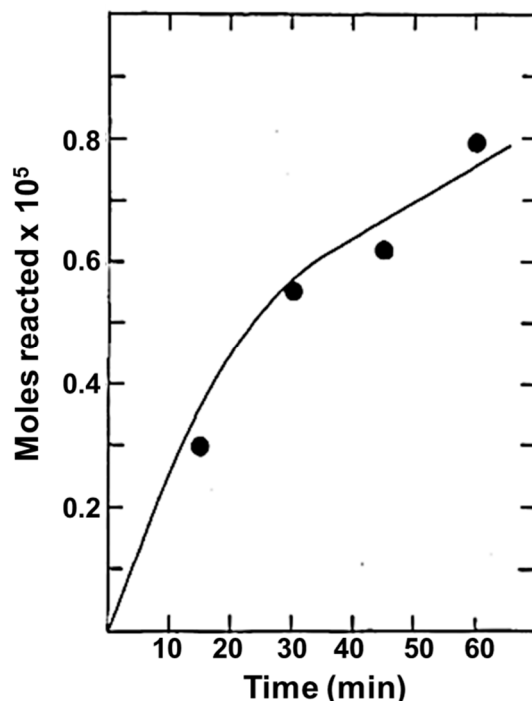


**Figure 3.** Number of moles of  $CN^-$  that reacted after irradiation of an aqueous solution 1 mM  $CN^-$  0.1 M  $KOH$  with a xenon lamp while bubbling  $O_2$ . Adapted with permission from Reference [59]. Copyright 1977, American Chemical Society.

The photodegradation of pollutants by  $TiO_2$  photocatalytic action typically requires the use of ultraviolet light. The practical experience demonstrated that the intensity of UV light present in the sunlight is typically non-sufficient to transform large quantities of organic compounds, and hence a medium/large scale application of the technology is somehow problematic. Such a limitation has oriented nowadays efforts and applications toward some specific directions. For example, attention has turned to cases in which a small

UV intensity is enough to carry a limited amounts of reactions at the titania surface such as, for example, the anti-bacterial disinfection of  $\text{TiO}_2$ —treated surfaces [69]. An obvious consequence of this limitation is that much research efforts are focused on developing  $\text{TiO}_2$ —based photocatalysts that can be activated by visible light, as will be discussed next.

#### 4. Electronic Properties and Fundamental Charge Carrier Processes in $\text{TiO}_2$

Titania is in most cases found (or synthesized) in either anatase or rutile phase. Anatase is a meta-stable phase which irreversibly convert to rutile at temperatures larger than  $600\text{ }^\circ\text{C}$ , while the rutile phase is thermodynamically stable. Anatase is the most active photocatalytic phase, a fact typically attributed to larger concentrations of surface hydroxyl and hence to an improved (compared to rutile) generation of  $\text{HO}^\bullet$  and  $\text{H}_2\text{O}_2$  species [70]. It is worth mentioning that another meta-stable phase exists, namely brookite whose photocatalytic properties have not been investigated in much detail [71–73]. In the rest of Section 4 we will sometimes use the abbreviations A- $\text{TiO}_2$  (or just “A”) and R- $\text{TiO}_2$  (or just “R”) to indicate the  $\text{TiO}_2$  anatase and rutile phase (respectively). Some of the bulk properties of the two polymorphs are reported in Table 1, which reports data taken from the Oxide Handbook by Samsonov [74], unless noted otherwise.

**Table 1.** Bulk properties of rutile and anatase  $\text{TiO}_2$ .

Atomic Radius (nm)			Density ( $\text{g}/\text{cm}^3$ )		
O:	0.066 (covalent)		Rutile	4.24	
Ti:	0.146 (metallic)		Anatase	3.83	
	Ionic radius (nm)		Brookite	4.17	
O (−2)	0.14 nm				
Ti (+4)	0.064 nm				
Crystal structure			Lattice constants (nm)		
System		Space group	a	b	c
Rutile	Tetragonal	P42/mnm (group #136)	0.4584	-	0.2953
Anatase	Tetragonal	I41/amd (group #141)	0.3733	-	0.937
Brookite	Orthorhombic	Pbca (group #61)	0.5436	0.9166	0.5135
Energy bandgap (eV)		Electron mobility $m$ ( $\text{cm}^2/\text{Vs}$ )	Dielectric constant (at room T)		
Rutile	3.0 (indirect)	Rutile: ~1 (Reference [75])		Frequency (Hz)	Value
Anatase	3.2 (indirect)	Anatase: ~10 (Reference [75])	Rutile, $\perp \hat{c}$	108	86
			Rutile, $\parallel \hat{c}$	104	160
				108	170
				107	100

##### 4.1. Charge Trapping and Electronic States

The absorption of photons whose energy is at least equal to the bandgap of the semiconductor induces to the creation of a pair of “free” (i.e., mobile) charges in the valence (a hole) and in the conduction band (an electron) of the semiconductor. Next, the fate of the free charges (and, in particular, whether they can reach the semiconductor surface or not) depends on the probability of recombination and of charge trapping processes. Both of these processes typically depend on the morphology and on the defect configuration (i.e., the type and the concentration of the defects) of the semiconductor nanoparticle.

Charge trapping indicates a generic process of electronic relaxation toward a localized state, typically belonging to the bandgap region of the semiconductor. Once trapped, the charge is of course no longer mobile. The trapped electrons (or holes) whose energy distance to the edge of the conduction (of valence) band is close to  $k_B T$  (where  $k_B$  is the Boltzmann constant and  $T$  is the temperature) can also be detrapped, that is they can return to a mobile state and continue to move in the crystal. The trapping process is however not reversible if it occurs into a deep trap, i.e., when charges are trapped in sites associated to

electron states whose energy distance from the band edges is much larger than  $k_B T$ . In such a case, the most likely fate of these charges is to recombine non-radiatively. For this reason, deep traps are often referred to as recombination centers.

The charge mobility of a semiconductor is clearly a crucial parameter in order to assess its efficiency as photocatalyst. The reactants are in fact typically present as adsorbed species on the semiconductor surface, and redox processes can occur only when started (triggered) by a charge that reached the surface. Based on what we said about the trap states, it can be broadly said that the presence of deep charge traps is detrimental to its photocatalytic efficiency. However, to assume this as broadly valid statement would be simplistic. For example, trapping could be also considered beneficial when it localizes charge carriers at sites which are preferential for the adsorption of potential reactants, or if promotes charge separation.

#### 4.2. Electron Trapping: Trapping Energies, Nature of Trap Sites and Time Scales

Electron trapping is quite important for  $\text{TiO}_2$  photophysics. In fact, most of the photogenerated electrons are expected to be already trapped long before they initiate a reduction reaction. As discussed in Section 6, in fact, the timescale for electron trapping is of the order of few nanoseconds.

Studies involving direct and/or indirect measurements or the binding energy of shallow and deep electron traps in  $\text{TiO}_2$  report values in an energy range between 0.1 and 0.8 eV [76–83], consistent with photoemission results for electronic defects on the surface of  $\text{TiO}_2$  single crystal surfaces [15].

For example, Leytner and coworkers [76] employed a time-resolved version of photoacoustic spectroscopy to study colloidal  $\text{TiO}_2$  nanocrystals in aqueous solutions, finding evidence of electron traps states, available to photoexcited conduction electrons, whose energy levels lie below approximately 0.8 eV below the conduction band edge, as shown in Figure 4. In this work the decay of trapped electrons to the valence band was estimated to occur with a lifetime of about 25–30 ns and an average photon energy of  $3.2 - 0.8 = 2.4$  eV, in good agreement with the experimental finding for the “green” photoluminescence of anatase, discussed in Section 5.2.3.

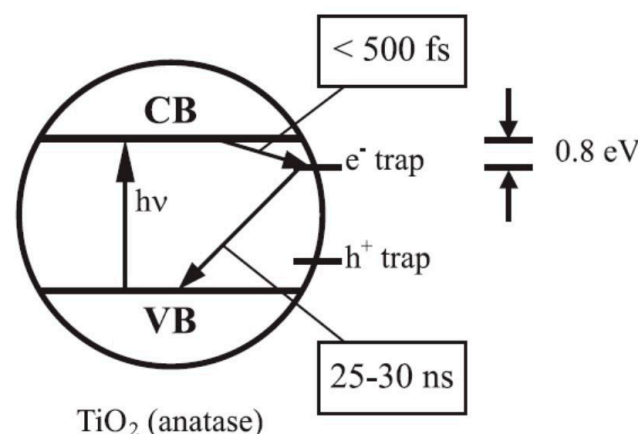


**Figure 4.** The scheme proposed for the dynamics of photogenerated electrons by Leytner and Hupp, according to the results of their time-resolved photoacoustic spectroscopy experiments. The free electrons are trapped via a fast process in states which are found to have an average energy 0.8 eV below the conduction band edge, so that they shall be considered deep traps. While the position of traps is in good accord with photoluminescence experiments, the lifetime of such trapping process was estimated to be less than 1 ns, in partial disagreement with the scheme proposed by Hoffman and coauthors [84] (discussed in Section 6.1) which associated processes of such rapidity to shallow traps. Reprinted from Reference [76] with permission from Elsevier. Copyright 2000 Elsevier Science B.V.

It is worth noting that other works evidence the presence of surface states at the contact between TiO<sub>2</sub> (rutile, generally) electrodes and electrolyte solution. Earlier analyses conducted by Siripala and Tomkiewicz [77] on the photocurrent induced by sub-bandgap illumination of single-crystal TiO<sub>2</sub> electrodes in milder acidic conditions (pH = 6.5) evidenced electron promotion from the valence band to gap states lying around 0.6 eV below the bottom of the conduction band. Since then, several works evidenced comparable results regarding the energy of the infra-gap traps and surface states. For example, surface states positioned at an energy 0.7 eV below the conduction band edge in TiO<sub>2</sub> in nanocrystalline TiO<sub>2</sub> electrode in acidic conditions (pH = 3) were reported by Redmond and coworkers [78], while Boschloo and coauthors evidenced surface states of nanostructured anatase TiO<sub>2</sub> via spectroelectrochemical methods located about 0.5 eV below the conduction band edge [79,80].

Other works highlighted the presence of shallow traps also. Experiments by Warren and coworkers [82] conducted in controlled atmosphere on dry TiO<sub>2</sub> indicated that the de-hydrated powders produced a broad infrared spectrum peaked at 880 cm<sup>-1</sup>, attributed to shallow traps present at 0.1 eV below the conduction band (see Figure 5).

To summarize, traps states are typically found within an interval of energies, in most cases reported to be centered at about 0.5–0.7 eV for the deep traps and 0.1 eV for the shallow traps. As origin of the dispersion of the allowed trap energies the heterogeneity of trap sites is often invoked [85–88]. Many researchers also agree that electrons are preferentially trapped at the surfaces for both anatase and rutile TiO<sub>2</sub> [81,83,87–94].

Although less often mentioned, surface OH groups have also been proposed as alternative trapping sites of photoexcited electrons. For example, this was proposed by Szczepankiewicz and coauthors [95], based on Fourier transform infrared (FTIR) experiments. The same possibility has also been mentioned by Henderson and coworkers for single-crystal rutile [96,97]. However, also bulk (i.e., internal) sites [98–102] and grain boundaries of sintered films [103] have been reported as possible trap sites for electrons.

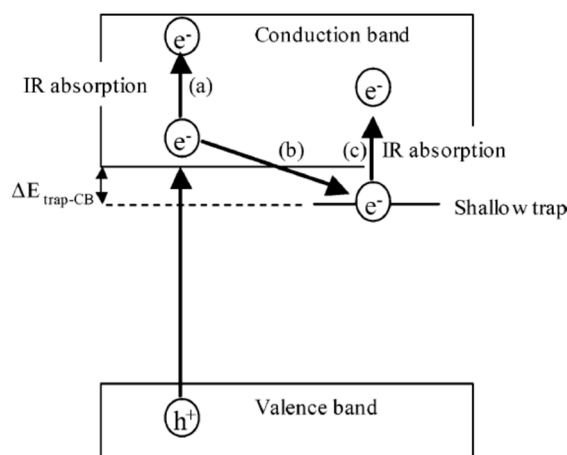


**Figure 5.** Processes identified by infrared spectroscopy in Reference [82] on Degussa P25 TiO<sub>2</sub> after the removal of adsorbed water. Spectroscopic analysis of the excitation of electrons trapped in shallow traps (process (c) in figure) provides an energy distance of about 0.1 eV between the conduction band and the trap states. Reprinted with permission from Reference [82]. Copyright 2004 American Chemical Society.

As the oxidation state of Ti in a stoichiometric TiO<sub>2</sub> crystal is 4+ (indicated as Ti<sup>4+</sup> or Ti(IV)), a Ti<sup>3+</sup> site is synonymous of an electronic excess, which might arise from the trapping of a photoexcited electron (i.e.,  $e_{CB}^- + Ti^{4+} \rightarrow Ti^{3+}$ ) or to the coordination of the Ti spaces with an oxygen vacancy (V<sub>O</sub>), which are typically associated to localized electronic charge. While it is generally true that a neutral OV accommodates electrons (two in the case of a V<sub>O</sub> in TiO<sub>2</sub>), the question of their actual degree of localization (in other words, the spatial extent of their orbital) depends on the actual strength of the ionic

bonding and interactions vs the possibility of the crystal to lower its energy by relaxing in a much different bonding configuration [104].

It might be tempting to assume that the degree of localization of an electron trapped at a  $\text{Ti}^{3+}$  site trapped charge could be estimated by adsorbing on the surface an electron-scavenging species (e.g.,  $\text{O}_2$ ) and observing whether their reaction occurs or not as a function of the distance between the surface and the trap center. However, the degree of electronic delocalization around the trap site could be sufficient to allow an electronic coupling with the surface  $\text{O}_2$  species even when the trap is not at the surface. For example, Wendt and coworkers performed this kind of analysis for rutile  $\text{TiO}_2$  via scanning tunnel microscopy (STM) measurements, arguing that even sub-surface charge associated with  $\text{Ti}^{3+}$  interstitial sites can interact with ambient  $\text{O}_2$  molecules and promoting their dissociative adsorption [105]. In conclusion, it is probably fair to state that the depth at which electrons trapped at  $\text{Ti}^{3+}$  sites can no longer participate in surface chemistry is not known. As a consequence, there is no easy way to assess whether an electron trap close to the surface but not at the surface (i.e., a sub-surface trap) is beneficial or not for the photocatalytic activity.

As mentioned previously, the photo-reduction processes such as the formation of superoxide radicals (Equation (7)) are expected to be mostly caused by trapped electrons. In fact, many studies concur that the trapping of a photogenerated occurs on a sub-picosecond time scale and possibly shorter than 100 fs [98,106], while instead its detrapping typically occurs on a much longer timescale.

More in detail, experimental studies indicate that the lifetimes of a trapped electron in  $\text{TiO}_2$  have a large variability [81,95,107–111] depending on the eventual presence (or absence) of electron scavengers (e.g.,  $\text{O}_2$ ) and/or hole scavengers.

Trapped electron lifetimes spanning over timescales from hundreds of picoseconds [81] to tenths of microseconds [112] in “non-perturbed”  $\text{TiO}_2$ , while they can be noticeably much longer if a hole scavenger (such as ethanol) removes the possible recombination partners of the trapped electrons. An example is reported in Figure 6 (reprinted from Ref. [112]) whose authors performed transient absorption spectroscopy on commercial P25 and P90 nanocrystalline films (the latter has greater anatase content and smaller particles than the former). The optical absorption at 800 nm ( $\sim 1.55$  eV) was used as a probe of the excitation of trapped electrons, while ethanol was used as hole scavenger. As shown in Figure, in absence of both ethanol and oxygen a lifetime of about 25  $\mu\text{s}$ , while in presence of ethanol the lifetime increased of a factor of six order of magnitudes ( $\sim 0.5$  s).

Moreover, it has also been reported that under ultra-high vacuum conditions (that is, the best controlled conditions to exclude the intervention of any charge scavenger), localized electronic charge associated to  $\text{Ti}^{3+}$  sites on single crystal  $\text{TiO}_2$  surfaces can persist indefinitely [15].

The ability to durably store trapped electrons at a given concentration is an important characteristic for defining the photocatalytic efficiency of a catalyst. In the case of nanoparticulated  $\text{TiO}_2$ , an early study indicated that up to about 10% of the  $\text{Ti}^{4+}$  sites could be occupied by a trapped electron if EtOH was used as hole scavenger to reduce the probability of electron-hole recombination [113]. The results of this study were later strengthened by other findings indicating trapping capacity in the range of 7–14% [109,114,115]. In terms of electron densities of surface traps, values have been found in literature as ranging in a typical interval of  $10^{12}$  to  $10^{13}$   $\text{cm}^{-2}$ . For example, Wang and coworkers [116] reported surface concentrations of trapped electrons varying as a function of the pH from about  $5 \times 10^{11}$   $\text{cm}^{-2}$  at pH = 4.7 to about  $5 \times 10^{13}$   $\text{cm}^{-2}$  at pH = 13. These values are consistent with that of  $\sim 3 \times 10^{12}$   $\text{cm}^{-2}$  reported by Boschloo [80]. It is not completely clear whether the density of trapped electrons is correlated with the specific surface area. For example, Katoh and coworkers [117] showed that  $\text{TiO}_2$  particles of 20 nm diameter trapped more electrons per unit surface than particles of 300 nm diameter. However, this conclusion is challenged by other experimental findings [81].

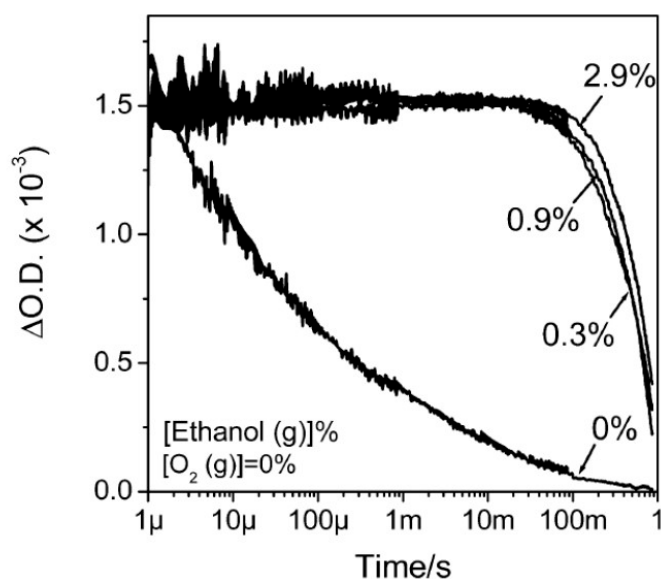


**Figure 6.** Time-resolved transient absorption signal at probe wavelength 800 nm for TiO<sub>2</sub> nanocrystals in anaerobic conditions. The percentages indicate the concentrations of ethanol (ranging from 0 to 2.9%). Pump (excitation) wavelength at 337 nm. Reprinted from Reference [112]. Copyright 2006 American Chemical Society.

#### 4.3. Hole Trapping: Trapping Energies, Nature of Trap Sites and Time Scales

Theoretical predictions based on electrostatic calculations [118] on hole and electron trapping at the TiO<sub>2</sub>(110) surface of rutile indicated near-surface sites as the preferred to bulk sites for hole trapping in rutile TiO<sub>2</sub>, a conclusion that is consistent with results by Shapovalov et al. [119] using an ab initio embedded cluster approach. Experimental investigations on the sites of hole trapping have often employed electron paramagnetic resonance (EPR). A consensus exists on the fact that the most likely trap sites are surface undercoordinated surface atoms (i.e., Ti<sup>4+</sup>-O surface terminations) [120–123].

Concerning the time dynamics of hole trapping, investigations indicate that on TiO<sub>2</sub> surface it occurs at about the same rate as electron trapping. For example, one analysis [124] conducted via transient absorption spectroscopy in anatase particles estimated a hole trapping time of about 50 fs, while other works report hole trapping timescale of ~200 fs for ‘hot’ holes resulting from band-to-band excitation [125,126], followed by thermalization over about successive 0.1 ns.

Other works worth mentioning are those from Furube’s group in which transient absorption spectroscopy (in combination with the use of methanol as a scavenger) was employed to track the hole trapping in nanocrystalline films of A-TiO<sub>2</sub> [126,127]. These authors assigned the spectral region at ~500 nm to excitation events associated with trapped holes, similarly as Yang and Tamai [124] who observed a broad transient absorption signal at ~520 nm evolving immediately on excitation of colloidal A with a 200 fs 360 nm pulsed laser source. This absorption was assigned to excitation of trapped holes because it was not observed if the hole scavenger SCN<sup>−</sup> was present. Interestingly, this absorption is very close in photon energy to the transitions correlated to the “green photoluminescence”, discussed later in Section 5.2.3, which are also attributed to trapped holes.

## 5. Optical Processes, Charge Recombination and Photoluminescence in TiO<sub>2</sub>

### 5.1. Optical Absorption

A-TiO<sub>2</sub> and R-TiO<sub>2</sub> are both transparent in the visible and near-infrared range, with a transmission interval of about  $\Delta\lambda = 0.4\text{--}7\ \mu\text{m}$  and birefringent, as they belong to the tetragonal system. The rutile has positive birefringence, meaning that its extraordinary refractive index is larger than its ordinary index. It exhibits an index difference  $\Delta n = n_e - n_o$

of about 0.27–0.29 in the visible range (see Figure 7). On the other hand, anatase shows a negative birefringence.

The refractive properties of R-TiO<sub>2</sub> have been investigated in some detail, as it serves in practical applications. Specifically, R-TiO<sub>2</sub> is commercially available as large crystals of good optical quality and large refractive indexes. As shown by the m-lines measurements by Rams and coworkers [128], the extraordinary refractive index  $n_E$  of R-TiO<sub>2</sub> in the wavelength interval  $\Delta\lambda = 1350 - 450$  nm varies from (about)  $n_E(1350 \text{ nm}) \approx 2.70$  to  $n_E(450 \text{ nm}) \approx 3.13$ , while for the ordinary index  $n_O$  we get  $n_O(1350 \text{ nm}) \approx 2.45$  and  $n_O(450 \text{ nm}) \approx 2.80$  (Figure 8).

Due to such a large refractive index, rutile prisms are often used in optical laboratories to couple the light into optical waveguides. This requires a precise knowledge of its refractive and thermo-optical coefficients. An earlier work by Devore (Ref. [129]) is also quite useful in estimate the dispersive refractive indexes of R-TiO<sub>2</sub>, as they provide a good extrapolation using a Sellmaier equation of the form:

$$n_k^2(\lambda) = A_k + \frac{B_k}{\lambda^2 - C_k} \quad (3)$$

where the suffix “k” indicates either ordinary or extraordinary wave. The best-fit values for the coefficients A, B and C are reported to be  $A_e = 7.197$ ,  $B_e = 0.3322$  and  $C_e = 0.0843$  for the extraordinary wave and  $A_o = 5.913$ ,  $B_o = 0.2441$  and  $C_e = 0.0803$  for the ordinary wave [129].

Measurements of dispersive refractive index of anatase are less available [130], probably due to the difficulty of preparing good quality anatase crystals and to the fact that anatase is actually much more useful and employed in form of nanoparticle films and powders due to its superior (respect to R-TiO<sub>2</sub>) photocatalytic properties.

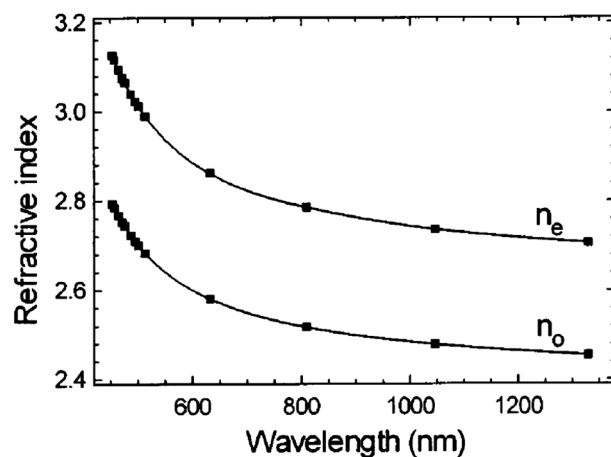


**Figure 7.** Experimental values of the ordinary ( $n_o$ ) and extraordinary ( $n_e$ ) refractive index of rutile TiO<sub>2</sub> crystals as a function of wavelength at temperature  $T = 30$  °C. The continuous curves are calculated via a Sellmeier-like interpolation. Reprinted with permission from Reference [128]. Copyright 1997 American Institute of Physics.

Figure 8 reports experimental values of the refractive index ( $n$ ) and extinction coefficient ( $k$ ) in the UV-visible range obtained via spectroscopic ellipsometry for amorphous and nanocrystalline thin TiO<sub>2</sub> films grown at different substrate temperatures ( $T_S$ ) on Si(100) substrates via Atomic Layer Deposition [131]. The data indicated refractive index values increasing from amorphous ( $T_S \leq 150$  °C) to nanocrystalline films  $250$  °C  $< T_S \leq 400$  °C. All measurements evidence in a clear way the negligible occurrence of optical absorption in the visible range.

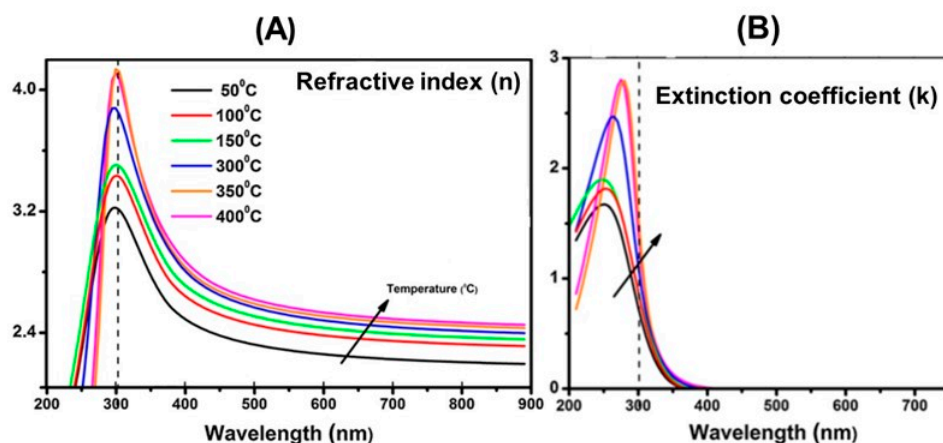


**Figure 8.** Plots of refractive index (A) and extinction coefficient (B) of amorphous TiO<sub>2</sub> films (grown at 50, 100 and 150 °C) and of nanocrystalline TiO<sub>2</sub> films (grown at 300, 350 and 400 °C) films. The black arrow indicates the increase of *n* and *k* with increasing growth temperature. In all cases it is clearly evidenced the absence of optical absorption for wavelengths larger than 400 nm. Reprinted from Reference [131] with permission from Elsevier. Copyright 2014 Elsevier Science B.V.

The bulk optical absorption properties of A and R have been studied in the past in great detail [130,132–138]. Their importance is underlined by the fact that they represent the first step (i.e., the photogeneration of free charges) of the photocatalytic process. The optical absorption spectra of the two main polymorphs of TiO<sub>2</sub> have been obtained by different techniques, including photoacoustic spectroscopy [76] and photoconductivity [134,139].

As also indicated in Table 1, the optical absorption edges (i.e., bandgap energies) of A and R occur at room temperature at photon energies of about 3.2 eV and 3.0 eV, respectively [140]. The photon energy values of optical absorption edges increase as the temperature of the crystals is decreased for both polymorphs [135]. It is generally held that they bandgaps in bulk R and A are direct and indirect, respectively. The threshold for the first direct bandgap transition in A is reported to be at ~3.8–4.0 eV [141,142]. In this same range (i.e., ~4.0 eV) the maxima of the bulk optical absorption spectra of both polymorphs also occur [143,144]. A detailed study of the optical absorption behavior of anatase TiO<sub>2</sub> at photon energy lower than absorption edge has been conducted by Tang and coworkers [134,136], who showed (see Figure 9) that the absorption coefficient exhibits a Urbach tail, i.e., a spectral region in which it increases exponentially vs. increasing photon energy [145] at all temperatures.

The same authors studied the dichroic behavior (i.e., the difference in the absorption properties perpendicular to versus parallel to the *c*-axis) of the two phases, showing that it increases with temperature in anatase, while disappears in R while approaching room T [136]. A possible interpretation of this effect was provided by a first-principles calculation indicating that non-bonding *dxy* orbitals preferentially oriented perpendicular to the *c*-axis are present at the bottom of the anatase CB, contributing to its anisotropic optical absorption [146].

Observation of quantum-size effects (quantum confinement) in the absorption spectra of ultra-small TiO<sub>2</sub> nanoparticles is controversial. Works have been published reporting both the occurrence [147] and the absence of quantum confinement effect [148,149]. For example, a blueshifts in the absorption threshold of anatase TiO<sub>2</sub> as a function of decreasing particles sizes below 2 nm was reported by Satoh and coworkers [147], who stated that the experimental results matched their calculations based on the effective mass approximation. On another hand, no bandgap shift for anatase nanoparticles of diameters down to 2 nm was evidenced by Serpone and coworkers [148], who suggested that absorption edge blueshifts observed for anatase nanoparticles below 2 nm diameter shall be assigned to a transition from an indirect to direct bandgap excitation, an effect caused by geometric distortions of Ti coordination occurring when anatase particles became ultra-small.

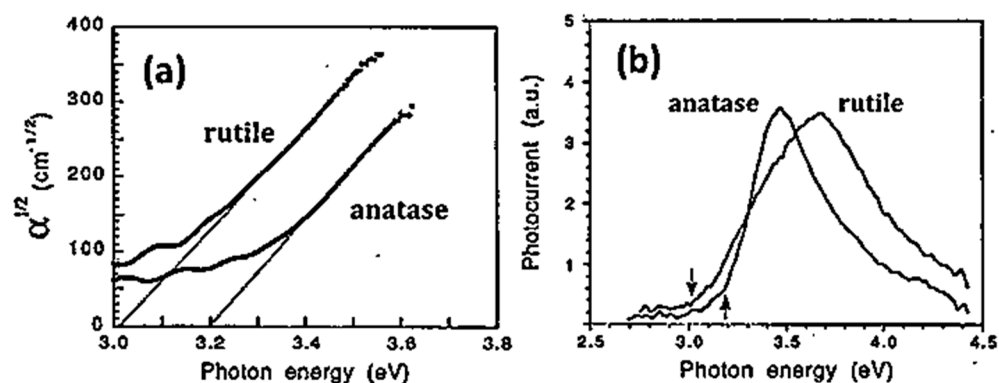


**Figure 9.** (a) Optical absorption spectra of anatase and rutile films measured at room temperature and plotted as  $\alpha^{1/2}$  ( $\text{cm}^{-1/2}$  units) vs. photon energy (eV units). The graph evidences the different indirect bandgap energy of the two polymorphs. (b) Photoconductivity spectra of anatase and rutile films. The arrows indicate the optical absorption edges. The anatase sample evidences a broader energy distribution of shallow donors in the sub-bandgap region. Adapted from Reference [134] with permission from Elsevier. Copyright 1994 Elsevier Science B.V.

Monticone and coworkers [149] also examined the optical properties of small anatase nanoparticles of different particle size distribution, observing little or no blueshift for particles with diameters from 3 nm down to 1 nm (see Figure 10). The data did not fit the effective mass approximation and did not support the occurrence of quantum size effect in  $\text{TiO}_2$  nanoparticles. Moreover, the same authors observed changes in the oscillator strengths of optical transitions in the 3.5–4.5 eV range with decreasing particle, which they did not attribute to quantum size effects but to increased lattice strain in the particles.

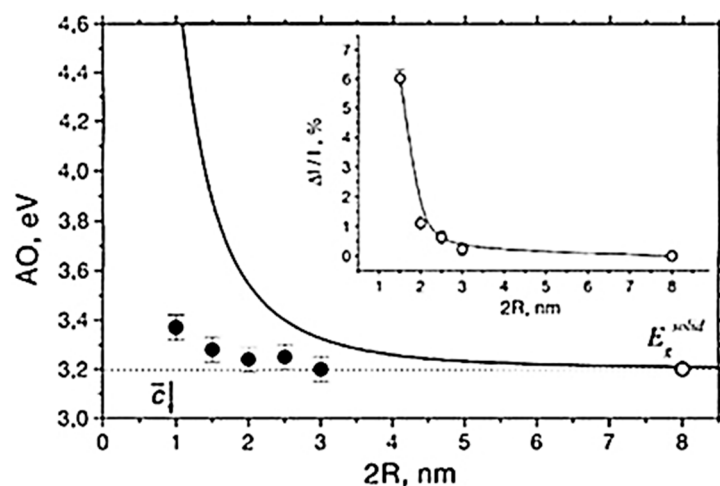


**Figure 10.** Absorption onset energy of colloidal  $\text{TiO}_2$  nanoparticles of different diameters (3, 2.5, 1.5 and 1 nm). The solid line is a theoretical calibration curve based on effective mass approximation. The inset reports relative changes of the (101) lattice constant calculated by XRD spectra. Reprinted from Reference [149] with permission from Elsevier. Copyright 2000 Elsevier Science B.V.

It is known that multilayered structures that alternate low and high refractive index layers can be engineered to form efficient reflectors [150], whose optical properties are mainly dictated by the periodicity of the optical thickness of the layers and on the refractive index differences between low and high index layers. Thanks to its large refractive index and to the variety of techniques allowing to process and micro-engineering  $\text{TiO}_2$  structures, multilayered reflectors [151] (Figure 11) and, more in general,  $\text{TiO}_2$ -based three-dimensional photonic crystals have been fabricated and investigated, proving to be useful in different ways. For example, photonic resonances can be used to localize the

electromagnetic energy at specific frequencies (“slow light” effect) in the high-refractive index photocatalyst and enhance the photoinduced, as schematically shown in Figure 12. Activation enhanced hydrogen production in photoelectrochemical cells was reported by Chiarello and coworkers [152] using a  $\text{TiO}_2$  photonic crystal as photoanode.

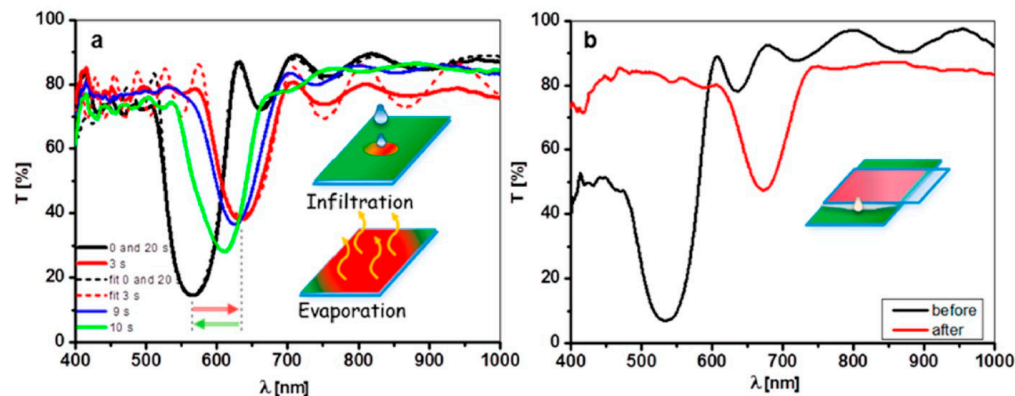


**Figure 11.** Example of the spectral reflectivity and chemical sensing capabilities of a 1D photonic crystal (multilayered reflector) obtained by stacking thin layer of controlled thickness and porosity by pulsed laser deposition. (a) Measurements of transmission spectra of the  $\text{TiO}_2$  photonic crystal before and after infiltration with acetone. The transmission measurements are modified due to the modification of the refractive index caused by infiltration of acetone the pores, followed by its evaporation. (b) Modification of the transmission spectrum caused by infiltration with a liquid crystal. Reprinted with permission from Reference [151]. Copyright 2014 American Chemical Society.

Applications of  $\text{TiO}_2$  in chemical sensing, SERS detection and photocatalysis have been reviewed in Refs. [23,153–155].

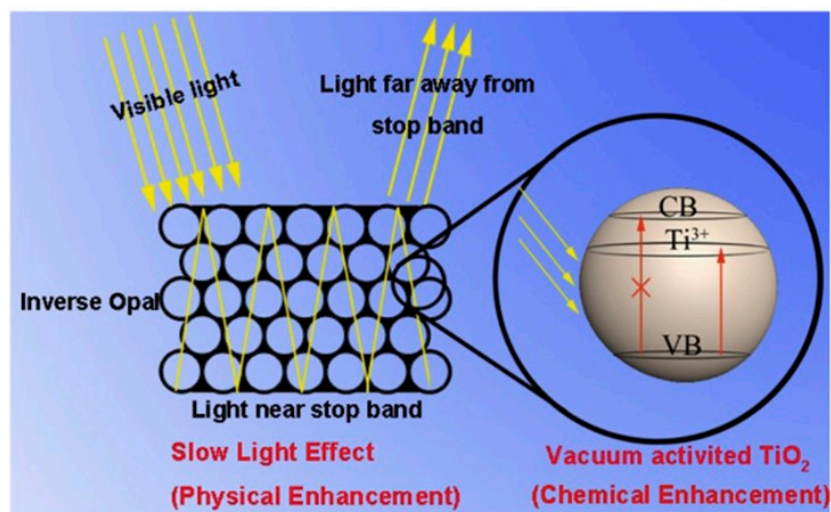


**Figure 12.** Illustration of the synergistic effect of the photonic resonances in an inverted-opal  $\text{TiO}_2$  photonic crystal and its photocatalytic activity. The off-resonance light is mostly reflected away, while the light belonging to the photonic stop-band is slowed down (“slow light effect”) and optical modes with larger intensity on the photocatalyst (the high-index regions) are formed leading to an efficient excitation of the photocatalyst. Reprinted from Reference [156] with permission from Elsevier. Copyright 2014 Elsevier B.V.

## 5.2. Electron-Hole Recombination and Photoluminescence (PL) in $\text{TiO}_2$

### 5.2.1. Relevance of Photoluminescence Analysis in $\text{TiO}_2$

In the context of studies of a catalytic material it is of paramount importance to gather information on the active surface sites of the catalyst and on how they affect the dynamics

of adsorption and photoactivated transformations of the targeted species. In this regard, studies of PL properties of the catalyst in controlled environment and during a reaction are very well suited and useful.

PL phenomena in semiconductors are driven by diffusion and recombination of photo-generated charges, that typically occurs in a thin region beneath the semiconductor surface (typical widths of few tenths of nm if the excitation is provided at supra-gap photon energy), making it very sensitive to small local variations. Even if PL is not intrinsically surface-selective as special techniques such as surface second harmonic generation [157–160], it has the advantage that it is usually not difficult to obtain a fairly good signal-to-noise ratio, furthermore in absence of background signal that are present in other optical spectroscopy techniques (e.g., reflectivity).

Moreover, PL techniques involve lifetime measurements and allows dynamic analysis during the reactions (i.e., while the catalyst is in contact with the reactant and as the pressure of the reactant is changed in a controlled manner). Finally, as already mentioned in the previous section, the PL efficiency gives indications on the lifetimes of charge carriers and therefore it usually correlates with the photocatalytic efficiency.

As mentioned, M. Anpo and coworkers were among the first who systematically employed photoluminescence as one of the standard techniques of study of photocatalytic materials and of the redox transformations occurring on their surfaces [161–165]. Since then, PL has been often employed as an indirect test to assess the usefulness of modifications of a material (for example, of heterogeneous doping), as a dramatic quenching of the PL signal would typically indicate an improvement in the photocatalytic properties.

#### 5.2.2. Basic Properties of Charge Carrier Recombination and PL in TiO<sub>2</sub>

Recombination represents the conclusive process for photogenerated electrons and holes. The excess (with respect to equilibrium) energy associated to the excited free charge carriers can be dissipated via emission of a photon (radiative recombination) or by other mechanisms (non-radiative recombination). Radiative recombination events manifest themselves at the macroscopic scale as photoluminescence (PL), while non-radiative events mostly transfer energy to the lattice vibration modes and thus manifest themselves at the macroscale via heat production.

Recombination efficiency is of course a very important parameter of a photocatalyst, as it correlates inversely with the photo-transformative efficiency. Therefore, techniques devoted to the study of recombination efficiency and timescales are of primary importance for TiO<sub>2</sub> studies. It is well established that the only contribution to photoluminescence in a semiconductor that can occur at a relevant intensity is the band-to-band recombination in crystals with direct bandgap, where the opposite charge carriers can recombine directly in a first-order radiative transition, i.e., with emission of photons whose energy is approximately equal to the bandgap energy (with variability of the order of the thermal energy  $k_B T$ ) [166]. TiO<sub>2</sub> has an indirect band-edge configuration and hence its PL emission occurs at wavelengths longer than the bandgap wavelength: that is, the PL of TiO<sub>2</sub> is not caused by band-to-band transitions but involves localized states. As a consequence, it is easily understood why the TiO<sub>2</sub> PL is typically quite weak and why it is ordinarily assumed that the vast majority of electron-hole recombination in this material occurs by non-radiative processes.

Achieving a direct detection of non-radiative recombination events is typically difficult, and actual estimations of non-radiative yields and lifetimes usually rely on indirect determination (such as for example evaluation of generated heat) [76].

On another hand, the radiative transition events can be directly detected by continuous-wave photoluminescence (CW-PL). Experimental setups suitable to compare in a quantitatively accurate manner the PL intensity from an investigated material and from a reference chemical species (e.g., a solution of some luminophore molecules) allows the determination of the PL quantum yield of the material under investigation. This is the quantity that more accurately (and directly) allows to estimate the actual proportion between radiative vs.

non-radiative efficiency. The few available reports of PL quantum yield ( $\eta$ ) measurements confirm this statement. In fact, typical values for  $\eta$  in various forms of  $\text{TiO}_2$  gives values of the order of  $\sim 0.1$  to 1% [167–171] confirming the general idea that the vast majority of electron-hole recombination in  $\text{TiO}_2$  is non-radiative.

Analysis conducted by CW-PL are important also for other reasons. Consider for instance the Lambert–Beer law, which states that the amount of electromagnetic intensity  $I(z)$  which is not extinct via optical absorption after travelling inside the material for a length  $z$  is given by  $I(z) = I_0 \exp[-\alpha(\omega)z]$ , where  $\alpha$  is the absorption coefficient. As typical values for the absorption coefficients at optical frequencies in  $\text{TiO}_2$  range in the order of  $\sim 10^5 \text{ cm}^{-1}$ , we deduce that most of the photogenerated charges occurs within a region whose depth below the semiconductor surface has a typical value of few tenths of nanometers [172]. Therefore, the PL characteristics (e.g., spectrum, intensity, lifetime) are very sensitive to molecular adsorption and to surface chemical reactions, which are decisive factors for characterizing the behavior of the photocatalyst. As a consequence, since the previously-mentioned studies by Anpo and coworkers [161–165] PL has been regarded as an important tool for studying photocatalytic materials and surface properties [85,90,173–182].

A very peculiar characteristic of  $\text{TiO}_2$  PL is that its A and R phases exhibit different and well-separated bands, where anatase typically shows a broad emission in the visible spectrum (VIS-PL) peaked at  $\sim 500$ – $530 \text{ nm}$  while rutile shows a narrow spectrum peaked in the near-IR (NIR-PL, peaked at  $\sim 820 \text{ nm}$ ) [183]. The electronic processes and the nature of the different states responsible for such a difference are not completely elucidated.

### 5.2.3. Anatase Photoluminescence

Regarding the origin of the anatase VIS-PL, two different hypotheses have gained greater consensus in recent decades, the first attributing is to the radiative recombination of self-trapped excitons and the second instead invoking free-to-bound radiative transitions, that is transition from defective (trap) states to band states or vice-versa.

Self-trapped excitons have been extensively invoked in early papers, based on the fact that the strong coupling between charges and crystal lattice field (i.e., electron-phonon interaction) typical of an ionic crystal can lead to a rearrangement of the local bond geometry associated to a relaxation of the exciton energy. The self-trapping of excitons is analogous to the self-localization of free charges as small polarons in ionic solids and has been observed in different alkali halides and large-bandgap oxides [184,185]. Some works interpreted the VIS-PL emission in anatase as the radiative dissociation of self-trapped excitons. According to this explanation, the more distorted Ti-O octahedral geometry of anatase (respect to rutile) favors the self-trapping of excitons, while instead excitons in rutile are free.

This interpretation leaves some question unanswered. For example, it is not clear why the emission originating from the recombination of free excitons in rutile is not observed and it is not explained why rutile emits light in the near-IR. Moreover, the self-trapped exciton interpretation seems problematic in relation to the more recent investigations on anatase PL emission under below-bandgap excitation (i.e., in conditions where the excitons cannot be formed) [186,187].

Successive works [83,90,188–190] instead argued in favor of the concurrence of two emission bands in anatase PL, caused by free-to-bound transitions (i.e., recombination of a free carrier and a trapped carrier). These transitions are typically centered at photon energies of (about) 2.4 and 1.9 eV [186], corresponding to respectively the green and the red region of the visible spectrum (hence hereafter named as “green” and “red” PL). These emission bands are observed simultaneously, so that they invariably give rise to the previously-mentioned broad “VIS-PL”, but careful studies of the interplay between these emission bands and the presence of external chemical species adsorbed on anatase surfaces conducted by the McHale group [83,182,191,192] and the Lettieri group [186,193,194] suggested the non-equivalence of these two PL contributions, i.e., that they are governed by different underlying mechanisms.

In this regard, Pallotti et al. evidenced the physical non-equivalence of the red and green PL via experiments on anatase/O<sub>2</sub> (gas) interactions and by using PL excitation (PLE) spectroscopy technique [186]. In particular, PLE experiments allowed to show that the green component of the PL is dominant for supragap excitation ( $\lambda_{exc} < 387$  nm), while subgap excitation also induces a PL emission which is anyway shifted toward the red part of the spectrum.

A considerable number of findings [195–204] indicates that exposure to O<sub>2</sub> quenches the PL intensity of a semiconductor: Such O<sub>2</sub>-induced quenching of the photoluminescence is quite naturally interpreted as the consequence of the scavenging of photogenerated free electrons in the CB (conduction band) operated by the oxygen molecules while adsorbing on the anatase surface. This charge-capture process is clearly competitive with the relaxation and/or radiative recombination of the photogenerated electron. Therefore, it quenches the PL emission that originates starting from free electrons.

The O<sub>2</sub>-induced quenching of PL is easily observed in anatase TiO<sub>2</sub> and is particularly prominent for the “high energy side” (i.e., green PL) of the emission spectrum. An example of this is shown in Figure 13.

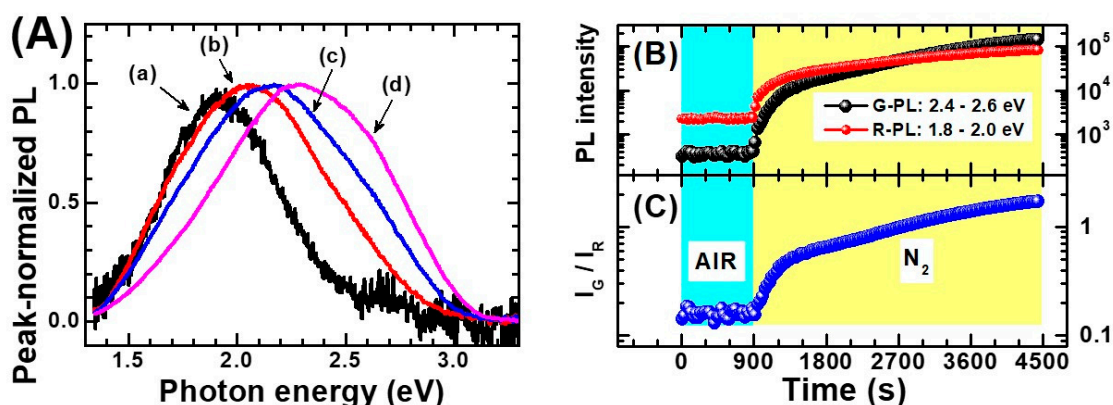


**Figure 13.** (A) Peak-normalized photoluminescence (PL) spectra of commercial anatase NPs measured after 900 s exposure to dry air (curve (a)) and after 600 s, 1500 s and 3600 s (curves (b), (c) and (d), respectively) of exposure to dry N<sub>2</sub> flow. The progressive shift toward shorter wavelengths of the PL spectrum indicates that the quenching effect exerted by O<sub>2</sub> is more pronounced on the “green” component (G-PL) of the photoluminescence spectrum of anatase. (B) PL intensity vs. time integrated in the photon energy intervals of 2.4–2.6 eV (G-PL, black dots) and 1.8–2.0 eV (R-PL, red dots). (C) Ratio between the G-PL and R-PL intensities vs. time. The increase of this ratio is another way to indicate the larger sensitivity of the green PL to the O<sub>2</sub> desorption. The exposure to different gaseous atmospheres is represented by differently colored backgrounds: Cyan: air, yellow: N<sub>2</sub>. G-PL and R-PL state for green PL and red PL, respectively.

Based on the beforementioned studies by the McHale group and Lettieri group on TiO<sub>2</sub> photoluminescence, a scheme for the totality of recombination processes in anatase and rutile can be proposed and schematically shown in Figure 14 for anatase (for additional details see Reference [186]). It has to be underlined that, at the present date, a global consensus on the overall configuration of processes that are involved in TiO<sub>2</sub> PL is still not present. Hence, the detailed mechanisms discussed in caption of the Figures 14 and 15 shall therefore be considered as reasonable hypothesis, even if most of the argumentations appear to be pretty solid.

The following points regarding the A-TiO<sub>2</sub> photoluminescence appear to be most experimentally established and the soundest from an interpretative point of view:

- (1) Non-equivalent recombination processes characterize anatase PL and lead to two spectrally separated contributions in the “green” and in the “red” part of the visible spectrum (i.e., centered at about 520 and 650 nm).
- (2) The overall anatase PL (i.e., both their spectral contribution) are subject to intensity quenching when the surface is exposed to O<sub>2</sub>. However, the “green” contribution is more sensitive than the “red”.

- (3) The excitation spectrum of anatase TiO<sub>2</sub> follows the interband absorption curve. However, additional PL emission is still present at sub-bandgap excitation conditions [188], in particular when the titania has been subjected to reductive treatments [207]. This evidence indicates that the anatase PL is not exclusively caused by self-trapped exciton recombination, as stated in several earlier papers (this point has been mentioned at the beginning of the present subsection)

Based on the above points, a mechanistic picture of the PL processes of A-TiO<sub>2</sub> can be proposed as represented in the next figure, involving two population of trapped charge-carriers. The first consists of trapped holes that can recombine with free electrons. Given that this transition is the one sensitive to electron scavengers and based on the available data on O<sub>2</sub>-induced quenching of A-TiO<sub>2</sub> PL, the same transition is likely to be associated to the green emission.

The second population of trapped charges that hence shall be assigned to the “red PL” and consists of trapped electrons which are deeply trapped and hence less likely to be chemisorbed by O<sub>2</sub>. However, some PL quenching is also expected due the development of a depletion region (see Section 5.3.1 for a discussion on this point). Moreover, some of the trapped electrons may originate from photogenerated electrons (see processes “f” and “g” in Figure 15) and they can be chemisorbed due to O<sub>2</sub> exposure.

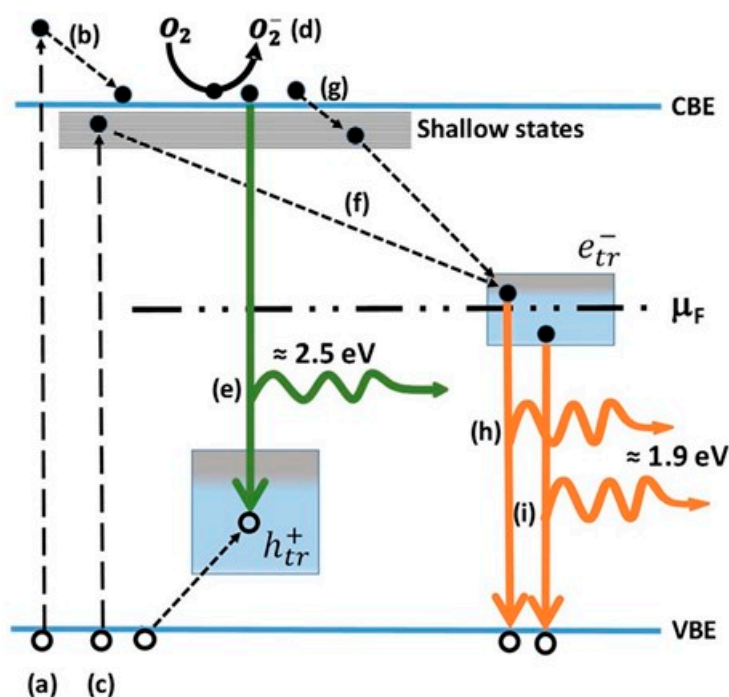


**Figure 14.** Schematic of the anatase PL mechanisms: (a) photo-excitation of charge carriers (electrons and holes) via absorption of UV light; (b) electron relaxation (thermalization) in the conduction band; (c) excitation of band-tail states (shallow states) via absorption of below-bandgap light; (d) scavenging of free electrons by O<sub>2</sub>; (e) radiative decay of conduction band electrons in electron traps with emission of “green” PL; (f,g) non-radiative decay of donor-like electrons (from shallow states) and free electrons (from the conduction band) to trap states; (h,i) radiative decay of trapped electrons to valence band, with emission of “red” PL peaked at about 1.9 eV. In this scheme this latter emission can be caused by either radiative recombination of electron in trap states to the valence band (mechanism “h”) or by radiative recombination of photogenerated holes with electrons in trap states below the Fermi level  $\mu_F$  (these latter states can be already occupied before the laser excitation). Reprinted with permission from Reference [186]. Copyright 2017 American Chemical Society.

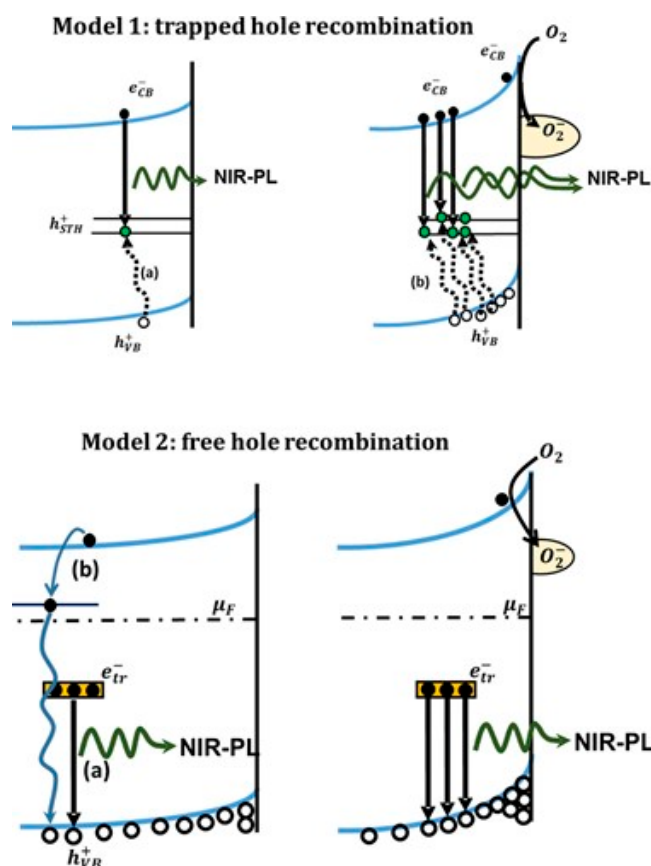


**Figure 15.** The “Model 1” (scheme on top of the Figure) is based on the hypothesis that the rutile PL is initiated by a self-trapped photogenerated hole close to a 3-fold coordinated O atom, which gains energy with respect to bulk holes and then recombines radiatively with a conduction band electron. This mechanism could explain the enhancement of the rutile PL caused by  $O_2$  adsorption, as the adsorbed superoxide ions bends upward the valence band and then helps accumulating holes near the surface. In the scheme below (“Model 2”) the near-infrared PL of rutile instead involves free holes and electrons trapped in mid-gap states below the Fermi level (which are already occupied in dark conditions), as shown by mechanism “a” in lower left. In this case, the enhancement of near-IR PL caused by  $O_2$  can be interpreted as the consequence of a different competition for the recombination of the photogenerated holes in the valence band. In presence of  $O_2$  more free electrons are scavenged (while those already in the trap states in dark condition are not affected by the adsorbed  $O_2$ ) and thus there is less competition for the recombination with the photogenerated holes. Reprinted with permission from Reference [186]. Copyright 2017 American Chemical Society.

#### 5.2.4. Rutile Photoluminescence

Interpreting the origin of the rutile NIR-PL is more difficult, for the reasons discussed here. Before starting the discussion, we point out the evidence that appear to be experimentally established:

- (1) Rutile NIR-PL occurs at with a peak energy typically included in the wavelength interval 820–850 nm. While room temperature measurements typically display a single peak, some reports resolve different contributions (for example Reference [206])
- (2) The PLE analyses indicate that the rutile PL is clearly initiated by free carriers only, as no NIR-PL emission at sub-gap excitation is observed.
- (3) Exposing the rutile to  $O_2$  enhances its PL (contrary to the case of anatase).

Concerning the NIR-PL emission of rutile, a general scheme that has been carried forward in several works by Y. Nakata and coworkers [207–209] attributes the NIR-PL to the decay of conduction electron with “self-trapped holes”, as schematized as “model 1” in Figure 15.

Another interpretation regarding the origin of the NIR-PL was proposed by Santara and coworkers [210], who stated that it has to attributed to recombination of electrons trapped at interstitial Ti sites close to the surface. The authors based this statement on PL studies of intrinsic mixed-phase TiO<sub>2</sub> nanoribbons (exhibiting different mixed phases, depending on the temperature of the solvothermal assembling process), corroborated by EPR and XPS analyses. It is to be noted that the attribution of NIR-PL to recombination of electrons trapped near interstitial Ti atoms appears to be incompatible with the before-mentioned “self-trapped holes” scheme.

The same authors suggested that the NIR-PL is not an intrinsic property rutile phase only. Instead, it might be simply observed prevalently in rutile because the rutile phase is usually produced by carrying out a heat treatment of anatase phase that conceivably activates the migration of intrinsic defects from the bulk to the surface. Among them, the interstitial Ti sites (including both Ti<sup>4+</sup> and Ti<sup>3+</sup>) also migrate toward the surface and their larger surface density (in comparison to the anatase one) might account for the NIR-PL.

Finally, it is worth noting that NIR-PL emission has been evidenced also in the TiO<sub>2</sub>(B) phase (brookite titania) as shown by Vequizo and coworkers [210]. In the latter work, the authors observed that methanol vapor quenched both the visible and NIR emissions of TiO<sub>2</sub>(B) due to the hole-consuming reaction of methanol (a known hole scavenger), while O<sub>2</sub> quenched the visible emission and enhanced the NIR emission, as also observed (as previously mentioned) for anatase and rutile phases. The authors interpreted the data stating that the NIR-PL is caused by the radiative recombination of electrons deeply trapped in surface sites at energies close to the mid-gap level and valence band holes.

It is to be noted that in Reference [210] the chemical nature of the sites that trap deeply the electrons is not specified, but this hypothesis looks compatible with that of Reference [206] which assign these sites to interstitial Ti.

### 5.3. Interplay between Photogenerated Charges and Molecular O<sub>2</sub> Adsorption: The O<sub>2</sub>-Dependent PL

In this section we underline the peculiar phenomena occurring to PL intensity of TiO<sub>2</sub> exposed to molecular oxygen (O<sub>2</sub>), as evidenced in relatively recent studies. The main feature here appears to be that TiO<sub>2</sub> has not a unique response to O<sub>2</sub> adsorption. More precisely: exposure to O<sub>2</sub> can induce either PL enhancement or PL quenching in anatase, while several reports (as discussed previously) also indicate that O<sub>2</sub> induces PL enhancement in rutile near-infrared (NIR) PL.

In most cases, O<sub>2</sub> act as a reversible scavenger of photoexcited electrons, causing a PL decrease (quenching) that can be caused by two concurrent effects, namely (i): the trapping of charges which are hence no more available to the radiative recombination (see for example Figure 14), and (ii): an increased upward bending of the energy bands below the surface, causing an enlargement of electron-depleted region and hence a decrease in the spatial overlap between holes and electrons, ultimately leading to a lesser rate for their recombination within the excitation volume. Therefore, it is—generally speaking—quite unusual and puzzling to observe an O<sub>2</sub>-induced enhancement of PL.

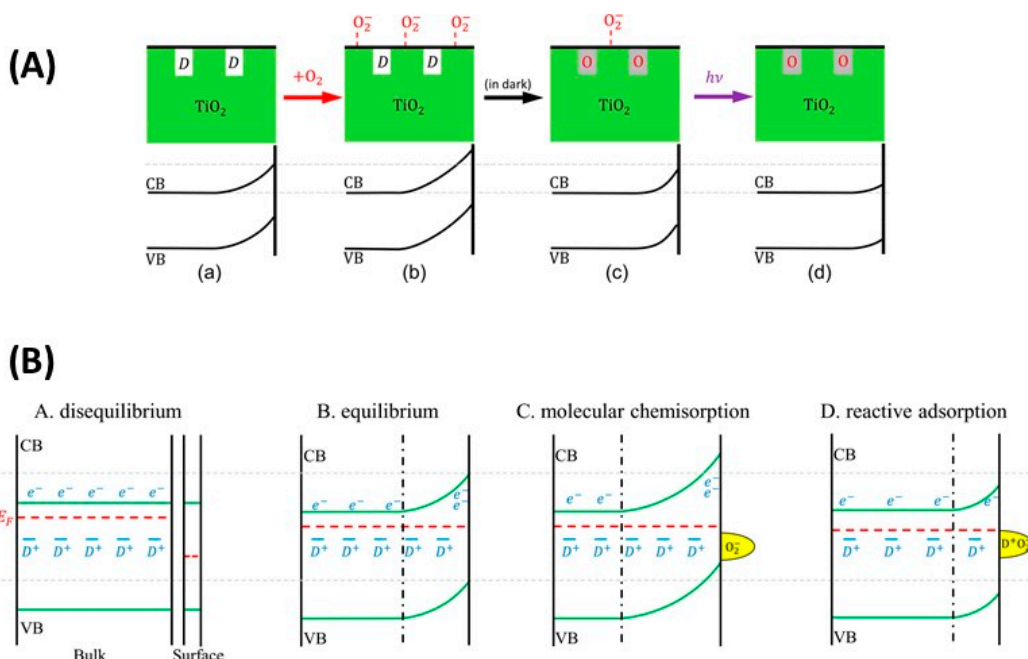
#### 5.3.1. O<sub>2</sub>—Anatase Interaction

The interplay between anatase PL and O<sub>2</sub> adsorption was studied in detail by Ma and coworkers [211], who proposed that the occurrence of either PL enhancement or PL quenching are basically related to opposite modifications of the surface potential (or, equivalently, the band bending toward the surface). As mentioned, the regions where upward band bending occur are partially depleted of mobile electrons and hence characterized by a lesser degree of spatial overlap between opposite charge carriers which is a necessary condition for the radiative recombination to occur. Hence, that any increase in the band bending is associated to a decrease in the region that can produce photoluminescence.

The fact that O<sub>2</sub> could alter the TiO<sub>2</sub> band bending in two different ways was attributed to the occurrence of two possible O<sub>2</sub> adsorption processes, one characterized by O<sub>2</sub>/defect reactions leading to a drop in the surface potential (and PL enhancement) and another

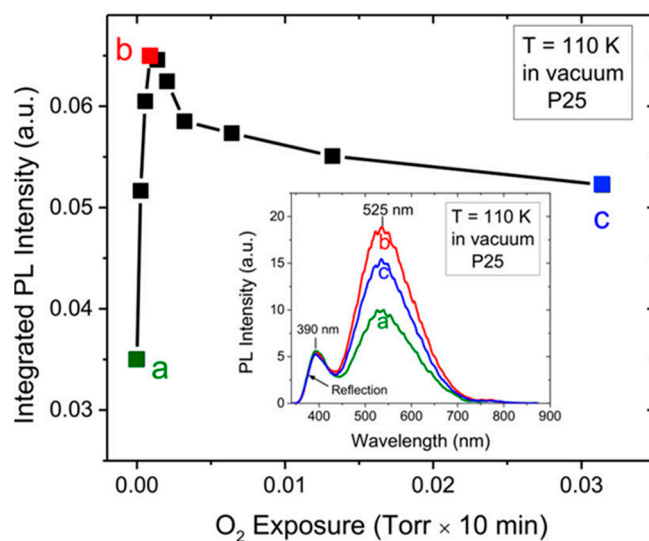
in which oxygen remains as chemisorbed superoxide ions on the surface, increasing the band bending and decreasing the PL intensity. Such a double possibility is schematized in Figure 16. Figure 16A shows the possible dynamics of the band bending, increasing due to the presence of chemisorbed charged molecular species (scheme b) and decreasing if due a reaction between molecular charged species and defects occurs in dark (scheme c), eventually followed by further lowering of the band bending and hence to increase of the PL intensity in by UV excitation in vacuum (scheme d).

Figure 16B (lower figure) also shows a possible interpretation of the actual process that leads to the variations of the band bending, involving an oxygen-defect ( $D^+$  in the scheme) reactive adsorption active reaction that lowers the surface charge and hence the band bending [211].



**Figure 16.** (A) Scheme for the two possible modification of the surface band bending of  $\text{TiO}_2$  induced by exposure to  $\text{O}_2$ . The configurations (b) and (d) are associated to the lowest and highest PL intensity, respectively. (B) Interplay between adsorbed  $\text{O}_2$  and intrinsic defects of  $\text{TiO}_2$  as proposed by Ma and coworkers as the processes capable to modulate the PL intensity. The configuration shown in scheme D (labelled as “reactive adsorption”) is characterized by the presence of a neutral species, resulting from reaction between molecular oxygen and surface donor-type defects. According to the data shown in Figure 16, this latter mechanism is active only for low  $\text{O}_2$  exposures. Reprinted with permission from Reference [211]. Copyright 2017 American Chemical Society.

An example of opposite behavior induced by  $\text{O}_2$  is shown in Figure 17 where the PL in vacuum conditions is measured after exposures at different  $\text{O}_2$  pressures. The data were interpreted by hypothesizing that the  $\text{O}_2$  adsorption at low exposures preferentially occurred via reaction with surface defects (schematized Figure 16b as “reactive adsorption”), thus leading to the observed PL increase (regions a,b in the Figure 17). On the contrary, at increasing  $\text{O}_2$  exposure the population of available defects decreased and the reactions with defects were saturated, so that the additional  $\text{O}_2$  occurred as chemisorbed  $\text{O}_2^-$  ions causing the decrease of PL intensity (observed from point b to point c in Figure 17).



**Figure 17.** Effect of O<sub>2</sub> exposure on the PL of P25 TiO<sub>2</sub>. The spectra were measured in post-exposure mode, that is: the TiO<sub>2</sub> sample in the measurement chamber was exposed for 10 min to a pre-selected O<sub>2</sub> pressure in dark, followed by chamber evacuation for 5 min and finally by acquisition of the PL spectra (obtained for 320 nm excitation wavelength). The spectra shown in the inset correspond to PL spectra acquired after a 10 min exposure to O<sub>2</sub> pressures of (a): 0 Torr (i.e., high vacuum), (b):  $9 \times 10^{-4}$  Torr and (c):  $3 \times 10^{-2}$  Torr. All spectra were acquired at chamber temperature of 110 K. Reprinted with permission from Reference [211]. Copyright 2017 American Chemical Society.

### 5.3.2. O<sub>2</sub>—Rutile Interaction

As mentioned, one of the first interpretation for the origin of NIR-PL emission of rutile involved the idea of a radiative recombination between conduction electrons and “self-trapped holes” [207–209], also schematized as “model 1” in Figure 15. This model has a problematic element in the fact that, due to its electron-scavenging activity, adsorbed O<sub>2</sub> favors the accumulation of mobile holes toward the surface and (equivalently) “pushes” mobile electron towards the bulk (hence increase the upward band-bending at the surface, as also shown in Figure 16). Therefore, the “self-trapped hole” model is compatible with the observed NIR-PL enhancement caused by O<sub>2</sub> only if these trapped holes have a low mobility and are present also extend also in the bulk. However, this is a problematic point as the self-trapped holes are believed to be formed mainly at the rutile surface [207–209].

We now consider the model that attributes NIR-PL to interstitial Ti defects: is it compatible with the observed NIR-PL enhancement by O<sub>2</sub> exposure? Concerning this point, Santara et al. [206] pointed out that some reoxidation experiments on reduced rutile TiO<sub>2</sub> crystals exposed to O<sub>2</sub> at high temperature evidenced the surfacing of Ti interstitial that were previously buried below the surface [212]. This phenomenon was suggested as an interpretation of NIR-PL enhancement under O<sub>2</sub> exposure, once assumed that surface interstitial Ti species cause the NIR PL.

However, it can be argued that this interpretation is problematic in the sense that surfacing of Ti species is likely to be caused by the temperature increase and not by the exposure to O<sub>2</sub> itself. As a matter of fact, the reoxidation process described by Onishi and coworkers [212] in which partially reduced Ti<sup>3+</sup> ions accumulated in interstitial positions were oxidized at the surface has been observed for surfaces heated at 800 K, while all the experimental evidence indicate that NIR-PL enhancement of rutile (and of brookite, see Reference [210]) occurs at room temperature.

It is our opinion that the attribution of NIR-PL to surface Ti interstitial defects is not problematic in itself, as the enhancement in O<sub>2</sub> might occur simply because the adsorbed O<sub>2</sub> accumulates valence band holes close to the surface and then increase the overlap between the recombining charges. However, to the best of our knowledge it is still not

completely clear why the same defects are not found in anatase phase. Additional in-depth analysis is probably still necessary to answer the question about the physical origin of the NIR-PL.

### 5.3.3. Applications of O<sub>2</sub>-Dependent PL of TiO<sub>2</sub>

In principle, the sensitivity of TiO<sub>2</sub> PL to molecular oxygen could be employed for oxygen sensing by detecting the modification of PL intensity. However, it has to be underlined that any detection approach based on the measurement of luminescence intensity is liable to errors. In fact, an absolute measurement of PL intensity is by definition not expressed in comparison to a proper reference value which might be for example the excitation intensity or—equivalently—any “secondary” intensity signal proportional to the excitation intensity. As a consequence, fluctuations in the intensity of excitation light will introduce an uncertainty in the experimental data which can be troublesome (in particular if the intention is to use the system to perform real-time monitoring).

One way to circumvent this technical issue involves the use of a ratiometric detection, i.e., detecting two PL intensities, both proportional to the excitation intensity but one being insensitive to the analyte while the second being sensitive to it. Hence, the ratio between the two signals will cancel out uncertainties caused only by a fluctuation in the excitation intensity.

It is interesting to mention that a similar concept can be implemented for mixed phase TiO<sub>2</sub> due to the fact that the PL of the rutile and of the anatase forms react differently to O<sub>2</sub> exposure under UV illumination conditions. This peculiarity of TiO<sub>2</sub> has been indeed exploited in Reference [213], showing that by using a mixture of rutile and anatase nanoparticles the sensitivity of the O<sub>2</sub>-induced PL changes can be increased significantly—in comparison with the one obtainable by single-phase nanopowders—using the ratio (rutile PL/anatase PL) as the parameter that signal the presence of O<sub>2</sub>. That leads to a “ratiometric” responsivity:

$$R = 1 - \frac{\phi_{NIR}^0 \phi_{VIS}}{\phi_{NIR} \phi_{VIS}} \quad (4)$$

which is by construction larger than the one obtainable using single-phase titania (for the demonstration see Reference [213]). In Equation (4) “NIR” and “VIS” refer to the near-infrared PL of rutile and to the visible PL of anatase (respectively), while  $\phi^0$  and  $\phi$  are the PL intensity in absence and in presence of O<sub>2</sub>, respectively.

An example of this concept is shown in Figure 18, that shows the dynamical (i.e., time-dependent) PL response of the mixed-phase titania toward different O<sub>2</sub> pressures under UV excitation at 325 nm. The graphs evidence the anti-correlated behavior of the two PL bands. From the PL curves, the effective response ratiometric response defined by Equation (4) and obtained from the data shown in Figure 18a are reported in Figure 18b and compared to the response curves which are obtained from single-phase titania.

It is worth underlining that the modulation of TiO<sub>2</sub> PL intensity can be very large, relatively to the typical values that are usually observed for other metal oxides exposed to gas analytes. As an example, Reference [34] reported changes in PL intensity in hierarchical anatase-phase titania [151] with responsivities up to about 1100% at 20% O<sub>2</sub> concentrations, which outperformed those obtainable by commercial TiO<sub>2</sub> nanopowders up to a factor of about 7 for response to synthetic air (see Figure 19).

These values are remarkable, when compared to some of the experimental findings reported in literature on PL-based opto-chemical gas sensing using other metal oxides (see Reference [34] and supporting information therein).

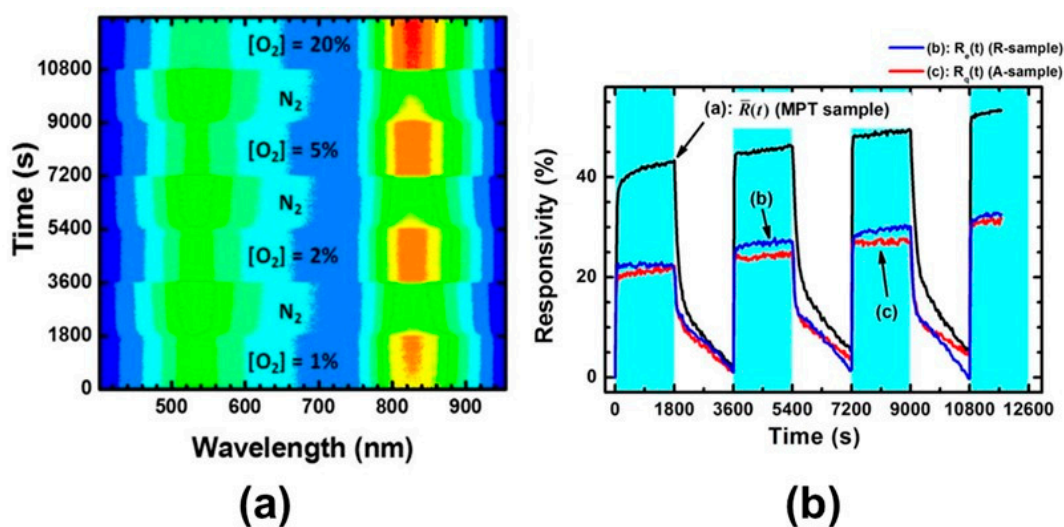


**Figure 18.** (a) Contour plot of PL spectral intensity measured during the exposure to oxygen/nitrogen mixtures with different O<sub>2</sub> concentrations. (b) Time-dependent optical responsivities  $R(t)$  at different O<sub>2</sub> concentrations for the mixed-phase sample (“mixed phase titania”, labelled as MPT) corresponding to the data shown in (a) and for two single-phase samples (anatase and rutile nanopowders). The responsivity for the mixed-phase sample is indicated in Equation (14), while the expression for the responsivities for anatase (showing a quenching response  $R_q$ ) and rutile (showing an enhancement response  $R_E$ ) are reported in Reference [213]. The O<sub>2</sub> concentration values are reported in (a). Reprinted from Reference [213], with the permission of AIP Publishing. Copyright 2016 AIP Publishing.

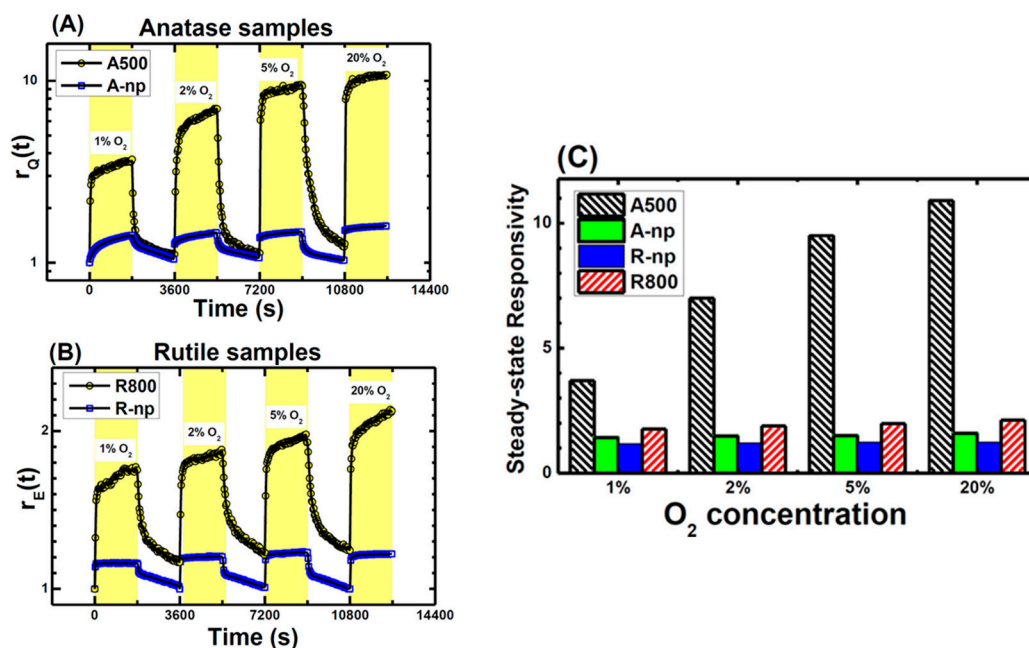


**Figure 19.** (A) Responsivity of hierarchical 1D anatase film (black curve, quenching response) as exposed to variable concentrations of O<sub>2</sub>. The black curve is compared to the data obtained in the same experimental conditions for commercial anatase nanopowders (blue curve). It shall be noted that the vertical scale has logarithmic units. (B) Responsivity of rutile film obtained by thermal annealing of the hierarchical 1D anatase film. As the TiO<sub>2</sub> nanoparticles coalesce at the anatase-rutile transition, the specific surface area decreases and so the gas responsivity. Nevertheless, the response (black curve) was found to be larger than the one exhibited by commercial rutile nanoparticles (blue curve). In both (A) and (B) the exposure to O<sub>2</sub> takes place in the yellow-colored time intervals, followed by exposure to flowing nitrogen (white regions). The tested oxygen concentrations (in percent units) were 1%, 2%, 5% and 20%. (C) Steady-state maximum responsivities of the tested samples measured for different O<sub>2</sub> concentrations. Adapted with permission from Reference [34]. Copyright 2017 American Chemical Society.

## 6. Intrinsic TiO<sub>2</sub> as Photocatalyst: Mechanisms and Limits

### 6.1. Basic Photocatalytic Processes and Their Characteristic Times

As mentioned, the photo-induced degradation of pollutants using a semiconductor photocatalyst involves the absorption of photons whose quantum energy  $\hbar\omega = hc/\lambda$  is sufficient to generate free charges (that is, electrons in the conduction band and holes in the valence band of the semiconductor) capable to migrate toward the surface and, once there, to participate in the oxidation-reduction reactions with suitable chemical species. These latter species can eventually be the pollutant themselves that will be transformed via direct photodegradation. However, it is more likely that the mentioned redox reactions will involve the dissolved oxygen (O<sub>2</sub>) and/or the hydroxide ions (OH<sup>-</sup>) present in aqueous environment, with formation of reactive oxygen species (ROS) that, in turn, will decompose the pollutants. A graphical representation of the main photocatalytic processes that occur after the photogeneration of charge carriers is shown in Figure 20.

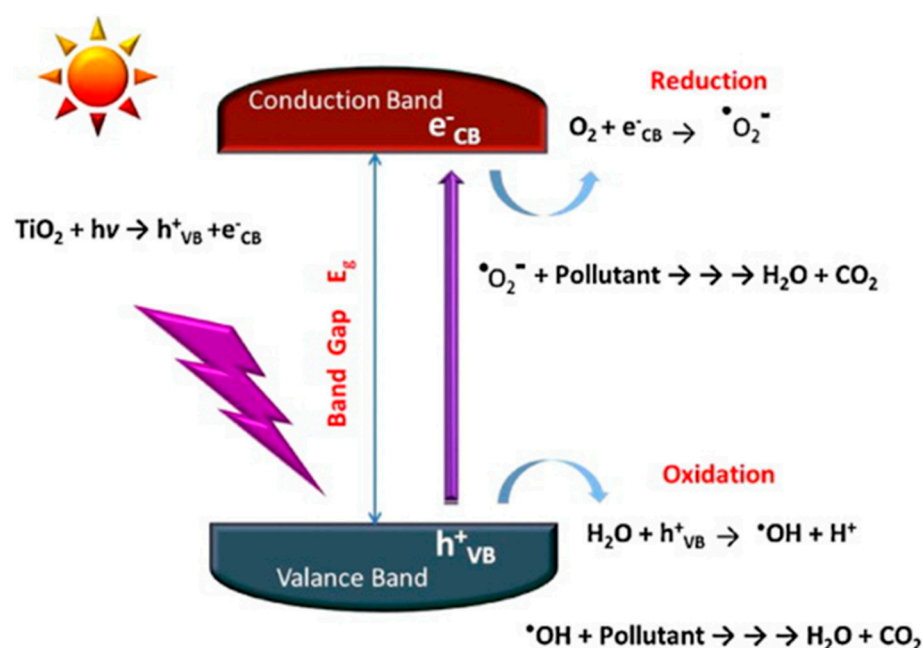
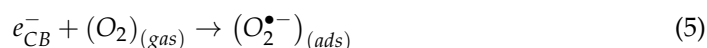


**Figure 20.** Graphic representation of the main processes that occur after the photogeneration of charge carriers in undoped TiO<sub>2</sub>. Reprinted with permission from Reference [214]. Copyright 2105 Elsevier Science.

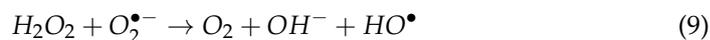
According to the prevailing understanding of photocatalytic phenomena, the most active species generated by illumination of TiO<sub>2</sub> in aqueous environment are the superoxide radicals (O<sub>2</sub><sup>•-</sup>), the hydroxyl radicals (HO<sup>•</sup>) and the photogenerated holes (h<sup>+</sup>). The superoxide radicals are generated from the dissolved molecular oxygen naturally present in the aqueous solution via photoreduction by a conduction band electron:



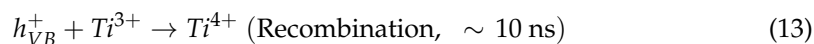
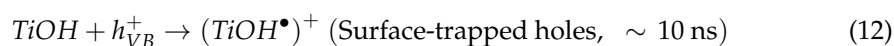
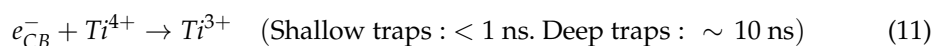
The hydroxyl radicals represent the primary oxidant in the photodegradation processes and are typically generated via two routes:

- (1) OH<sup>-</sup> ions in water are oxidized by photogenerated holes (see Equation (6)).
- (2) Superoxide radicals react with protons (H<sup>+</sup>) forming peroxidic radicals (HOO<sup>•</sup>), which, in turn form oxygen peroxide that further decomposes to hydroxyl radicals (see Equations (7)–(9)). Finally, photogenerated holes can also oxidize a pollutant molecule directly and trigger its degradation (see Equation (8) next). The corresponding reactions are:

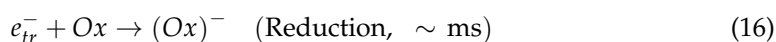
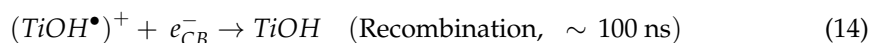




A review by Hoffman, Bahnemann and coworkers [84] summarized the relevant photocatalytic processes of photoexcited TiO<sub>2</sub> and their time dynamics, based on the results of investigations conducted via time-resolved microwave conductivity experiments [215,216]. The dynamical scheme produced by Hoffmann et al. (also referenced also in other successive reviews) [19,217] is shown in Figure 21 and summarized as follows. For a time duration of about 10 ns after the photogeneration of an electron-hole pair, mobile electrons ( $e_{CB}^-$ ) can be trapped at shallow or deep levels localized on Ti<sup>4+</sup> sites, while mobile holes ( $h_{VB}^+$ ) can be trapped on hydrated surface functionalities (TiOH), forming surface-bond hydroxyl radicals, here indicated by  $(TiOH^{\bullet})^+$  using the nomenclature of Ref. [84]. On the same time scale, the trapped electrons can recombine with mobile holes. These processes can be represented as follows (we also indicate the characteristic time scale for each one):



Hence, both the charge localization and (non-radiative) recombination is likely to occur on typical scales of about 10 ns, after which—according to the model by Hoffman et al.—the surviving charge are mainly surface-trapped holes localized at Ti-OH terminations. On successive stage, these holes can recombine with mobile electrons (Equation (12)) or oxidize an external species Red (see Equation (13)). On another hand, the same authors proposed slower dynamics for typical oxidation processes by photoelectrons (Equation (13)), i.e.,



There is clearly a competition between charge recombination and photocatalytic transformations. This competition is clearly in favor of the former, as long as the redox lifetimes vary in a range from hundreds of nanoseconds to hundreds of microseconds, while the recombination occurs with typical lifetimes of 1–10 ns.

In this model, it is argued that only the trapped charges do participate to the redox processes and that there is no direct oxidation by the conduction band holes. Indeed, as mentioned previously, the photogenerated holes are nowadays also considered possible oxidant for a direct degradation of organic contaminants [218]. However, whichever the case, a kinetic competition between the recombination of the charges (either trapped or mobile) and the redox reactions always occurs and the recombination rate is always a primary limiting factor of the photocatalytic efficiency. This observation justifies the importance of time-resolved studies of charge dynamics in TiO<sub>2</sub> and other metal oxide photocatalysts under operating conditions [173,195,219].



is about 3.2 eV, which—using the relation in Equation (1)—corresponds to photons of wavelength  $\lambda_g = 387$  nm lying in the near ultraviolet (or “UV-A”) interval of the electromagnetic spectrum. Unfortunately, this implies that TiO<sub>2</sub> is scarcely activated by solar radiation, as the near-UV light accounts for just about 5% of the total solar energy on Earth’s surface.

The second point is the scarce charge separation. Larger proximity of electrons and holes imply larger recombination rates and lower lifetimes of the photogenerated charge carriers, so that most of them will recombine before reaching the surface where the photocatalytic processes (such as ROS generation) shall occur.

In order to overcome these problems, several strategies have been scrutinized. Here, we will schematically classify them in two main categories, namely:

- (1) Strategies based on engineered TiO<sub>2</sub> nanocrystals, that is centered on modifications and/or control of intrinsic properties of TiO<sub>2</sub> nanocrystals, such as the stoichiometric composition or the surface termination (“facet engineering”),
- (2) Strategies based on the use of heterojunction photocatalysts, i.e., composites materials or in which TiO<sub>2</sub> is electronically coupled with a different material acting as cocatalyst.

We discuss separately these two categories in Section 7.1 and 7.2. Engineered TiO<sub>2</sub> nanocrystals are discussed in Section 7.1, with specific focus on highly-reduced TiO<sub>2</sub> (black and “colored” TiO<sub>2</sub>) and on the exploitation faceted TiO<sub>2</sub> nanocrystals, based on the natural tendency of electrons and holes to localize on different crystal termination in anatase.

The second category (Section 7.2) deals with some of the most used heterojunction photocatalysts and co-catalysts. The intrinsic length limitations of the present review will not allow a complete review of these extensively-studied topics. Aspects regarding the “hottest” topics will be discussed next. The reader is referred to other more specialized reviews for further information [2,19,21,22,232–235].

## 7. Present and Future Trends for TiO<sub>2</sub>-Based Heterostructure Photocatalysts and Engineered TiO<sub>2</sub>

### 7.1. Engineered TiO<sub>2</sub> Nanocrystals

The approaches described in the section do not recur to the use of cocatalysts. In particular, we consider here the strategies based on highly reduced TiO<sub>2</sub>—also often referred to as “black TiO<sub>2</sub>” or more generally to “colored TiO<sub>2</sub>”—and on facet engineered nanocrystals, in which the key role is played by the control of exposed crystalline facets.

#### 7.1.1. Black TiO<sub>2</sub>

The preparation and study of TiO<sub>2</sub> nanocrystals having intermediate to high levels of oxygen reduction is currently regarded as one of the most interesting approaches among that not relying on the use of cocatalysts. The concentration of oxygen vacancies is directly correlated with the optical absorption spectrum and hence on the apparent color of TiO<sub>2-x</sub> nanoparticle aggregates. Samples with very high concentrations of oxygen vacancies appear as dark grey or even black as the result of a large and approximately wavelength-independent optical absorption in the visible spectrum. These samples are referred to in literature as “black TiO<sub>2</sub>” [22,236–238] or as “grey” or otherwise “colored” version of TiO<sub>2</sub> (e.g., blue TiO<sub>2</sub>) [205,239,240]. In all of these cases, the formation of defects which are not present in pristine TiO<sub>2</sub> nanoparticles leads to an additional optical absorption band (“additional” here meaning that is absent in stoichiometric TiO<sub>2</sub>) and then to the sample coloration. The additional optical absorption band is associated to optical transitions that involve electrons trapped in the vacancy sites [104,233] and permits the formation of photogenerated carriers even under illumination with visible light, which is the general goal of this kind of approach.

Earlier evidence of the possibility to obtain “black TiO<sub>2</sub>” via hydrogenation process at high temperatures was reported by Chen and coworkers in 2011 [236], who demonstrated that the introduction of a disordered surface layer via hydrogenation led to formation of extended “band-tail” states (see Figure 22c) responsible for the enhanced optical absorption of visible light (see Figure 22b). The black TiO<sub>2</sub> powders also exhibited effective

photocatalytic properties, including photodegradation of the methylene blue dye and H<sub>2</sub> production [236]. The pioneering work of Chen and coworkers determined a huge interest in black and, more generally, in colored versions of TiO<sub>2</sub>, such as “grey” and “blue” titania.

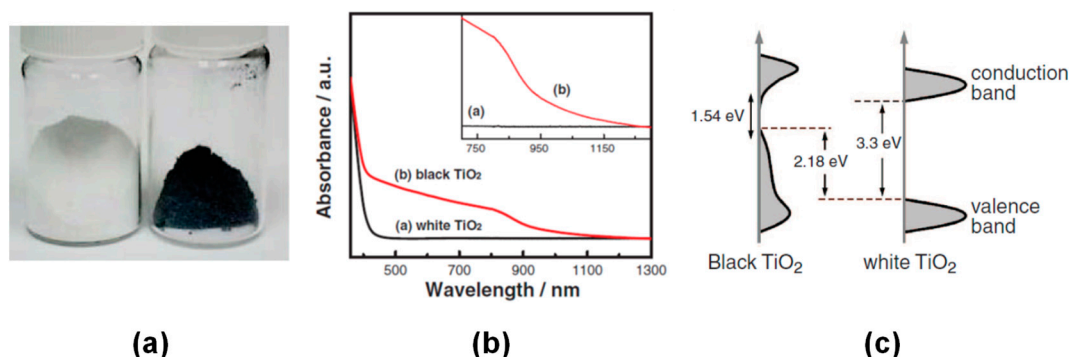


**Figure 22.** (a) White and black TiO<sub>2</sub> powders. (b) Optical absorption spectra of white TiO<sub>2</sub> and black TiO<sub>2</sub>, evidencing the slowly-varying non-zero optical absorption in the visible range, which extends even in the near-infrared range (evidenced in the inset). (c) Scheme of the electronic density of states of Black TiO<sub>2</sub> (compared to standard “white” TiO<sub>2</sub>), showing almost no optical bandgap due to the extended tail of states responsible of the black coloration. Reproduced with permission from Reference [236]. Copyright 2011, American Association for the Advancement of Science.

It is important to note that the H<sub>2</sub> production rate under visible light illumination observed in the earlier work by Chen et al. on Black TiO<sub>2</sub> was still unsatisfactory: a H<sub>2</sub> evolution rate of about 0.1 mmol h<sup>-1</sup> g<sup>-1</sup> was determined by activation at wavelength > 400 nm, versus a 10 mmol h<sup>-1</sup> g<sup>-1</sup> (i.e., two order of magnitude larger) under solar illumination [236]. In order to improve the visible light-activated efficiency, a significant number of works investigated additional routes for producing more efficient black TiO<sub>2</sub>. A commonly employed strategy involved the presence of Pt as co-catalyst, given its very high intrinsic efficiency in H reduction, as discussed in next section. However, it is important to underline that follow-up works evidenced that hydrogenated or reduced TiO<sub>2</sub> has been shown to be able to produce H<sub>2</sub> even in absence of any metal cocatalysts. This point was confirmed by several works employing different samples morphologies, such as single crystals [241], powders [242] or anodic nanotubes [243–245]. The absence of extrinsic catalytically-active reduction sites suggest the presence of some intrinsic co-catalytic site that appeared to be closely related to the hydrogenation process. An example is shown in Figure 23, taken from reference [243]: a significant H<sub>2</sub> evolution rate for anatase nanoparticles treated in high-pressure hydrogen flow was measured while other reduction processes such as high-temperature annealing in air or in Argon did not lead to significant H<sub>2</sub> evolution rate under solar illumination.

In a work by Liu and coworkers [246] it was shown that no significant changes in morphology and (anatase) crystalline order occurred after the hydrogenation process. An even more striking result was the uncorrelation between the optical properties of such “grey” samples and their solar light-activated H<sub>2</sub> photoproduction, as these samples exhibited negligible optical absorption and moderate values of H<sub>2</sub> production rates (see Figure 24). These findings suggest that the actual responsible for the H<sub>2</sub> photoevolution under solar illumination was not the entire ensemble of defects that determine the overall anatase coloration, but instead some specific type of defect, whose formation was optimized by the sample processing.

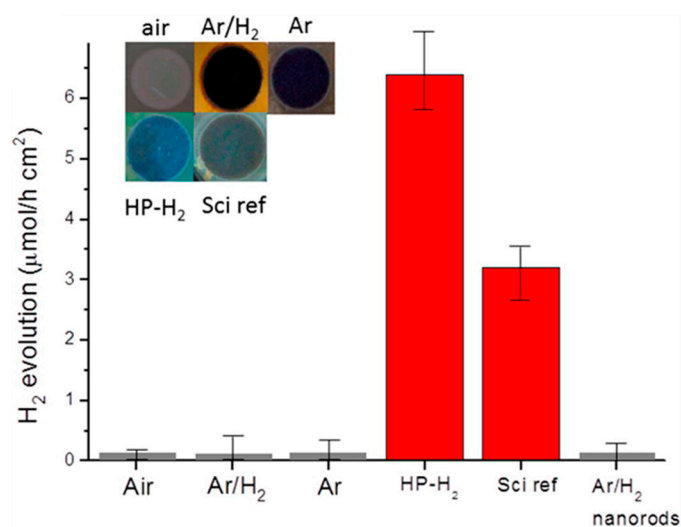


**Figure 23.** Rate of photocatalytic H<sub>2</sub> production in 50/50% volume water/methanol solution under AM1.5 illumination and in open circuit conditions by using TiO<sub>2</sub> nanorods and nanotubes treated in different atmospheres. Air: heat treatment in air at 450 °C. Ar: heat treatment in pure argon at 500 °C. Ar/H<sub>2</sub>: heat treatment in H<sub>2</sub>/Ar (5 vol%) at 500 °C. HP-H<sub>2</sub>: heat treatment in H<sub>2</sub> at 20 bar at 500 °C. Sci ref: heat treatment in H<sub>2</sub> at 20 bar at 200 °C for 5 days. Inset: optical images for the differently treated samples. Reprinted with permission from Reference [243]. Copyright 2014 American Chemical Society.

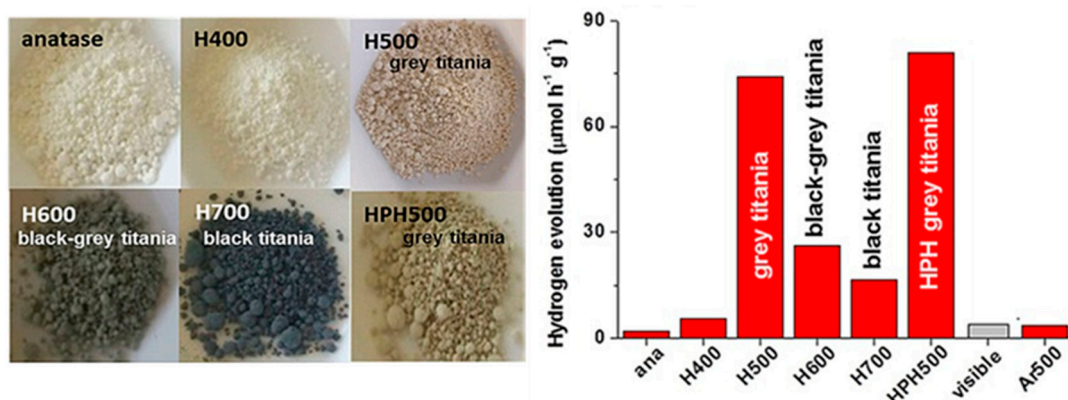


**Figure 24.** Left: Images of anatase nanopowders after different hydrogenation conditions (H: flow furnace, HPH: high pressure hydrogenation). Right: Rate of photocatalytic hydrogen evolution rate under AM 1.5 illumination for TiO<sub>2</sub> nanoparticles after different hydrogenation treatments. It is to be noted here that the largest activity is obtained not for black TiO<sub>2</sub> but for grey TiO<sub>2</sub>. Reprinted with permission from Reference [246]. Copyright 2017 Wiley-VCH Verlag GmbH & Co. KGaA, Weinheim.

Follow-up analyses based on PL measurements characterized the grey anatase H<sub>2</sub>-treated samples with an additional light emission in the range of 400–450 nm [247], which corresponds to sub-bandgap states positioned 0.2–0.4 eV below the conduction band edge. Interestingly, such a conclusion is not only compatible with scheme proposed in Figure 14 (shallow states) to explain the sub-bandgap excitation of PL in anatase (see processes (f) and (g)), but also is supported by a work by Lettieri and coworkers, who found a “optical signature” of reduced anatase by exploring a different strategy for the production of visible light-activated reduced TiO<sub>2</sub> [205]. In this work, a simple ethanol refluxing treatment at mild temperatures of P25 nanoparticles was employed to produce “blue TiO<sub>2</sub>” with improved visible light photocatalytic activity. The treatment caused an increase of Ti<sup>3+</sup> states and, most notably, a new sub-gap optical excitation band (absent in pristine anatase) associated to anatase PL and peaked at 430 nm, as shown in Figure 25. The data represent

photoluminescence excitation (PLE) intensity maps for untreated P25 (A) and EtOH-treated samples (B and C) and the novel excitation feature is clearly visible, with a maximum efficiency for 430 nm excitation wavelength, corresponding to a photon energy of about 2.9 eV (0.3 eV below the CB edge).

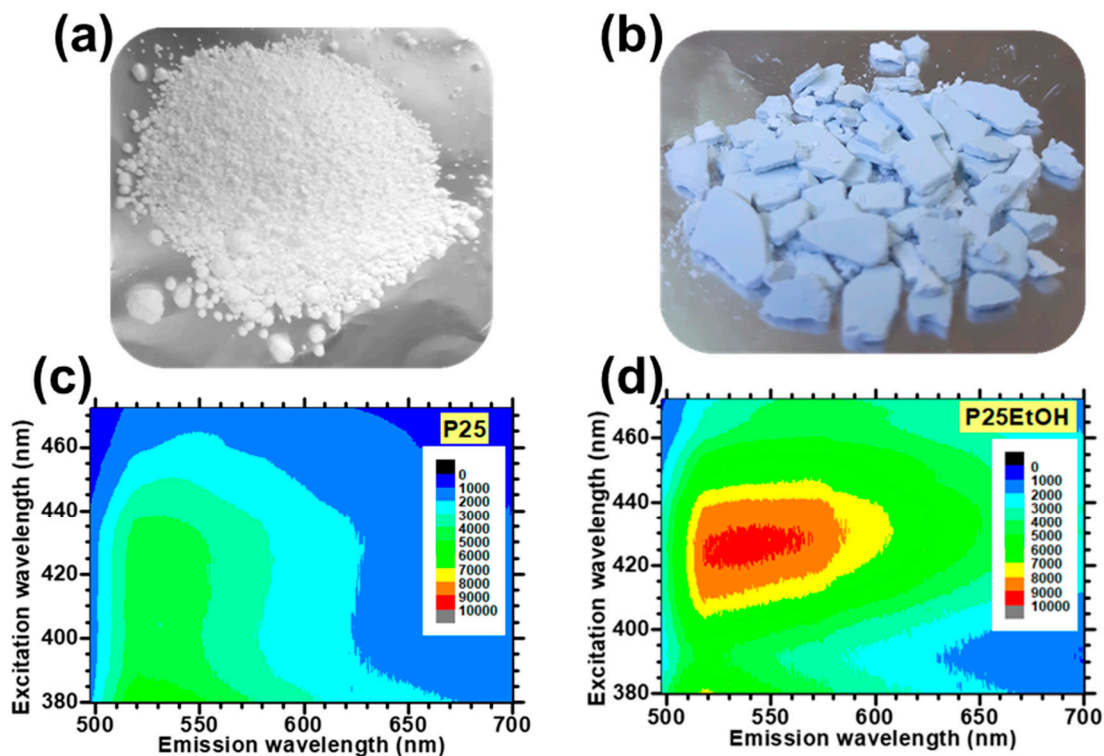


**Figure 25.** Top: images of untreated (a) and ethanol-treated (b) P25 powders. Bottom: excitation-resolved photoluminescence intensity maps (also PLE maps) for untreated (c) and ethanol-treated (d) P25 samples. The new excitation band which appears for ethanol-treated samples with a peak excitation wavelength of about 420 nm is associated to an additional radiative recombination channel that involves sub-gap excitations of valence band electrons to shallow states characterizing the reduced  $\text{TiO}_2$ , which then relax to deeper and luminescence-active electron traps. Figure 25 (c,d) are reprinted with permission from Reference [205]. Copyright 2020 American Chemical Society.

In summary, different findings suggest the existence of stable and “shallow”  $\text{Ti}^{3+}$  states whose energy position is close (0.2–0.4 eV below) to the CB edge, well above that of deep traps positioned about 0.8 eV below the CB edge (see Section 4.2 and references therein). These states appear to be responsible for the cocatalyst-free  $\text{H}_2$  evolution by hydrogenated “colored”  $\text{TiO}_2$ . Some indications about the actual nature of these intrinsic defects active in  $\text{H}_2$  production involve their location in the crystal: for example, investigations performed on anatase single-crystals correlated the  $\text{H}_2$  photocatalytic production of hydrogenated  $\text{TiO}_2$  to was associated to the presence of surface defects on high-index planes [241]. Additional procedures have been experimented to produce colored  $\text{TiO}_2$  with photocatalytically-active intrinsic defects. Some examples include  $\text{H}^+$  ion implantation [244], photodegradation of organic molecules on  $\text{TiO}_2$  surface [205,248,249], different treatments with reducing agents [250–252] and others: due to the vastness of the topic, the reader is referred to specialized reviews [22,233,238,253] for additional information.

### 7.1.2. Facet Engineered $\text{TiO}_2$

It is well established that the surface termination of a single-crystal metal oxide semiconductor affects several important electronic parameters, such as energy levels, bandgap energies and work functions. Several phenomena of facet-dependent properties in oxides of interest for photocatalysis are documented for  $\text{ZnO}$  and  $\text{TiO}_2$ . The case of

ZnO is a representative one: it crystallizes in polar (wurtzite) structures made of  $O^{2-}$  and  $Zn^{2+}$  planes perpendicular to the c-axis and hence its surface consists of a positively charged Zn-terminated (002) planes and a negatively charged O-terminated (002) planes. This facilitates to discern surface termination-dependent phenomena and study related phenomena. An example is a study by Wong et al. who detected via confocal microscopy the green PL emission ( $\sim 520$  nm) which is mostly correlated to surface oxygen vacancies, concluding that these defects in ZnO surfaces preferentially form along the polar (002) facets instead than on the non-polar (100) ones [254].

The interest in facet engineering in  $TiO_2$  nanocrystals arises from the possibility to improve the photocatalytic efficiency by using the different ability of non-equivalent surface planes to trap electrons instead than holes and thus achieve an effective charge carrier separation without the need to employ heterojunction effects and cocatalysts. An earlier evidence of the actual occurrence of surface-selective accumulation of electrons in single-crystal  $TiO_2$  has been reported by Ohno et al., who observed a selective photodeposition efficiency for Pt and  $PbO_2$  on specific surface-oriented anatase and rutile crystals [255], as shown in Figure 26.

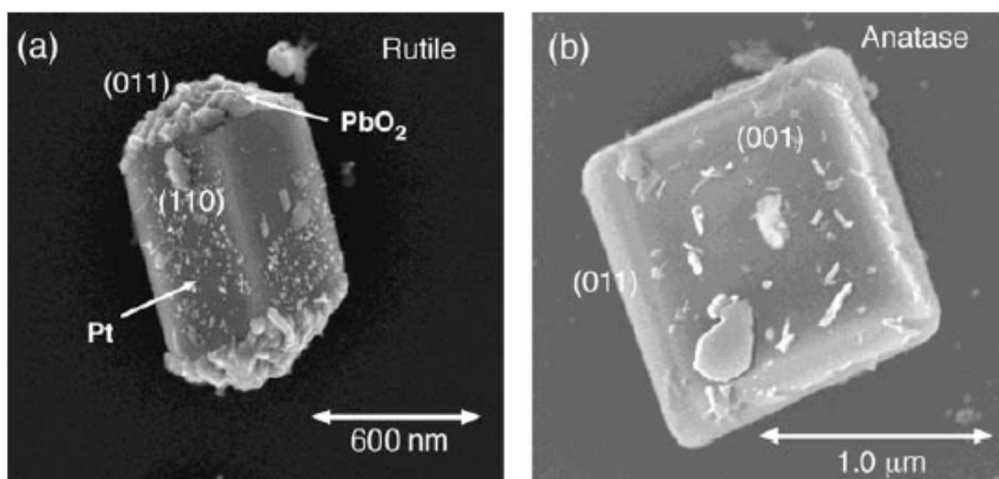


**Figure 26.** SEM images of a rutile particle (a) and an anatase particle (b) showing surface-selective  $PbO_2$  deposits. Reprinted with permission from Reference [255]. Copyright 2002 Royal Society of Chemistry and Centre National de la Recherche Scientifique.

Analysis of these results pointed toward a preferential transfer of electrons toward the  $TiO_2$  (101) facets, while instead holes are driven toward the (001) surface. In other words, they suggested that once photogenerated charge carriers of opposite sign reach the surface of an anatase crystal, its (101) surface will provide reduction sites while its (001) surface will provide oxidation sites.

A factor that typically limits the possibility to employ surfaces with high reactivities is that their relative amount tends to decrease as the crystal grows, due to the natural tendency to minimization of the surface energy. In the case of anatase  $TiO_2$  crystals this tendency translates in the predominance of (101) facets, which are more thermodynamical stability than the (001) ones. According to the Wulf construction [256], the relative amount of (101) is expected to be about 94% in an anatase crystal. Hence, the spatial charge carrier separation suggested by the results of Ref. [255] and the related eventual improvement of photocatalytic efficiency caused by the coexistence of both the facets is difficult to be observed in normal conditions. Therefore, the demonstration by Yang and coworkers [257] that in fluorine-terminated  $TiO_2$  surfaces the relative stability of the two surfaces is inverted, i.e., (001) becomes energetically favored with respect to (101) was an important breakthrough, as it provided synthetic procedures for producing nanocrystals with co-exposed (001) and (101) facets and controlled shapes (see also Figure 27).

Approximately in the same period, other procedures for growing TiO<sub>2</sub> nanocrystals with controlled shapes such as spherical, rhombic, elongated rhombic, truncated rhombic and dog-bone shapes were published by Dinh et al. [258], based on modified solvothermal techniques that employ oleylamine and oleic acid as capping surfactants (for the technical details we refer the interested reader to the original work, Ref. [258]).

Since these promising results, the role played by differently-oriented surfaces in TiO<sub>2</sub> [234,259–268] and in other catalysts such as Cu<sub>2</sub>O [269], ZnO [254], WO<sub>3</sub> [270] and BiVO<sub>4</sub> [271] has been theoretically and experimentally studied.

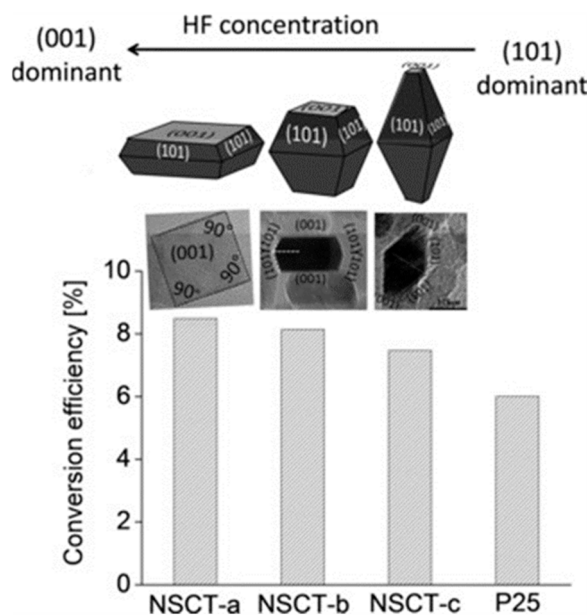


**Figure 27.** Graphical representation of the photoconversion efficiency vs. different percentage of exposed (001) facets in anatase TiO<sub>2</sub> nanocrystals. Reprinted from Reference [262]. Copyright 2011 John Wiley and Sons.

Regarding TiO<sub>2</sub>, several works involved the study of facet-dependent photocatalytic reactions on anatase with co-exposed (001) and (101) facets.

An interesting technical approach for those kind of studies has been reported by Tachikawa and coworkers [261], who shown that single-molecule fluorescence imaging of redox-responsive dyes can be used as spatially-resolved technique to evidence the different reactivities of (101) vs. (101) anatase facets, where the latter was the preferential site for photoinduced dye reduction [261]. This conclusion is supported by the work published in the same year by D'Arienzo et al. [259] employed photogeneration and analysis by electron spin resonance (ESR) of defects in shape-controlled anatase nanocrystals to address how the (001) and (101) facets participate to redox processes. In more detail, the exposure to UV radiation determined the formation of Ti<sup>3+</sup>, O<sup>-</sup> and O<sup>2-</sup> charge-trapping centers which are detectable by ESR. Correlating the relative amount of exposed crystal facets of nanocrystals with the relative abundance of these defects and with the sample reactivity (via phenol photodegradation). The experiments indicated that samples with larger relative amount of (001) surface area also exhibited larger concentrations of trapped holes and of photo-oxidation, while lesser photo-oxidative efficiency was associated to larger relative amounts of (101) surface areas and to Ti<sup>3+</sup> centers. The authors therefore concluded that the (001) and (101) surfaces essentially act as oxidation and reduction sites, respectively [259].

While the latter examples basically agree each other, other works pointed out that the surface characteristics are not intrinsically sufficient to determine the photo-oxidation reactivity. For example, Pan and coworkers [260] analyzed (001), (101) and (010)-terminated nanocrystals and argued that it is the combination of surface atomic structure (namely: the density of under-coordinated Ti<sub>5c</sub> surface atoms) and of band structure (namely: the energy

position of conduction band edge) that defines the actual photo-oxidation efficiency of the anatase nanocrystal. In more detail, the authors stated that the (001) and (010)-terminated crystals are favored in terms of photo-oxidative efficiency by a high density of  $Ti_{5c}$  sites, while the (101) and (010)-terminated crystals express exhibit stronger photo-reductive efficiency due to a higher energy of the electrons at the minimum of the conduction band, represented schematically in Figure 28. Since an efficient electron consumption can at the same time hamper the charge carrier recombination and thus promote photooxidation reactions initiated by the holes in the valence band, the authors concluded that (010) are expected to exhibit the highest reactivity.

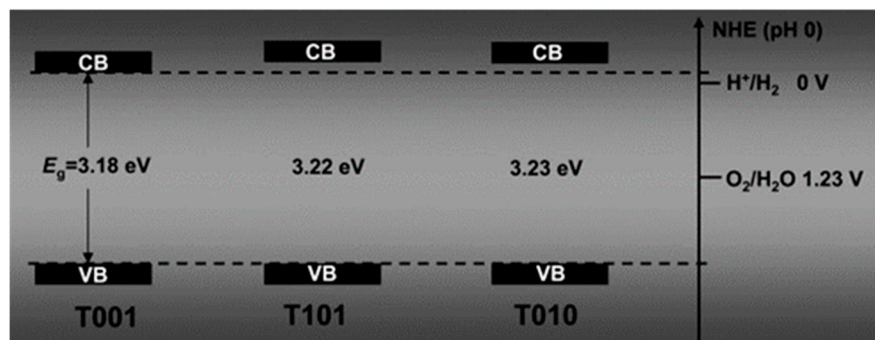


**Figure 28.** Bandgap energies extracted by optical absorption data from nanosized anatase single crystals with predominant (100), (001), and (010) exposed facets and compared with the standard semireactions potential for water oxidation and hydrogen reduction. Reprinted with permission from Reference [260]. Copyright 2011 John Wiley and Sons.

Insights in the origin of enhanced photocatalytic activity of facet-engineered anatase were experimentally evidenced by Kashiwaya et al. who prepared well-defined (001)-terminated and (101)-terminated anatase by means of different procedures and determined their Fermi level position by ultraviolet photoelectron spectroscopy [267]. The experimental results indicated that, regardless the surface preparation (sputtered vs. annealed) and the sample state (stoichiometric vs. oxidized), the Fermi level of (001) facets always had energy values lower (by amounts of 150–450 meV) than that of (101) facets. This Fermi level offset determines a band bending at the boundary between the two facets, acting as an effective “driving field” for spatial separation of the charge carriers. A schematic representation of the processes that shall occur in a faceted anatase crystal are shown in Figure 29.

Application of facet-engineered  $TiO_2$  for photocatalytic-based applications has been demonstrated in several works. For example, we mention here the improved  $H_2$  generation yield via methanol photosteam reforming published by D’Arienzo and coworkers [266] who also evidenced the reactivity of the (010) facets, a topic that was also highlighted in the Ref. [260] discussed previously. Other examples involve the enhanced efficiency of dye-sensitized solar cells (DSSCs) using photoanodes made of  $TiO_2$  nanocrystals with high percentage of exposed (001) facets [262] and the improvement of  $CO_2$  reduction [265] by anatase  $TiO_2$  with co-exposed (101) and (001) surfaces.

Other references and application examples can be found in reviews specialized on the topic [234,263,264,268].

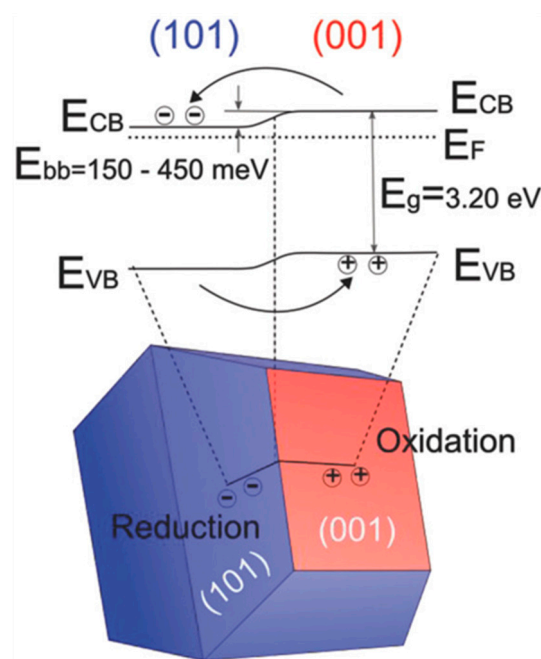


**Figure 29.** Interfacial band bending and spatial separation of charge carriers on anatase crystallites with co-exposed (001) and (101) facets. The band bending at the interface between the facets is based on the experimentally determined Fermi level difference between the facets and induces a transfer of photogenerated electrons from the (001) surface to the (101) surface (and vice-versa for the photogenerated holes). Reprinted with permission from Reference [267]. Copyright 2018 John Wiley and Sons.

### 7.2. $\text{TiO}_2$ -Based Heterojunction Photocatalysts

The coupling of  $\text{TiO}_2$  with a different and suitable material can be a way to tackle either the problem of visible (sunlight) activation and/or that of charge separation. In fact, a suitable “partner” material—also referred to as cocatalyst—may form a heterojunction with  $\text{TiO}_2$ , inducing a suitable built-in electrostatic fields and internal driving forces that facilitate the spatial separate the opposite charge carriers.

In other cases, the partner material could undertake the role of absorbing the photons in the visible range and of injecting the resulting photogenerated charge carriers into  $\text{TiO}_2$ . In regard to this approach the topic of dye-sensitized  $\text{TiO}_2$  materials is worth mentioning (see Section 7.2.4).

For a useful classification, we can distinguish between the cases in which the cocatalyst is a conductor (i.e., a metal) or a semiconductor. In the latter case, we can further make a distinction for metal oxide semiconductors and other classes of semiconductors. A separate class consists of carbonaceous and graphene-related cocatalysts, which may exhibit different degrees of semiconductor characteristics. This latter class includes for example graphene and reduced graphene oxide, carbon quantum dots and graphitic carbon nitride ( $\text{g-C}_3\text{N}_4$ ). As the subject of graphene- $\text{TiO}_2$  systems is too vast to be discussed here, we will briefly introduce only the topic of  $\text{TiO}_2/\text{g-C}_3\text{N}_4$  composites as it has been receiving a lot of attention in the latest years.

Metallic (or bimetallic) cocatalysts are used in conjunction with  $\text{TiO}_2$  as they typically contribute to spatial separation of photogenerated charge carriers and can favor the activation by visible light through the exploitation of plasmonic resonances, as it will be discussed in Section 7.2.1.

Regarding semiconductor-based photo-reactive cocatalysts, the most desired and advantageous configuration in which they can form a heterojunction with  $\text{TiO}_2$  is the one referred to as “direct Z-scheme configuration”, represented in Figure 30. In more detail, the direct Z-scheme is achievable if the semiconductor with higher value of conduction

band edge (or more precisely, with larger electron affinity) has also the lower value of the work function, as indicated in Figure (where the work functions are indicated by  $W_2 > W_1$ ). This might for example happen when the Fermi levels are close to the middle of the bandgap (as in undoped semiconductors). In this case, a built-in electric field will be formed at the interfacial region, leading to a band bending as represented in Figure 30, so that excess electrons generated in the semiconductor with lower work function (PC I in Figure, where "PC" stands for photocatalyst) will tend to remain in it, as a potential barrier at the interface prevents the transfer toward the other semiconductor. The same conclusion can of course be derived for the photogenerated holes in the semiconductor with larger work function (PC II in Figure). Therefore, the system will tend to remain for longer times with non-recombined holes in PC II and electrons in PC I. This is an ideal situation for cases in which PC II is  $\text{TiO}_2$  and PC I is a visible light-absorbing photocatalytic semiconductor.

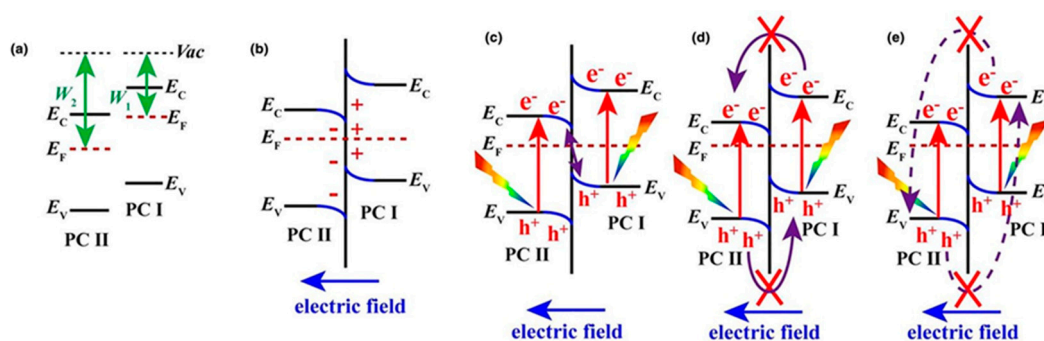


**Figure 30.** (a) Representation of the energy level configuration for a direct Z-scheme heterojunction. The photocatalyst on the left (PC II) was lower conduction band edge energy and higher work function ( $W_2$ ) than the photocatalyst PC I. This leads to the built-in electric field and band bending represented in (b). Under photon absorption the photogenerated electrons of PC II and holes of PC I accumulate at the interfacial region, increasing the probability of mutual recombination and thus the effective charge separation (c), while the unfavorable charge transfer processes or recombination indicated in (d) and (e) respectively are hampered by the relative position of the band edges and by the built-in electric field. As discussed in the text, this configuration is ideal to increase the redox efficiency of the composite system when the PC II is a strongly oxidizing photocatalyst such as  $\text{TiO}_2$ . Adapted with permission from Ref. [235]. Copyright 2018 Elsevier.

In fact, in such cases holes will remain longer in  $\text{TiO}_2$  which has a large oxidative efficiency (and larger than holes in PC I), while electrons in the partner material (PC I) have a larger reductive efficiency than electrons in PC II (In terms of redox potential, this is because the electrostatic potential is more positive than for holes in PC II than for holes in PC I, while it is more negative for electrons in PC I than for electrons in PC II). This situation presents a definite advantage for photocatalytic processes in order to overcome the problems related to the scarce charge separation and short charge-carrier lifetime in intrinsic  $\text{TiO}_2$ .

### 7.2.1. $\text{TiO}_2$ /Metal Heterostructures

Metals are probably the most commonly employed materials used to improve the photocatalytic properties of  $\text{TiO}_2$ . Both noble metals (such as Pt, Au, Pd, Ag) and non-noble metals (such as Cu and Ni) are commonly used as cocatalysts. Their role can be stated by considering three basic functions, namely: (i) Favoring the charge separation; (ii) Improving the optical absorption and local electromagnetic in the visible range via excitation of plasmonic resonances, and (iii) Providing additional catalytic active sites (i.e., the metal itself acts as catalyst) on the surface of the  $\text{TiO}_2$  nanoparticle.

The charge separation is caused by the built-in electric field that occurs close to a metal/semiconductor Schottky junction, that in turn is caused by the transfer of free charge carriers between two materials with different work functions. If the physical contact between a metal and a semiconductor is close enough to permit the quantum coupling of the charges of the two materials (i.e., in first approximation when spatial overlap of the

orbitals of the charge carrier is present), electrons will transfer from the semiconductor to the metal when the Fermi level is lower in energy than the semiconductor one or—to state it in different but equivalent words—when the work function of the semiconductor is lesser than that of the metal. Metals typically have larger work function ( $W_f$ ) than metal oxide semiconductors, as their values typically span in the 4–5 eV range and with notable values of about  $W_f \approx 5.6$  eV for Pt and  $W_f \approx 5.1$  eV for Au, Pd and Ni [272]. These values indicate that electron transfer from  $\text{TiO}_2$  to the metal is likely to occur, as they indicate Fermi levels of the metal which is well below in potential energy (and more positive in terms of electric potential vs. NHE) of the conduction band edge of  $\text{TiO}_2$ . See Figure 31 for reference.

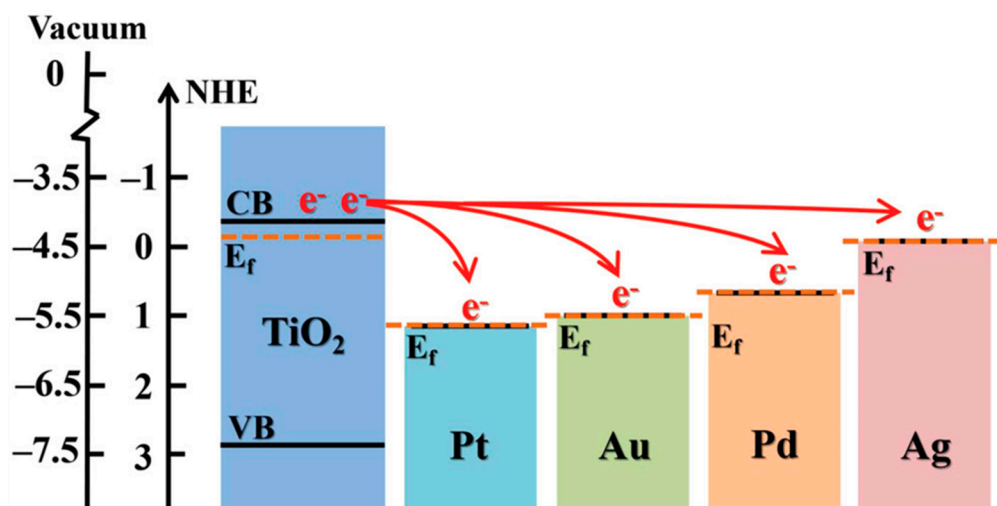


**Figure 31.** Potential energy values (referenced to the vacuum level) and electrical potential values (referenced to NHE) for the conduction band edge of  $\text{TiO}_2$  compared with the Fermi levels of Pt, Au, Pd, and Ag. The latter values refer to cases where the metals are isolated (that is, in absence of electrical contacts with other materials and in absence of illumination). Reprinted with permission from Reference [21]. Copyright 2019 WILEY-VCH Verlag GmbH & Co. KGaA, Weinheim.

In other words, as the photocatalyst is activated by optical absorption the transition region close to the heterojunction will be depleted of electrons, due to the effect of the built-in electric field and the electron-hole recombination will be slowed down. The effect is more pronounced for higher Schottky barriers, which based on the data shown in Figure occur at contact of  $\text{TiO}_2$  with Pt and Au.

The metal itself also typically contributes to a catalytic process. For example, Pt is very effective for hydrogen evolution (i.e., proton reduction) due to the fact that the Gibbs energy change for atomic hydrogen adsorption on Pt is very low, so that the process in which Pt binds to  $\text{H}^+$  and releases  $\text{H}_2$  is thermodynamically easier than for example for the case of Au [273]. However, Au has a distinct advantage in that it supports localized plasmonic resonance in the visible range [274,275]. An example showing a direct evidence of plasmonic-related improvement of photocatalytic efficiency in  $\text{TiO}_2/\text{Au}$  systems was shown in Reference [276], where the photocatalytic production rate for  $\text{H}_2$  under illumination of  $\text{TiO}_2$  nanofibers co-decorated by Pt and Au was measured for optical excitation at 550 nm (plasmon resonance for the Au particles) and 420 nm. The experiments evidenced a wavelength-dependent enhancement for  $\text{H}_2$  generation correlated to the plasmonic absorption of Au.

The plasmonic properties of Au allow to employ it in combination with a different metal, in order to take advantage of both Schottky junction-related charge separation and plasmonic coupling with optical radiation. Therefore, Au–Pt or similar (Au–M) bimetallic cocatalyst (M can typically be also Pd, Ag, Ru, Rh) are often employed to improve the photocatalytic efficiencies of  $\text{TiO}_2$  [277–280].

### 7.2.2. TiO<sub>2</sub>/Metal Oxide Semiconductors

Several metal oxide semiconductors can be used as cocatalysts having the function of trapping either electrons or holes photogenerated in TiO<sub>2</sub>. Examples include oxides of copper such as CuO and Cu<sub>2</sub>O, NiO, RuO<sub>2</sub>, IrO<sub>2</sub> and oxides of cobalt (CoO<sub>x</sub>).

Cuprous oxide (Cu<sub>2</sub>O) is often employed as reduction cocatalyst: it is a p-type semiconductor with a narrow bandgap of 2.2 eV. As TiO<sub>2</sub> is a n-type semiconductor, a TiO<sub>2</sub>/Cu<sub>2</sub>O junction typically results in a p-n heterojunction and, at equilibrium, in a built-in electrostatic field that drives excess (photogenerated) holes electrons of TiO<sub>2</sub> toward Cu<sub>2</sub>O (and vice-versa for electrons photogenerated in Cu<sub>2</sub>O). As a result, Cu<sub>2</sub>O can be effectively used as reduction cocatalyst in hydrogen for photocatalytic hydrogen evolution [281–285]. A schematic representation of the H<sub>2</sub> evolution reactions over a TiO<sub>2</sub>/Cu<sub>2</sub>O composite is reported in Figure 32. The scheme shows the oxidation of water (or of an organic species) operated by holes in Cu<sub>2</sub>O, with proton reduction by photogenerated electrons in the conduction band. For simplicity, the scheme assumes here the generation of charge carriers in both the materials and thus shows the both the possible charge transfer pathways. Noticeably, the narrow optical gap of Cu<sub>2</sub>O permits the activation of proton reduction under visible light illumination: the energy offset in the conduction bands (i.e., −1.5 Volts and −0.5 Volts (vs. NHE) for Cu<sub>2</sub>O and TiO<sub>2</sub> respectively [286] implies that the electron are transferred to TiO<sub>2</sub>, where the proton reduction can occur as shown in Figure, while photogenerated holes remain in Cu<sub>2</sub>O where they participate to the oxidation of water or of an organic species that acts as suitable sacrificial agent.

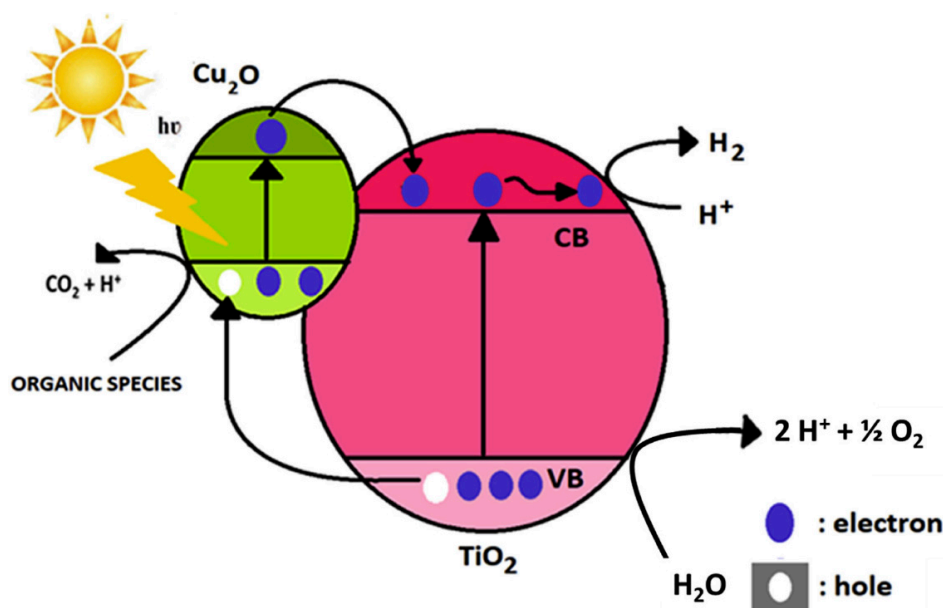


**Figure 32.** Scheme of the hydrogen evolution process in a Cu<sub>2</sub>O/TiO<sub>2</sub> heterojunction photocatalyst under solar illumination. It is assumed that the Fermi level equilibrium has already been achieved, to that the built-in field drives electrons from Cu<sub>2</sub>O to TiO<sub>2</sub> and vice-versa. The scheme includes possible photogeneration in both TiO<sub>2</sub> and Cu<sub>2</sub>O, where the latter implies the possibility of H<sub>2</sub> generation activated by visible light thanks to the electron transfer from Cu<sub>2</sub>O to TiO<sub>2</sub>. Reprinted with permission from Reference [287]. Copyright 2020 Hydrogen Energy Publications LLC. Published by Elsevier Ltd.

Cuprous oxide is often used in conjunction with additional functional elements, such as noble metals (e.g., Pt [288,289], Au [290] or metal copper [291–294]) to prepare ternary hybrid photocatalysts. A review that includes several references and experimental results on the use of TiO<sub>2</sub>/Cu<sub>2</sub>O composites for H<sub>2</sub> production through photoreforming processes has been recently published by Marotta and coworkers [287].

Nickel oxide (NiO) is also a p-type semiconductor which can be employed to obtain p-n heterojunctions with TiO<sub>2</sub>. An accurate characterization of the energy levels alignment of NiO/TiO<sub>2</sub> composites has been reported by Uddin and coworkers [295], who combined

XPS, UPS and absorption spectroscopy to sketch the electronic configuration of the p-n heterojunction as shown in Figure 33. The resulting heterojunction photocatalysts typically exhibit an improved efficiency (compared to commercial anatase or P25 nanoparticles) in oxidative photodegradation of pollutants [296] and hydrogen evolution [295,297].

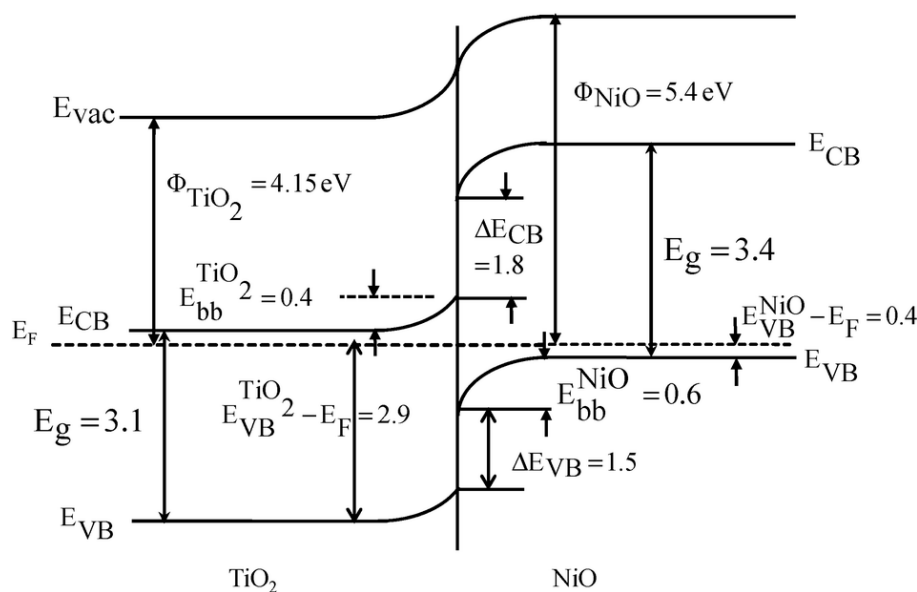


**Figure 33.** Band alignment at the  $\text{TiO}_2/\text{NiO}$  heterojunction. Reprinted with permission from Reference [295]. Copyright 2017 Royal Society of Chemistry.

For additional information on other metal oxide cocatalysts—such as  $\text{RuO}_2$ ,  $\text{Co}_3\text{O}_4$  and  $\text{IrO}_2$ , the reader may consult the review by Meng and coauthors [21] and references therein.

### 7.2.3. $\text{TiO}_2/g\text{-C}_3\text{N}_4$ Heterostructures

In recent years, graphitic carbon nitride ( $g\text{-C}_3\text{N}_4$ ) has become one of the newest and mostly investigated low-gap photocatalytic materials, both as a stand-alone photosensitive 2D material and as a functional “partner” for  $\text{TiO}_2/g\text{-C}_3\text{N}_4$  heterostructures for hydrogen production.

The term graphitic carbon nitride ( $g\text{-C}_3\text{N}_4$ ) designs a class of carbon nitride compounds whose general formula is  $\text{C}_3\text{N}_4$ , although it is common that the stoichiometric ratio is slightly modified due to some amount of hydrogen. The class includes seven phases of  $\text{C}_3\text{N}_4$  [298], two of which are more interesting for photocatalytic applications. These are the g-h-triazine phase, obtained by polymerization of s-triazazine (Figure 34a) and the g-h-heptazine phase, obtained by polymerization of tri-s-triazazine (or heptazine, Figure 34b). Their energy gaps were calculated to be 2.97 and 2.88 eV, respectively, while instead the other forms of  $\text{C}_3\text{N}_4$  show optical absorption only in the ultraviolet range [299]. As a consequence, the g-h-triazazine and g-h-heptazine phases are those suitable for photocatalytic production of hydrogen.

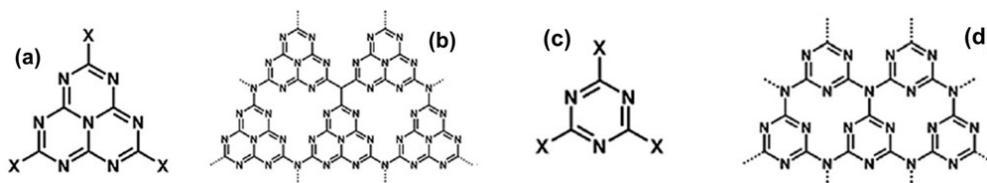


**Figure 34.** (a) s-heptazine (or tri-s-triazazine), (b) s-heptazine-derived  $g\text{-C}_3\text{N}_4$ , (c) s-triazazine, (d) s-heptazine-derived  $g\text{-C}_3\text{N}_4$ . Adapted from Reference [300] with permission. Copyright 2015 WILEY-VCH Verlag GmbH & Co. KGaA, Weinheim.

The interest in  $g\text{-C}_3\text{N}_4$  was boosted by the observation of  $\text{H}_2$  production via water splitting under visible light illumination by Wang et al. in 2009 [301]. The interest in the material has increased since then, prompted by the potential perspective of conjugated polymers shifting the dominance among photocatalysts from inorganic semiconductors to more abundant and easily processable polymeric ones [302,303]. The material in fact shows several advantages: it is fairly inexpensive, highly available, chemically inert in several solvents, thermally stable (up to  $600\text{ }^\circ\text{C}$  in air). Furthermore, as mentioned previously, its optical gap allows the optical absorption of visible light. Finally, bulk powders can be used to prepare few-layers or even single-layer 2D material.

Exploitation of heterojunction effects of  $g\text{-C}_3\text{N}_4$  with  $\text{TiO}_2$  clearly represents a route to be explored in order to improve the performances of both the materials. While in fact the  $g\text{-C}_3\text{N}_4$  is capable to add the visible-light activation functionality to  $\text{TiO}_2$ , this latter is more effective as oxidizing agent due to the relative position of its valence band with respect to the one of  $g\text{-C}_3\text{N}_4$ .

Several theoretical and experimental works point out that the electronic coupling of  $g\text{-C}_3\text{N}_4$  with  $\text{TiO}_2$  supports the occurrence of a direct Z-scheme band alignment, as described in Figure 30. An example is shown from the work by Wei and coworkers [304], whose computation of work function of the separated materials and of the band alignment of the  $g\text{-C}_3\text{N}_4/\text{TiO}_2$  led the authors to conclude that the equalization of the Fermi levels of the two materials sets up a built-in electric field as in Figure 35 and representative of a direct Z-scheme configuration. In fact, the configuration prevents photogenerated electrons in  $g\text{-C}_3\text{N}_4$  and holes in  $\text{TiO}_2$  to cross the interface, as shown in Figure for the processes labelled as “Route 3” and “Route 4” which are electrostatically inhibited. On another hand, the recombination of photogenerated  $\text{TiO}_2$  electrons and  $\text{C}_3\text{N}_4$  holes is possible and electrostatically favored near the interface (Route 5).

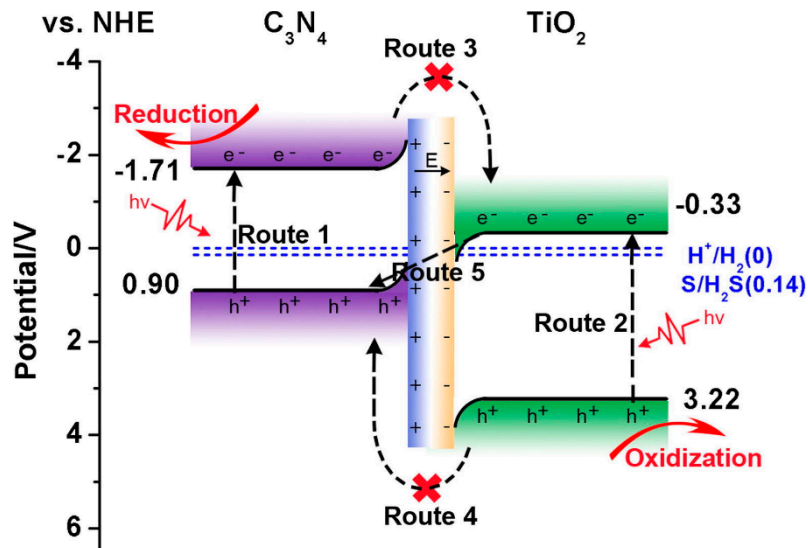


**Figure 35.** Electronic configuration of a  $\text{TiO}_2/g\text{-C}_3\text{N}_4$  heterojunction with direct Z-scheme configuration. The various processes (Route 1 to Route 5) and the favorable separation of photogenerated holes in  $\text{TiO}_2$  and electrons in  $g\text{-C}_3\text{N}_4$  is discussed in the text. Reprinted from Reference [304] with permission. Copyright 2019 Elsevier.

Nowadays, significant efforts are put in the study of  $\text{TiO}_2/g\text{-C}_3\text{N}_4$  heterostructures for applications such as  $\text{H}_2$  photogeneration,  $\text{CO}_2$  reduction and pollutants photodegradation. Perspectives are generally considered promising, as proved by the large amount of works published in the topic in the last years, even though some aspects need to be improved such as adsorption affinity for pollutants and long-term reproducibility of photocatalyzed photodegradations [303]. For additional information the reader is referred to some specialized review on the topic [302–306] and references therein.

#### 7.2.4. Dye-Sensitized TiO<sub>2</sub>

Coupling TiO<sub>2</sub> with organic dyes capable to absorb light in the visible range and inject the photogenerated electrons to TiO<sub>2</sub> represents a possible way to achieve a sunlight-activated photocatalyst. A coupled TiO<sub>2</sub>/dye system in which such two-step sequence (i.e., photon absorption and charge carrier transfer) occurs is known as “dye-sensitized” TiO<sub>2</sub>. Dye sensitization in TiO<sub>2</sub> is a well-known topic, being it the key ingredient for the realization of dye-sensitized solar cells (DSSC), a well-known and widely studied class of thin-film photovoltaic cells that are receiving worldwide attention since more than two decades thanks to their simple preparation, low toxicity and affordable production costs. Even is the topic of DSSCs is beyond the scope of this review, for the sake of our discussion it is worth mentioning that electrons in DSSCs are generated by optical absorption in the dye molecule and transferred to a TiO<sub>2</sub> photo-anode, while holes are transferred to a reduced form (typically an iodide ion I<sup>−</sup>) of redox mediator which is then reduced back by gaining electrons at the cathode and so closing the electric circuit [307].

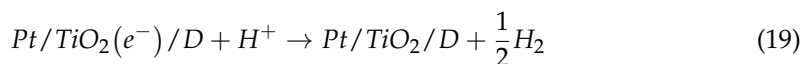
The interfacial charge transfer in dye-sensitized TiO<sub>2</sub> (and in other dye-sensitized photocatalysts as well) occurs as in DSSC systems and electrons are then transferred to a catalyst (typically Pt) instead of being used for electricity generation (as in a solar cells). To allow the process to continue, the oxidized dye molecule has to be reduced by an appropriate electron donor (or, equivalently, a hole scavenger).

When the overall process is optimized, the dye-sensitized TiO<sub>2</sub> photocatalyst can be used for solar fuel (hydrogen) generation, according to the scheme reported in Figure 36 that shows the complete sequence of elementary charge carrier processes for H<sub>2</sub> production. The photoexcitation through visible light consists of the generation of electrons and holes in the dye molecules. It is worth noting the presence of a suitable “sacrificial electron donor” (indicated as SED) as reducing agent, whose role is to restore the fundamental state of the Dye molecule [308].

The sequence of elementary processes which is regarded as the one occurring more frequently involves the injection of an electron from the photoexcited dye (D<sup>\*</sup>) to the TiO<sub>2</sub> as first step, implying that the excited dye becomes a dye radical cation (D<sup>\*+</sup>). Successively, the latter is reduced by the SED agent. Overall, the processes can be summarized as follows:



Another scheme is possible in which the first process is now the hole capture operated by the SED agent, followed by the injection of a photoelectron from the radical anion to the TiO<sub>2</sub>. As mentioned, this different sequence shall occur in a minority of cases [309]. Regardless, the resulting state is the same, that is free electrons in the semiconductor CB will allow the generation of H<sub>2</sub> via proton reduction:



The same class of materials can be used for remediation of environmental pollutants. For example, Choi and coworkers [310] studied the use of dye-sensitized TiO<sub>2</sub> for both H<sub>2</sub> generation and photodegradation through visible light of Cr(VI), as represented in Figure 37. Here, the authors evidenced as major photodegradation process the direct reduction of Cr(VI) to Cr(III) carried out by photogenerated electrons (see mechanism 7), and an indirect reaction pathway based on superoxide-mediated reduction (see mechanisms 9 and 10 in Figure). As pointed out by the authors, the photodegradation pathway for aqueous substrates involve different reactions and are more difficult to control as compared with those for H<sub>2</sub> production that occurs predominantly in the absence of reactive oxygen species. As a consequence, the relationship between the concentrations of species and the rate of reaction for degradation of pollutants and for H<sub>2</sub> generation are different, in the general cases.

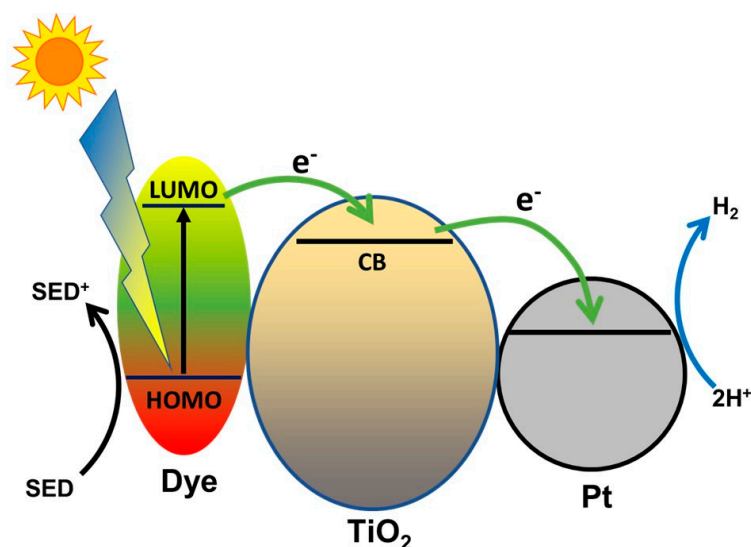


**Figure 36.** Scheme of the key charge carrier processes in  $\text{H}_2$  photogeneration by a dye-sensitized  $\text{TiO}_2$  photocatalyst. The electrocatalyst involved in the final step is here represented as platinum (Pt) in accordance with the Equation (19).

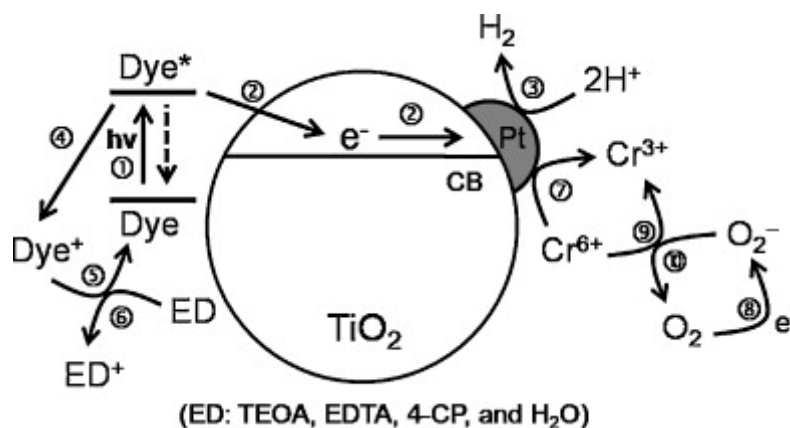


**Figure 37.** Schematic representation of photoinduced  $\text{H}_2$  generation and of reduction of  $\text{Cr}(\text{IV})$  pollutant through dye-sensitized  $\text{TiO}_2$  in water. Some particular processes to be noted are dye regeneration (processes 5 and 6) through the electron donor ED (indicated as “SED” in the previous figure), the reduction of  $\text{Cr}(\text{VI})$  to  $\text{Cr}(\text{III})$  by direct reduction (process 7) or by reaction with superoxide ion intermediates (process 9 and 10). Reprinted from Reference [310] with permission from Elsevier. Copyright 2012 Elsevier Science B.V.

It is worth mentioning that study of dyes used to sensitize photocatalysts does not overlap that of dyes for DSSCs. Instead, the two study fields are developing independently, as a direct consequence of the different conditions in which the two systems operate. To this regard, we can mention that dye-sensitized  $\text{TiO}_2$  has to be optimized for operating in water and that the dye must allow the regeneration of the electron donor agents, which are typically different from the redox couples (e.g.,  $\text{I}^-/\text{I}_3^-$ ) used in DSSC.

At present, the solar-to-hydrogen efficiency of dye-sensitized  $\text{TiO}_2$  is lesser than that obtainable by photoelectrochemical cells. However, the dye-sensitization approach for  $\text{TiO}_2$  leads to comparatively simpler, less expensive and more scalable systems [311]. Therefore, it is significant to pinpoint any room for possible improvements, in particular for what regards efficiency and cost issues. In regard to the efficiency considerations, the molecular design of the dye sensitizer is a central element. It involves the chemical structure of the groups that anchor the dye to the  $\text{TiO}_2$  [312], the dye hydrophobicity and hydrophilicity [313] and of course the relative energy level position with respect to the CB

of the TiO<sub>2</sub> (or, in more general extent, of other photocatalysts). Further information on the foreseeable progress on those aspects can be found on recent reviews [308,314,315].

## 8. Conclusions

As a conclusion of this work, we intend to underline the importance of reviewing (and, when possible or needed, updating) the basic knowledge on fundamental processes that characterize a functional photocatalyst, even if it is probable that future applications will employ it in significantly modified versions, such as highly reduced (or doped) forms or as partner material in composite systems and photocatalysts.

The literature on TiO<sub>2</sub> and TiO<sub>2</sub>-based systems is abundant, as argued in Sections 1–3 where we also discussed some historical facts about the study of intrinsic TiO<sub>2</sub> photophysical and photo-oxidating properties. As a consequence we believe that a review might be useful for scholars (in particular for those who are approaching the field) if it aims at summarizing specific and basic topics, as we did here for the photogenerated charge carrier processes in TiO<sub>2</sub>. The fate and the time dynamics of photogenerated electrons and holes define in a major way the applicative potential of a photocatalyst. We discussed these topics alongside the review, and in particular in Sections 4 and 6. The optical properties are also important: they are not only responsible for the activation of the photocatalyst (absorption coefficient), but they can also be used as modifiable parameters for photocatalytic or chemical sensing applications. This point has been discussed in Section 5, underlining the possibility of using—to these aims—special features of light propagation in engineered structures (e.g., “metasurfaces” and photonic crystals) and photoluminescence of mixed-phase TiO<sub>2</sub>.

Mechanisms and characteristic lifetimes of TiO<sub>2</sub> photocatalysis have been summarized in Section 6, discussing them in order to highlight the limitations of intrinsic TiO<sub>2</sub> and introduce some of the future trends that will likely involve TiO<sub>2</sub> as key element in composite catalysts. Several methods are under scrutiny to develop improved photocatalysts that might facilitate some significant advancement in solar fuel technologies. Some of these, discussed in this review (Section 7), include defect tailoring/engineering and design of nanocomposite heterojunctions. Considering this last point, it is very likely for example that research on some specific systems, such as TiO<sub>2</sub>/g-C<sub>3</sub>N<sub>4</sub> will grow in the next future. Hopefully, these studies on clean energy conversion technologies will evolve in mature key-enabling technologies for the era of ecological transition.

**Author Contributions:** S.L., M.P. and P.M. conceived the work; S.L. worked on the bibliography section and wrote the original draft, with contributions from A.F. and L.S.A. All the authors reviewed and edited the manuscript. All authors have read and agreed to the published version of the manuscript.

**Funding:** This research received no external funding.

**Data Availability Statement:** No new data were created or analyzed in this study.

**Conflicts of Interest:** The authors declare no conflict of interest.

## References

1. Habisreutinger, S.N.; Schmidt-Mende, L.; Stolarczyk, J.K. Photocatalytic Reduction of CO<sub>2</sub> on TiO<sub>2</sub> and Other Semiconductors. *Angew. Chem. Int. Ed.* **2013**, *52*, 7372–7408. [[CrossRef](#)] [[PubMed](#)]
2. Low, J.; Cheng, B.; Yu, J. Surface Modification and Enhanced Photocatalytic CO<sub>2</sub> Reduction Performance of TiO<sub>2</sub>: A Review. *Appl. Surf. Sci.* **2017**, *392*, 658–686. [[CrossRef](#)]
3. Fujishima, A.; Zhang, X.; Tryk, D. TiO<sub>2</sub> Photocatalysis and Related Surface Phenomena. *Surf. Sci. Rep.* **2008**, *63*, 515–582. [[CrossRef](#)]
4. Kanan, S.; Moyet, M.A.; Arthur, R.B.; Patterson, H.H. Recent Advances on TiO<sub>2</sub>-Based Photocatalysts toward the Degradation of Pesticides and Major Organic Pollutants from Water Bodies. *Catal. Rev.* **2020**, *62*, 1–65. [[CrossRef](#)]
5. Moniz, S.J.A.; Shevlin, S.A.; Martin, D.J.; Guo, Z.-X.; Tang, J. Visible-Light Driven Heterojunction Photocatalysts for Water Splitting—A Critical Review. *Energy Environ. Sci.* **2015**, *8*, 731–759. [[CrossRef](#)]

6. Fajrina, N.; Tahir, M. A Critical Review in Strategies to Improve Photocatalytic Water Splitting towards Hydrogen Production. *Int. J. Hydrog. Energy* **2019**, *44*, 540–577. [[CrossRef](#)]
7. Wang, Q.; Domen, K. Particulate Photocatalysts for Light-Driven Water Splitting: Mechanisms, Challenges, and Design Strategies. *Chem. Rev.* **2020**, *67*. [[CrossRef](#)]
8. Clarizia, L.; Vitiello, G.; Pallotti, D.K.; Silvestri, B.; Nadagouda, M.; Lettieri, S.; Luciani, G.; Andreozzi, R.; Maddalena, P.; Marotta, R. Effect of Surface Properties of Copper-Modified Commercial Titanium Dioxide Photocatalysts on Hydrogen Production through Photoreforming of Alcohols. *Int. J. Hydrog. Energy* **2017**, *42*, 28349–28362. [[CrossRef](#)]
9. Pellegrino, F.; Sordello, F.; Mino, L.; Minero, C.; Hodoroaba, V.-D.; Martra, G.; Maurino, V. Formic Acid Photoreforming for Hydrogen Production on Shape-Controlled Anatase TiO<sub>2</sub> Nanoparticles: Assessment of the Role of Fluorides, {101}/[001] Surfaces Ratio, and Platinization. *ACS Catal.* **2019**, *9*, 6692–6697. [[CrossRef](#)]
10. Qi, K.; Cheng, B.; Yu, J.; Ho, W. Review on the Improvement of the Photocatalytic and Antibacterial Activities of ZnO. *J. Alloys Compd.* **2017**, *727*, 792–820. [[CrossRef](#)]
11. Prakash, J.; Sun, S.; Swart, H.C.; Gupta, R.K. Noble Metals-TiO<sub>2</sub> Nanocomposites: From Fundamental Mechanisms to Photocatalysis, Surface Enhanced Raman Scattering and Antibacterial Applications. *Appl. Mater. Today* **2018**, *11*, 82–135. [[CrossRef](#)]
12. Li, P.; Li, J.; Feng, X.; Li, J.; Hao, Y.; Zhang, J.; Wang, H.; Yin, A.; Zhou, J.; Ma, X.; et al. Metal-Organic Frameworks with Photocatalytic Bactericidal Activity for Integrated Air Cleaning. *Nat. Commun.* **2019**, *10*, 2177. [[CrossRef](#)] [[PubMed](#)]
13. Fujishima, A.; Rao, T.N.; Tryk, D.A. Titanium Dioxide Photocatalysis. *J. Photochem. Photobiol. C: Photochem. Rev.* **2000**, *1*, 1–21. [[CrossRef](#)]
14. Rajeshwar, K.; Chenthamarakshan, C.R.; Goeringer, S.; Djukic, M. Titania-Based Heterogeneous Photocatalysis. Materials, Mechanistic Issues, and Implications for Environmental Remediation. *Pure Appl. Chem.* **2001**, *73*, 1849–1860. [[CrossRef](#)]
15. Diebold, U. The Surface Science of Titanium Dioxide. *Surf. Sci. Rep.* **2003**, *48*, 53–229. [[CrossRef](#)]
16. Chen, X.; Mao, S.S. Titanium Dioxide Nanomaterials: Synthesis, Properties, Modifications, and Applications. *Chem. Rev.* **2007**, *107*, 2891–2959. [[CrossRef](#)]
17. Henderson, M.A. A Surface Science Perspective on TiO<sub>2</sub> Photocatalysis. *Surf. Sci. Rep.* **2011**, *66*, 185–297. [[CrossRef](#)]
18. Dahl, M.; Liu, Y.; Yin, Y. Composite Titanium Dioxide Nanomaterials. *Chem. Rev.* **2014**, *114*, 9853–9889. [[CrossRef](#)]
19. Etacheri, V.; Di Valentin, C.; Schneider, J.; Bahnemann, D.; Pillai, S.C. Visible-Light Activation of TiO<sub>2</sub> Photocatalysts: Advances in Theory and Experiments. *J. Photochem. Photobiol. Photochem. Rev.* **2015**, *25*, 1–29. [[CrossRef](#)]
20. Al-Mamun, M.R.; Kader, S.; Islam, M.S.; Khan, M.Z.H. Photocatalytic Activity Improvement and Application of UV-TiO<sub>2</sub> Photocatalysis in Textile Wastewater Treatment: A Review. *J. Environ. Chem. Eng.* **2019**, *7*, 103248. [[CrossRef](#)]
21. Meng, A.; Zhang, L.; Cheng, B.; Yu, J. Dual Cocatalysts in TiO<sub>2</sub> Photocatalysis. *Adv. Mater.* **2019**, 1807660. [[CrossRef](#)]
22. Naldoni, A.; Altomare, M.; Zoppellaro, G.; Liu, N.; Kment, Š.; Zbořil, R.; Schmuki, P. Photocatalysis with Reduced TiO<sub>2</sub>: From Black TiO<sub>2</sub> to Cocatalyst-Free Hydrogen Production. *ACS Catal.* **2019**, *9*, 345–364. [[CrossRef](#)]
23. Likodimos, V. Photonic Crystal-Assisted Visible Light Activated TiO<sub>2</sub> Photocatalysis. *Appl. Catal. Environ.* **2018**, *230*, 269–303. [[CrossRef](#)]
24. Xu, C.; Ravi Anusuyadevi, P.; Aymonier, C.; Luque, R.; Marre, S. Nanostructured Materials for Photocatalysis. *Chem. Soc. Rev.* **2019**, *48*, 3868–3902. [[CrossRef](#)] [[PubMed](#)]
25. Peng, J.; Chen, X.; Ong, W.-J.; Zhao, X.; Li, N. Surface and Heterointerface Engineering of 2D MXenes and Their Nanocomposites: Insights into Electro- and Photocatalysis. *Chem* **2019**, *5*, 18–50. [[CrossRef](#)]
26. Dhakshinamoorthy, A.; Li, Z.; Garcia, H. Catalysis and Photocatalysis by Metal Organic Frameworks. *Chem. Soc. Rev.* **2018**, *47*, 8134–8172. [[CrossRef](#)] [[PubMed](#)]
27. Kapilashrami, M.; Zhang, Y.; Liu, Y.-S.; Hagfeldt, A.; Guo, J. Probing the Optical Property and Electronic Structure of TiO<sub>2</sub> Nanomaterials for Renewable Energy Applications. *Chem. Rev.* **2014**, *114*, 9662–9707. [[CrossRef](#)]
28. Grätzel, M. Photoelectrochemical Cells. *Nature* **2001**, *414*, 7. [[CrossRef](#)] [[PubMed](#)]
29. Carp, O. Photoinduced Reactivity of Titanium Dioxide. *Prog. Solid State Chem.* **2004**, *32*, 33–177. [[CrossRef](#)]
30. Ghicov, A.; Schmuki, P. Self-Ordering Electrochemistry: A Review on Growth and Functionality of TiO<sub>2</sub> nanotubes and Other Self-Aligned MO<sub>x</sub> Structures. *Chem. Commun.* **2009**, 2791–2808. [[CrossRef](#)]
31. Sanz, M.; Castillejo, M.; Amoroso, S.; Ausanio, G.; Bruzzese, R.; Wang, X. Ultra-Fast Laser Ablation and Deposition of TiO<sub>2</sub>. *Appl. Phys. A* **2010**, *101*, 639–644. [[CrossRef](#)]
32. Paramasivam, I.; Jha, H.; Liu, N.; Schmuki, P. A Review of Photocatalysis Using Self-Organized TiO<sub>2</sub> Nanotubes and Other Ordered Oxide Nanostructures. *Small* **2012**, *8*, 3073–3103. [[CrossRef](#)] [[PubMed](#)]
33. Tian, J.; Zhao, Z.; Kumar, A.; Boughton, R.I.; Liu, H. Recent Progress in Design, Synthesis, and Applications of One-Dimensional TiO<sub>2</sub> Nanostructured Surface Heterostructures: A Review. *Chem. Soc. Rev.* **2014**, *43*, 6920–6937. [[CrossRef](#)]
34. Pallotti, D.K.; Passoni, L.; Gesuele, F.; Maddalena, P.; Di Fonzo, F.; Lettieri, S. Giant O<sub>2</sub>-Induced Photoluminescence Modulation in Hierarchical Titanium Dioxide Nanostructures. *ACS Sens.* **2017**, *2*, 61–68. [[CrossRef](#)] [[PubMed](#)]
35. Kaur, N.; Singh, M.; Moumen, A.; Duina, G.; Comini, E. 1D Titanium Dioxide: Achievements in Chemical Sensing. *Materials* **2020**, *13*, 2974. [[CrossRef](#)]
36. Sanz, M.; López-Arias, M.; Marco, J.F.; De Nalda, R.; Amoroso, S.; Ausanio, G.; Lettieri, S.; Bruzzese, R.; Wang, X.; Castillejo, M. Ultrafast Laser Ablation and Deposition of Wide Band Gap Semiconductors. *J. Phys. Chem. C* **2011**, *115*, 3203–3211. [[CrossRef](#)]

37. Di Fonzo, F.; Casari, C.S.; Russo, V.; Brunella, M.F.; Li Bassi, A.; Bottani, C.E. Hierarchically Organized Nanostructured TiO<sub>2</sub> for Photocatalysis Applications. *Nanotechnology* **2009**, *20*, 015604. [[CrossRef](#)]
38. Kaempf, G.; Papenrot, W.; Holm, R. Degradation Processes in TiO<sub>2</sub>-Pigmented Paint Films on Exposure to Weathering. *J. Paint Technol.* **1974**, *46*, 56–63.
39. Van Driel, B.A.; Van den Berg, K.J.; Smout, M.; Dekker, N.; Kooyman, P.J.; Dik, J. Investigating the Effect of Artists' Paint Formulation on Degradation Rates of TiO<sub>2</sub>-Based Oil Paints. *Herit. Sci.* **2018**, *6*, 21. [[CrossRef](#)]
40. Artesani, A.; Mosca, S.; Dozzi, M.V.; Valentini, G.; Comelli, D. Determination of Crystal Phases in Mixed TiO<sub>2</sub> Paint Films by Non-Invasive Optical Spectroscopies. *Microchem. J.* **2020**, *155*, 104739. [[CrossRef](#)]
41. Rempelberg, C.; Heringa, M.B.; Van Donkersgoed, G.; Drijvers, J.; Roos, A.; Westenbrink, S.; Peters, R.; Van Bommel, G.; Brand, W.; Oomen, A.G. Oral Intake of Added Titanium Dioxide and Its Nanofraction from Food Products, Food Supplements and Toothpaste by the Dutch Population. *Nanotoxicology* **2016**, *10*, 1404–1414. [[CrossRef](#)] [[PubMed](#)]
42. Popov, A.P.; Priezzhev, A.V.; Lademann, J.; Myllyla, R. TiO<sub>2</sub> Nanoparticles as an Effective UV-B Radiation Skin-Protective Compound in Sunscreens. *J. Phys. D-Appl. Phys.* **2005**, *38*, 2564–2570. [[CrossRef](#)]
43. Jaroenworuluck, A.; Sunsaneeyametha, W.; Kosachan, N.; Stevens, R. Characteristics of Silica-Coated TiO<sub>2</sub> and Its UV Absorption for Sunscreen Cosmetic Applications. *Surf. Interface Anal.* **2006**, *38*, 473–477. [[CrossRef](#)]
44. Velimirovic, M.; Wagner, S.; Monikh, F.A.; Uusimaeki, T.; Kaegi, R.; Hofmann, T.; Von der Kammer, F. Accurate Quantification of TiO<sub>2</sub> Nanoparticles in Commercial Sunscreens Using Standard Materials and Orthogonal Particle Sizing Methods for verification. *Talanta* **2020**, *215*, 120921. [[CrossRef](#)]
45. Fujishima, A.; Honda, K. Electrochemical Photolysis of Water at a Semiconductor Electrode. *Nature* **1972**, *238*, 37–38. [[CrossRef](#)] [[PubMed](#)]
46. Renz, C. Lichtreaktionen Der Oxyde Des Titans, Cers Und Der Erdsäuren. *Helv. Chim. Acta* **1921**, *4*, 961–968. [[CrossRef](#)]
47. Jacobsen, A.E. Titanium Dioxide Pigments: Correlation between Photochemical Reactivity and Chalking. *Ind. Eng. Chem.* **1949**, *41*, 523–526. [[CrossRef](#)]
48. Baur, E.; Perret, A. Über Die Einwirkung von Licht Auf Gelöste Silbersalze in Gegenwart von Zinkoxyd. *Helv. Chim. Acta* **1924**, *7*, 910–915. [[CrossRef](#)]
49. Baur, E.; Neuweiler, C. Über Photolytische Bildung von Hydroperoxyd. *Helv. Chim. Acta* **1927**, *10*, 901–907. [[CrossRef](#)]
50. Renz, C. Über die Einwirkung von Oxyden auf Silbernitrat und Goldchlorid im Licht. *Helv. Chim. Acta* **1932**, *15*, 1077–1084. [[CrossRef](#)]
51. Goodeve, C.F.; Kitchener, J.A. Photosensitisation by Titanium Dioxide. *Trans. Faraday Soc.* **1938**, *34*, 570–579. [[CrossRef](#)]
52. Goodeve, C.F.; Kitchener, J.A. The Mechanism of Photosensitisation by Solids. *Trans. Faraday Soc.* **1938**, *34*, 902–908. [[CrossRef](#)]
53. Rubin, T.R.; Calvert, J.G.; Rankin, G.T.; MacNevin, W. Photochemical Synthesis of Hydrogen Peroxide at Zinc Oxide Surfaces. *J. Am. Chem. Soc.* **1953**, *75*, 2850–2853. [[CrossRef](#)]
54. Markham, M.C.; Laidler, K.J. A Kinetic Study of Photo-Oxidations on the Surface of Zinc Oxide in Aqueous Suspensions. *J. Phys. Chem.* **1953**, *57*, 363–369. [[CrossRef](#)]
55. Kennedy, D.R.; Ritchie, M.; Mackenzie, J. The Photosorption of Oxygen and Nitric Oxide on Titanium Dioxide. *Trans. Faraday Soc.* **1958**, *54*, 119–129. [[CrossRef](#)]
56. Filimonov, V.N. Photocatalytic Oxidation of Gaseous Isopropanol on ZnO and TiO<sub>2</sub>. *Dokl. Akad. Nauk SSSR* **1964**, *154*, 922–925.
57. McLintock, I.S.; Ritchie, M. Reactions on Titanium Dioxide; Photo-Adsorption and Oxidation of Ethylene and Propylene. *Trans. Faraday Soc.* **1965**, *61*, 1007–1016. [[CrossRef](#)]
58. Fujishima, A.; Honda, K. Evidence of Photosensitized Electrolytic Oxidation on TiO<sub>2</sub> Electrode from pH Change of Electrolyte Solution. *J. Soc. Chem. Ind. Jpn.* **1971**, *74*, 355–358. [[CrossRef](#)]
59. Frank, S.N.; Bard, A.J. Heterogeneous Photocatalytic Oxidation of Cyanide and Sulfite in Aqueous Solutions at Semiconductor Powders. *J. Phys. Chem.* **1977**, *81*, 1484–1488. [[CrossRef](#)]
60. Frank, S.N.; Bard, A.J. Heterogeneous Photocatalytic Oxidation of Cyanide Ion in Aqueous Solutions at Titanium Dioxide Powder. *J. Am. Chem. Soc.* **1977**, *99*, 303–304. [[CrossRef](#)]
61. Frank, S.N.; Bard, A.J. Semiconductor Electrodes. 12. Photoassisted Oxidations and Photoelectrosynthesis at Polycrystalline Titanium Dioxide Electrodes. *J. Am. Chem. Soc.* **1977**, *99*, 4667–4675. [[CrossRef](#)]
62. Singh, S.; Mahalingam, H.; Singh, P.K. Polymer-Supported Titanium Dioxide Photocatalysts for Environmental Remediation: A Review. *Appl. Catal. Gen.* **2013**, *462–463*, 178–195. [[CrossRef](#)]
63. Di Paola, A.; García-López, E.; Marci, G.; Palmisano, L. A Survey of Photocatalytic Materials for Environmental Remediation. *J. Hazard. Mater.* **2012**, *211–212*, 3–29. [[CrossRef](#)]
64. Ayati, A.; Ahmadpour, A.; Bamoharram, F.F.; Tanhaei, B.; Mänttari, M.; Sillanpää, M. A Review on Catalytic Applications of Au/TiO<sub>2</sub> Nanoparticles in the Removal of Water Pollutant. *Chemosphere* **2014**, *107*, 163–174. [[CrossRef](#)] [[PubMed](#)]
65. Varshney, G.; Kanel, S.R.; Kempisty, D.M.; Varshney, V.; Agrawal, A.; Sahle-Demessie, E.; Varma, R.S.; Nadagouda, M.N. Nanoscale TiO<sub>2</sub> Films and Their Application in Remediation of Organic Pollutants. *Coord. Chem. Rev.* **2016**, *306*, 43–64. [[CrossRef](#)]
66. Mamaghani, A.H.; Haghghat, F.; Lee, C.-S. Photocatalytic Oxidation Technology for Indoor Environment Air Purification: The State-of-the-Art. *Appl. Catal. Environ.* **2017**, *203*, 247–269. [[CrossRef](#)]
67. Boyjoo, Y.; Sun, H.; Liu, J.; Pareek, V.K.; Wang, S. A Review on Photocatalysis for Air Treatment: From Catalyst Development to Reactor Design. *Chem. Eng. J.* **2017**, *310*, 537–559. [[CrossRef](#)]

68. Tsang, C.H.A.; Li, K.; Zeng, Y.; Zhao, W.; Zhang, T.; Zhan, Y.; Xie, R.; Leung, D.Y.C.; Huang, H. Titanium Oxide Based Photocatalytic Materials Development and Their Role of in the Air Pollutants Degradation: Overview and Forecast. *Environ. Int.* **2019**, *125*, 200–228. [[CrossRef](#)]
69. Laxma Reddy, P.V.; Kavitha, B.; Kumar Reddy, P.A.; Kim, K.-H. TiO<sub>2</sub>-Based Photocatalytic Disinfection of Microbes in Aqueous Media: A Review. *Environ. Res.* **2017**, *154*, 296–303. [[CrossRef](#)] [[PubMed](#)]
70. Buchalska, M.; Kobielski, M.; Matuszek, A.; Pacia, M.; Wojtyła, S.; Macyk, W. On Oxygen Activation at Rutile- and Anatase-TiO<sub>2</sub>. *ACS Catal.* **2015**, *5*, 7424–7431. [[CrossRef](#)]
71. Di Paola, A.; Bellardita, M.; Palmisano, L. Brookite, the Least Known TiO<sub>2</sub> Photocatalyst. *Catalysts* **2013**, *3*, 36–73. [[CrossRef](#)]
72. Zhang, J.; Zhou, P.; Liu, J.; Yu, J. New Understanding of the Difference of Photocatalytic Activity among Anatase, Rutile and Brookite TiO<sub>2</sub>. *Phys. Chem. Chem. Phys.* **2014**, *16*, 20382–20386. [[CrossRef](#)]
73. Mutuma, B.K.; Shao, G.N.; Kim, W.D.; Kim, H.T. Sol-Gel Synthesis of Mesoporous Anatase-Brookite and Anatase-Brookite-Rutile TiO<sub>2</sub> Nanoparticles and Their Photocatalytic Properties. *J. Colloid Interface Sci.* **2015**, *442*, 1–7. [[CrossRef](#)] [[PubMed](#)]
74. Kavan, L.; Grätzel, M.; Gilbert, S.E.; Klemenčič, C.; Scheel, H.J. Electrochemical and Photoelectrochemical Investigation of Single-Crystal Anatase. *J. Am. Chem. Soc.* **1996**, *118*, 6716–6723. [[CrossRef](#)]
75. Samsonov, G.V. *The Oxide Handbook*; IFI Data Base Library; Springer US: New York, NY, USA, 1973; ISBN 978-1-4615-9599-1.
76. Leytner, S.; Hupp, J.T. Evaluation of the Energetics of Electron Trap States at the Nanocrystalline Titanium Dioxide/Aqueous Solution Interface via Time-Resolved Photoacoustic Spectroscopy. *Chem. Phys. Lett.* **2000**, *330*, 231–236. [[CrossRef](#)]
77. Siripala, W.; Tomkiewicz, M. Interactions Between Photoinduced and Dark Charge Transfer across n-TiO<sub>2</sub>-Aqueous Electrolyte Interface. *J. Electrochem. Soc.* **1982**, *129*, 1240–1245. [[CrossRef](#)]
78. Redmond, G.; Fitzmaurice, D.; Graetzel, M. Effect of Surface Chelation on the Energy of an Intraband Surface State of a Nanocrystalline Titania Film. *J. Phys. Chem.* **1993**, *97*, 6951–6954. [[CrossRef](#)]
79. Boschloo, G.K.; Goossens, A. Electron Trapping in Porphyrin-Sensitized Porous Nanocrystalline TiO<sub>2</sub> Electrodes. *J. Phys. Chem.* **1996**, *100*, 19489–19494. [[CrossRef](#)]
80. Boschloo, G.; Fitzmaurice, D. Spectroelectrochemical Investigation of Surface States in Nanostructured TiO<sub>2</sub> Electrodes. *J. Phys. Chem. B* **1999**, *103*, 2228–2231. [[CrossRef](#)]
81. Ikeda, S.; Sugiyama, N.; Murakami, S.; Kominami, H.; Kera, Y.; Noguchi, H.; Uosaki, K.; Torimoto, T.; Ohtani, B. Quantitative Analysis of Defective Sites in Titanium (IV) Oxide Photocatalyst Powders. *Phys. Chem. Chem. Phys.* **2003**, *5*, 778–783. [[CrossRef](#)]
82. Warren, D.S.; McQuillan, A.J. Influence of Adsorbed Water on Phonon and UV-Induced IR Absorptions of TiO<sub>2</sub> Photocatalytic Particle Films. *J. Phys. Chem. B* **2004**, *108*, 19373–19379. [[CrossRef](#)]
83. Rex, R.E.; Knorr, F.J.; McHale, J.L. Surface Traps of TiO<sub>2</sub> Nanosheets and Nanoparticles as Illuminated by Spectroelectrochemical Photoluminescence. *J. Phys. Chem. C* **2014**, *118*, 16831–16841. [[CrossRef](#)]
84. Hoffmann, M.R.; Martin, S.T.; Choi, W.; Bahnemann, D.W. Environmental Applications of Semiconductor Photocatalysis. *Chem. Rev.* **1995**, *95*, 69–96. [[CrossRef](#)]
85. Knorr, F.J.; Mercado, C.C.; McHale, J.L. Trap-State Distributions and Carrier Transport in Pure and Mixed-Phase TiO<sub>2</sub>: Influence of Contacting Solvent and Interphasial Electron Transfer. *J. Phys. Chem. C* **2008**, *112*, 12786–12794. [[CrossRef](#)]
86. Deskins, N.A.; Rousseau, R.; Dupuis, M. Distribution of Ti<sup>3+</sup> Surface Sites in Reduced TiO<sub>2</sub>. *J. Phys. Chem. C* **2011**, *115*, 7562–7572. [[CrossRef](#)]
87. Wallace, S.K.; McKenna, K.P. Facet-Dependent Electron Trapping in TiO<sub>2</sub> Nanocrystals. *J. Phys. Chem. C* **2015**, *119*, 1913–1920. [[CrossRef](#)]
88. Selcuk, S.; Selloni, A. Facet-Dependent Trapping and Dynamics of Excess Electrons at Anatase TiO<sub>2</sub> Surfaces and Aqueous Interfaces. *Nat. Mater.* **2016**, *15*, 1107–1112. [[CrossRef](#)]
89. Asahi, T.; Furube, A.; Masuhara, H. Direct Measurement of Picosecond Interfacial Electron Transfer from Photoexcited TiO<sub>2</sub> Powder to an Adsorbed Molecule in the Opaque Suspension. *Chem. Phys. Lett.* **1997**, *275*, 234–238. [[CrossRef](#)]
90. Mercado, C.C.; Knorr, F.J.; McHale, J.L.; Usmani, S.M.; Ichimura, A.S.; Saraf, L.V. Location of Hole and Electron Traps on Nanocrystalline Anatase TiO<sub>2</sub>. *J. Phys. Chem. C* **2012**, *116*, 10796–10804. [[CrossRef](#)]
91. Chiesa, M.; Paganini, M.C.; Livraghi, S.; Giamello, E. Charge Trapping in TiO<sub>2</sub> Polymorphs as Seen by Electron Paramagnetic Resonance Spectroscopy. *Phys. Chem. Chem. Phys.* **2013**, *15*, 9435–9447. [[CrossRef](#)]
92. Zawadzki, P. Absorption Spectra of Trapped Holes in Anatase TiO<sub>2</sub>. *J. Phys. Chem. C* **2013**, *117*, 8647–8651. [[CrossRef](#)]
93. Setvin, M.; Hao, X.; Daniel, B.; Pavelec, J.; Novotny, Z.; Parkinson, G.S.; Schmid, M.; Kresse, G.; Franchini, C.; Diebold, U. Charge Trapping at the Step Edges of TiO<sub>2</sub> Anatase (101). *Angew. Chem.-Int. Edit.* **2014**, *53*, 4714–4716. [[CrossRef](#)] [[PubMed](#)]
94. Carey, J.J.; McKenna, K.P. Does Polaronic Self-Trapping Occur at Anatase TiO<sub>2</sub> Surfaces? *J. Phys. Chem. C* **2018**, *122*, 27540–27553. [[CrossRef](#)]
95. Szczepankiewicz, S.H.; Moss, J.A.; Hoffmann, M.R. Electron Traps and the Stark Effect on Hydroxylated Titania Photocatalysts. *J. Phys. Chem. B* **2002**, *106*, 7654–7658. [[CrossRef](#)]
96. Henderson, M.A.; White, J.M.; Uetsuka, H.; Onishi, H. Photochemical Charge Transfer and Trapping at the Interface between an Organic Adlayer and an Oxide Semiconductor. *J. Am. Chem. Soc.* **2003**, *125*, 14974–14975. [[CrossRef](#)] [[PubMed](#)]
97. Uetsuka, H.; Onishi, H.; Henderson, M.A.; White, J.M. Photoinduced Redox Reaction Coupled with Limited Electron Mobility at Metal Oxide Surface. *J. Phys. Chem. B* **2004**, *108*, 10621–10624. [[CrossRef](#)]

98. Furube, A.; Asahi, T.; Masuhara, H.; Yamashita, H.; Anpo, M. Charge Carrier Dynamics of Standard TiO<sub>2</sub> Catalysts Revealed by Femtosecond Diffuse Reflectance Spectroscopy. *J. Phys. Chem. B* **1999**, *103*, 3120–3127. [[CrossRef](#)]
99. Jenkins, C.A.; Murphy, D.M. Thermal and Photoreactivity of TiO<sub>2</sub> at the Gas–Solid Interface with Aliphatic and Aromatic Aldehydes. *J. Phys. Chem. B* **1999**, *103*, 1019–1026. [[CrossRef](#)]
100. Chang, S.; Liu, W. Surface Doping Is More Beneficial than Bulk Doping to the Photocatalytic Activity of Vanadium-Doped TiO<sub>2</sub>. *Appl. Catal. B-Environ.* **2011**, *101*, 333–342. [[CrossRef](#)]
101. Li, J.; Zhang, M.; Guan, Z.; Li, Q.; He, C.; Yang, J. Synergistic Effect of Surface and Bulk Single-Electron-Trapped Oxygen Vacancy of TiO<sub>2</sub> in the Photocatalytic Reduction of CO<sub>2</sub>. *Appl. Catal. B-Environ.* **2017**, *206*, 300–307. [[CrossRef](#)]
102. Hou, L.; Guan, Z.; Zhang, M.; He, C.; Li, Q.; Yang, J. Adjusting the Ratio of Bulk Single-Electron-Trapped Oxygen Vacancies/Surface Oxygen Vacancies in TiO<sub>2</sub> for Efficient Photocatalytic Hydrogen Evolution. *Catal. Sci. Technol.* **2018**, *8*, 2809–2817. [[CrossRef](#)]
103. Kamei, M.; Miyagi, T.; Ishigaki, T. Strain-Induced Charge Separation in the Photocatalytic Single Crystalline Anatase TiO<sub>2</sub> Film. *Chem. Phys. Lett.* **2005**, *407*, 209–212. [[CrossRef](#)]
104. Pacchioni, G. Oxygen Vacancy: The Invisible Agent on Oxide Surfaces. *ChemPhysChem* **2003**, *4*, 1041–1047. [[CrossRef](#)]
105. Wendt, S.; Sprunger, P.T.; Lira, E.; Madsen, G.K.H.; Li, Z.; Hansen, J.O.; Matthiesen, J.; Blekinge-Rasmussen, A.; Laegsgaard, E.; Hammer, B.; et al. The Role of Interstitial Sites in the Ti3d Defect State in the Band Gap of Titania. *Science* **2008**, *320*, 1755–1759. [[CrossRef](#)] [[PubMed](#)]
106. Tachikawa, T.; Tojo, S.; Fujitsuka, M.; Sekino, T.; Majima, T. Photoinduced Charge Separation in Titania Nanotubes. *J. Phys. Chem. B* **2006**, *110*, 14055–14059. [[CrossRef](#)] [[PubMed](#)]
107. Corrent, S.; Cosa, G.; Scaiano, J.C.; Galletero, M.S.; Alvaro, M.; Garcia, H. Intrazeolite Photochemistry. 26. Photophysical Properties of Nanosized TiO<sub>2</sub> Clusters Included in Zeolites,  $\gamma$ ,  $\beta$ , and Mordenite. *Chem. Mater.* **2001**, *13*, 715–722. [[CrossRef](#)]
108. Huber, R.; Spörlein, S.; Moser, J.E.; Grätzel, M.; Wachtveitl, J. The Role of Surface States in the Ultrafast Photoinduced Electron Transfer from Sensitizing Dye Molecules to Semiconductor Colloids. *J. Phys. Chem. B* **2000**, *104*, 8995–9003. [[CrossRef](#)]
109. Kuznetsov, A.I.; Kameneva, O.; Rozes, L.; Sanchez, C.; Bityurin, N.; Kanaev, A. Extinction of Photo-Induced Ti<sup>3+</sup> Centres in Titanium Oxide Gels and Gel-Based oxo-PHEMA Hybrids. *Chem. Phys. Lett.* **2006**, *429*, 523–527. [[CrossRef](#)]
110. Yamada, Y.; Kanemitsu, Y. Determination of Electron and Hole Lifetimes of Rutile and Anatase TiO<sub>2</sub> Single Crystals. *Appl. Phys. Lett.* **2012**, *101*, 133907. [[CrossRef](#)]
111. Sa, J.; Friedli, P.; Geiger, R.; Lerch, P.; Rittmann-Frank, M.H.; Milne, C.J.; Szlachetko, J.; Santomauro, F.G.; Van Bokhoven, J.A.; Chergui, M.; et al. Transient Mid-IR Study of Electron Dynamics in TiO<sub>2</sub> Conduction Band. *Analyst* **2013**, *138*, 1966–1970. [[CrossRef](#)]
112. Peiró, A.M.; Colombo, C.; Doyle, G.; Nelson, J.; Mills, A.; Durrant, J.R. Photochemical Reduction of Oxygen Adsorbed to Nanocrystalline TiO<sub>2</sub> Films: A Transient Absorption and Oxygen Scavenging Study of Different TiO<sub>2</sub> Preparations. *J. Phys. Chem. B* **2006**, *110*, 23255–23263. [[CrossRef](#)] [[PubMed](#)]
113. Kormann, C.; Bahnemann, D.W.; Hoffmann, M.R. Preparation and Characterization of Quantum-Size Titanium Dioxide. *J. Phys. Chem.* **1988**, *92*, 5196–5201. [[CrossRef](#)]
114. Kuznetsov, A.I.; Kameneva, O.; Alexandrov, A.; Bityurin, N.; Marteau; Chhor, K.; Sanchez, C.; Kanaev, A. Light-Induced Charge Separation and Storage in Titanium Oxide Gels. *Phys. Rev. E* **2005**, *71*, 021403. [[CrossRef](#)] [[PubMed](#)]
115. Bityurin, N.; Kuznetsov, A.I.; Kanaev, A. Kinetics of UV-Induced Darkening of Titanium-Oxide Gels. *Appl. Surf. Sci.* **2005**, *248*, 86–90. [[CrossRef](#)]
116. Wang, H.; He, J.; Boschloo, G.; Lindström, H.; Hagfeldt, A.; Lindquist, S.-E. Electrochemical Investigation of Traps in a Nanostructured TiO<sub>2</sub> Film. *J. Phys. Chem. B* **2001**, *105*, 2529–2533. [[CrossRef](#)]
117. Katoh, R.; Murai, M.; Furube, A. Electron–Hole Recombination in the Bulk of a Rutile TiO<sub>2</sub> Single Crystal Studied by Sub-Nanosecond Transient Absorption Spectroscopy. *Chem. Phys. Lett.* **2008**, *461*, 238–241. [[CrossRef](#)]
118. Kerisit, S.; Deskins, N.A.; Rosso, K.M.; Dupuis, M. A Shell Model for Atomistic Simulation of Charge Transfer in Titania. *J. Phys. Chem. C* **2008**, *112*, 7678–7688. [[CrossRef](#)]
119. Shapovalov, V.; Stefanovich, E.V.; Truong, T.N. Nature of the Excited States of the Rutile TiO<sub>2</sub>(110) Surface with Adsorbed Water. *Surf. Sci.* **2002**, *498*, L103–L108. [[CrossRef](#)]
120. Dimitrijevic, N.M.; Saponjic, Z.V.; Rabatic, B.M.; Poluektov, O.G.; Rajh, T. Effect of Size and Shape of Nanocrystalline TiO<sub>2</sub> on Photogenerated Charges. An EPR Study. *J. Phys. Chem. C* **2007**, *111*, 14597–14601. [[CrossRef](#)]
121. Coronado, J.M.; Javier Maira, A.; Martínez-Arias, A.; Conesa, J.C.; Soria, J. EPR Study of the Radicals Formed upon UV Irradiation of Ceria-Based Photocatalysts. *J. Photochem. Photobiol. Chem.* **2002**, *150*, 213–221. [[CrossRef](#)]
122. Berger, T.; Sterrer, M.; Diwald, O.; Knözinger, E.; Panayotov, D.; Thompson, T.L.; Yates, J.T. Light-Induced Charge Separation in Anatase TiO<sub>2</sub> Particles. *J. Phys. Chem. B* **2005**, *109*, 6061–6068. [[CrossRef](#)] [[PubMed](#)]
123. Berger, T.; Sterrer, M.; Diwald, O.; Knözinger, E. Charge Trapping and Photoadsorption of O<sub>2</sub> on Dehydroxylated TiO<sub>2</sub> Nanocrystals? An Electron Paramagnetic Resonance Study. *ChemPhysChem* **2005**, *6*, 2104–2112. [[CrossRef](#)] [[PubMed](#)]
124. Yang, X.; Tamai, N. How Fast Is Interfacial Hole Transfer? In Situ Monitoring of Carrier Dynamics in Anatase TiO<sub>2</sub> Nanoparticles by Femtosecond Laser Spectroscopy. *Phys. Chem. Chem. Phys.* **2001**, *3*, 3393–3398. [[CrossRef](#)]

125. Tamaki, Y.; Furube, A.; Murai, M.; Hara, K.; Katoh, R.; Tachiya, M. Direct Observation of Reactive Trapped Holes in TiO<sub>2</sub> Undergoing Photocatalytic Oxidation of Adsorbed Alcohols: Evaluation of the Reaction Rates and Yields. *J. Am. Chem. Soc.* **2006**, *128*, 416–417. [[CrossRef](#)]
126. Tamaki, Y.; Furube, A.; Murai, M.; Hara, K.; Katoh, R.; Tachiya, M. Dynamics of Efficient Electron–Hole Separation in TiO<sub>2</sub> Nanoparticles Revealed by Femtosecond Transient Absorption Spectroscopy under the Weak-Excitation Condition. *Phys. Chem. Chem. Phys.* **2007**, *9*, 1453–1460. [[CrossRef](#)]
127. Yoshihara, T.; Katoh, R.; Furube, A.; Tamaki, Y.; Murai, M.; Hara, K.; Murata, S.; Arakawa, H.; Tachiya, M. Identification of Reactive Species in Photoexcited Nanocrystalline TiO<sub>2</sub> Films by Wide-Wavelength-Range (400–2500 nm) Transient Absorption Spectroscopy. *J. Phys. Chem. B* **2004**, *108*, 3817–3823. [[CrossRef](#)]
128. Rams, J.; Tejada, A.; Cabrera, J.M. Refractive Indices of Rutile as a Function of Temperature and Wavelength. *J. Appl. Phys.* **1997**, *82*, 994–997. [[CrossRef](#)]
129. DeVore, J.R. Refractive Indices of Rutile and Sphalerite. *J. Opt. Soc. Am. JOSA* **1951**, *41*, 416–419. [[CrossRef](#)]
130. Jellison, G.E.; Boatner, L.A.; Budai, J.D.; Jeong, B.-S.; Norton, D.P. Spectroscopic Ellipsometry of Thin Film and Bulk Anatase (TiO<sub>2</sub>). *J. Appl. Phys.* **2003**, *93*, 9537. [[CrossRef](#)]
131. Saha, D.; Ajimsha, R.S.; Rajiv, K.; Mukherjee, C.; Gupta, M.; Misra, P.; Kukreja, L.M. Spectroscopic Ellipsometry Characterization of Amorphous and Crystalline TiO<sub>2</sub> Thin Films Grown by Atomic Layer Deposition at Different Temperatures. *Appl. Surf. Sci.* **2014**, *315*, 116–123. [[CrossRef](#)]
132. Cronemeyer, D.C. Infrared Absorption of Reduced Rutile TiO<sub>2</sub> Single Crystals. *Phys. Rev.* **1959**, *113*, 1222–1226. [[CrossRef](#)]
133. Glassford, K.M.; Chelikowsky, J.R. Optical Properties of Titanium Dioxide in the Rutile Structure. *Phys. Rev. B* **1992**, *45*, 3874–3877. [[CrossRef](#)] [[PubMed](#)]
134. Tang, H.; Prasad, K.; Sanjinés, R.; Schmid, P.E.; Lévy, F. Electrical and Optical Properties of TiO<sub>2</sub> Anatase Thin Films. *J. Appl. Phys.* **1994**, *75*, 2042–2047. [[CrossRef](#)]
135. Tang, H.; Berger, H.; Schmid, P.E.; Lévy, F. Optical Properties of Anatase (TiO<sub>2</sub>). *Solid State Commun.* **1994**, *92*, 267–271. [[CrossRef](#)]
136. Tang, H.; Lévy, F.; Berger, H.; Schmid, P.E. Urbach Tail of Anatase TiO<sub>2</sub>. *Phys. Rev. B* **1995**, *52*, 7771–7774. [[CrossRef](#)] [[PubMed](#)]
137. Sekiya, T.; Igarashi, M.; Kurita, S.; Takekawa, S.; Fujisawa, M. Structure Dependence of Reflection Spectra of TiO<sub>2</sub> Single Crystals. *J. Electron Spectrosc. Relat. Phenom.* **1998**, *92*, 247–250. [[CrossRef](#)]
138. Tanemura, S.; Miao, L.; Jin, P.; Kaneko, K.; Terai, A.; Nabatova-Gabain, N. Optical Properties of Polycrystalline and Epitaxial Anatase and Rutile TiO<sub>2</sub> Thin Films by Rf Magnetron Sputtering. *Appl. Surf. Sci.* **2003**, *212–213*, 654–660. [[CrossRef](#)]
139. Itoh, C.; Iwahashi, K.; Kan’no, K. Photogeneration of Charge Carriers in Titanium Oxides. *Nucl. Instrum. Methods Phys. Res. Sect. Beam Interact. Mater. At.* **2002**, *191*, 271–274. [[CrossRef](#)]
140. Sumita, T.; Yamaki, T.; Yamamoto, S.; Miyashita, A. Photo-Induced Surface Charge Separation of Highly Oriented TiO<sub>2</sub> Anatase and Rutile Thin Films. *Appl. Surf. Sci.* **2002**, *200*, 21–26. [[CrossRef](#)]
141. Amtout, A.; Leonelli, R. Optical Properties of Rutile near Its Fundamental Band Gap. *Phys. Rev. B* **1995**, *51*, 6842–6851. [[CrossRef](#)]
142. Wang, Z.; Helmersson, U.; Käll, P.-O. Optical Properties of Anatase TiO<sub>2</sub> Thin Films Prepared by Aqueous Sol–Gel Process at Low Temperature. *Thin Solid Films* **2002**, *405*, 50–54. [[CrossRef](#)]
143. Hosaka, N.; Sekiya, T.; Fujisawa, M.; Satoko, C.; Kurita, S. UV Reflection Spectra of Anatase TiO<sub>2</sub>. *J. Electron Spectrosc. Relat. Phenom.* **1996**, *78*, 75–78. [[CrossRef](#)]
144. Kurita, D.; Ohta, S.; Sugiura, K.; Ohta, H.; Koumoto, K. Carrier Generation and Transport Properties of Heavily Nb-Doped Anatase TiO<sub>2</sub> Epitaxial Films at High Temperatures. *J. Appl. Phys.* **2006**, *100*, 096105. [[CrossRef](#)]
145. Ambrosone, G.; Coscia, U.; Lettieri, S.; Maddalena, P.; Minarini, C. Optical, Structural and Electrical Properties of Mc-Si:H Films Deposited by SiH<sub>4</sub>+H<sub>2</sub>. *Mater. Sci. Eng.* **2003**, *101*, 236–241. [[CrossRef](#)]
146. Asahi, R.; Taga, Y.; Mannstadt, W.; Freeman, A.J. Electronic and Optical Properties of Anatase TiO<sub>2</sub>. *Phys. Rev. B* **2000**, *61*, 7459–7465. [[CrossRef](#)]
147. Satoh, N.; Nakashima, T.; Kamikura, K.; Yamamoto, K. Quantum Size Effect in TiO<sub>2</sub> Nanoparticles Prepared by Finely Controlled Metal Assembly on Dendrimer Templates. *Nat. Nanotechnol.* **2008**, *3*, 106–111. [[CrossRef](#)]
148. Serpone, N.; Lawless, D.; Khairutdinov, R. Size Effects on the Photophysical Properties of Colloidal Anatase TiO<sub>2</sub> Particles: Size Quantization versus Direct Transitions in This Indirect Semiconductor? *J. Phys. Chem.* **1995**, *99*, 16646–16654. [[CrossRef](#)]
149. Monticone, S.; Tufeu, R.; Kanaev, A.V.; Scolan, E.; Sanchez, C. Quantum Size Effect in TiO<sub>2</sub> Nanoparticles: Does It Exist? *Appl. Surf. Sci.* **2000**, *162–163*, 565–570. [[CrossRef](#)]
150. Ricciardi, C.; Ballardini, V.; Galli, M.; Liscidini, M.; Andreani, L.C.; Losurdo, M.; Bruno, G.; Lettieri, S.; Gesuele, F.; Maddalena, P.; et al. Amorphous Silicon Nitride: A Suitable Alloy for Optical Multilayered Structures. *J. Non-Cryst. Solids* **2006**, *352*, 1294–1297. [[CrossRef](#)]
151. Passoni, L.; Criante, L.; Fumagalli, F.; Scotognella, F.; Lanzani, G.; Di Fonzo, F. Self-Assembled Hierarchical Nanostructures for High-Efficiency Porous Photonic Crystals. *ACS Nano* **2014**, *8*, 12167–12174. [[CrossRef](#)]
152. Chiarello, G.L.; Zuliani, A.; Ceresoli, D.; Martinazzo, R.; Selli, E. Exploiting the Photonic Crystal Properties of TiO<sub>2</sub> Nanotube Arrays To Enhance Photocatalytic Hydrogen Production. *ACS Catal.* **2016**, *6*, 1345–1353. [[CrossRef](#)]
153. Chiarello, G.L.; Aguirre, M.H.; Selli, E. Hydrogen Production by Photocatalytic Steam Reforming of Methanol on Noble Metal-Modified TiO<sub>2</sub>. *J. Catal.* **2010**, *273*, 182–190. [[CrossRef](#)]

154. Carotta, M.C.; Fioravanti, A.; Gherardi, S.; Malagù, C.; Sacerdoti, M.; Ghiotti, G.; Morandi, S. (Ti,Sn) Solid Solutions as Functional Materials for Gas Sensing. *Sens. Actuators Chem.* **2014**, *194*, 195–205. [[CrossRef](#)]
155. Yu, J.; Lei, J.; Wang, L.; Zhang, J.; Liu, Y. TiO<sub>2</sub> Inverse Opal Photonic Crystals: Synthesis, Modification, and Applications - A Review. *J. Alloys Compd.* **2018**, *769*, 740–757. [[CrossRef](#)]
156. Qi, D.; Lu, L.; Xi, Z.; Wang, L.; Zhang, J. Enhanced Photocatalytic Performance of TiO<sub>2</sub> Based on Synergistic Effect of Ti<sup>3+</sup> Self-Doping and Slow Light Effect. *Appl. Catal. Environ.* **2014**, *160–161*, 621–628. [[CrossRef](#)]
157. Corn, R.M.; Higgins, D.A. Optical Second Harmonic Generation as a Probe of Surface Chemistry. *Chem. Rev.* **1994**, *94*, 107–125. [[CrossRef](#)]
158. Borbone, F.; Carella, A.; Caruso, U.; Roviello, G.; Tuzi, A.; Dardano, P.; Lettieri, S.; Maddalena, P.; Barsella, A. Large Second-Order NLO Activity in Poly(4-Vinylpyridine) Grafted with PdII and CuII Chromophoric Complexes with Tridentate Bent Ligands Containing Heterocycles. *Eur. J. Inorg. Chem.* **2008**, *2008*, 1846–1853. [[CrossRef](#)]
159. Shen, Y.R. Basic Theory of Surface Sum-Frequency Generation. *J. Phys. Chem. C* **2012**, *116*, 15505–15509. [[CrossRef](#)]
160. Rubano, A.; Scigaj, M.; Sánchez, F.; Herranz, G.; Paparo, D. Optical Second Harmonic Generation from LaAlO<sub>3</sub>/SrTiO<sub>3</sub> Interfaces with Different in-Plane Anisotropies. *J. Phys. Condens. Matter* **2020**, *32*, 135001. [[CrossRef](#)]
161. Anpo, M.; Shima, T.; Kubokawa, Y. ESR and Photoluminescence Evidence for the Photocatalytic Formation of Hydroxyl Radicals on Small TiO<sub>2</sub> Particles. *Chem. Lett.* **1985**, *14*, 1799–1802. [[CrossRef](#)]
162. Anpo, M.; Aikawa, N.; Kubokawa, Y.; Che, M.; Louis, C.; Giamello, E. Photoluminescence and Photocatalytic Activity of Highly Dispersed Titanium Oxide Anchored onto Porous Vycor Glass. *J. Phys. Chem.* **1985**, *89*, 5017–5021. [[CrossRef](#)]
163. Anpo, M.; Yamada, Y.; Kubokawa, Y. Photoluminescence and Photocatalytic Activity of MgO Powders with Co-Ordinatively Unsaturated Surface Ions. *J. Chem. Soc. Chem. Commun.* **1986**, 714. [[CrossRef](#)]
164. Anpo, M.; Yamada, Y. Photoluminescence and Photocatalytic Activity of MgO Powders. *Mater. Chem. Phys.* **1988**, *18*, 465–484. [[CrossRef](#)]
165. Anpo, M.; Tomonari, M.; Fox, M.A. In Situ Photoluminescence of Titania as a Probe of Photocatalytic Reactions. *J. Phys. Chem.* **1989**, *93*, 7300–7302. [[CrossRef](#)]
166. Yu, P.Y.; Cardona, M. *Fundamentals of Semiconductors*; Graduate Texts in Physics; Springer: Heidelberg, Germany, 2010; ISBN 978-3-642-00709-5.
167. Forss, L.; Schubnell, M. Temperature Dependence of the Luminescence of TiO<sub>2</sub> Powder. *Appl. Phys. B* **1993**, *56*, 363–366. [[CrossRef](#)]
168. Ghosh, H.N.; Adhikari, S. Trap State Emission from TiO<sub>2</sub> Nanoparticles in Microemulsion Solutions. *Langmuir* **2001**, *17*, 4129–4130. [[CrossRef](#)]
169. Susha, A.S.; Lutich, A.A.; Liu, C.; Xu, H.; Zhang, R.; Zhong, Y.; Wong, K.S.; Yang, S.; Rogach, A.L. Comparative Optical Study of Colloidal Anatase Titania Nanorods and Atomically Thin Wires. *Nanoscale* **2013**, *5*, 1465. [[CrossRef](#)]
170. Cleary, O.; Purcell-Milton, F.; Vandekerckhove, A.; Gun'ko, Y.K. Chiral and Luminescent TiO<sub>2</sub> Nanoparticles. *Adv. Opt. Mater.* **2017**, *5*, 1601000. [[CrossRef](#)]
171. Paul, K.K.; Jana, S.; Giri, P.K. Tunable and High Photoluminescence Quantum Yield from Self-Decorated TiO<sub>2</sub> Quantum Dots on Fluorine Doped Mesoporous TiO<sub>2</sub> Flowers by Rapid Thermal Annealing. *Part. Part. Syst. Charact.* **2018**, *35*, 1800198. [[CrossRef](#)]
172. Gfroerer, T.H. Photoluminescence in Analysis of Surfaces and Interfaces. *Encycl. Anal. Chem.* **2000**.
173. Lettieri, S.; Santamaria Amato, L.; Maddalena, P.; Comini, E.; Baratto, C.; Todros, S. Recombination Dynamics of Deep Defect States in Zinc Oxide Nanowires. *Nanotechnology* **2009**, *20*, 175706. [[CrossRef](#)] [[PubMed](#)]
174. Dozzi, M.V.; D'Andrea, C.; Ohtani, B.; Valentini, G.; Selli, E. Fluorine-Doped TiO<sub>2</sub> Materials: Photocatalytic Activity vs Time-Resolved Photoluminescence. *J. Phys. Chem. C* **2013**, *117*, 25586–25595. [[CrossRef](#)]
175. Anpo, M.; Che, M. Applications of Photoluminescence Techniques to the Characterization of Solid Surfaces in Relation to Adsorption, Catalysis, and Photocatalysis. *Adv. Catal.* **1999**, *44*, 119–257.
176. Zhang, W.F.; Tang, J.; Ye, J. Photoluminescence and Photocatalytic Properties of SrSnO<sub>3</sub> Perovskite. *Chem. Phys. Lett.* **2006**, *418*, 174–178. [[CrossRef](#)]
177. Liqiang, J.; Yichun, Q.; Baiqi, W.; Shudan, L.; Baojiang, J.; Libin, Y.; Wei, F.; Honggang, F.; Jiazhong, S. Review of Photoluminescence Performance of Nano-Sized Semiconductor Materials and Its Relationships with Photocatalytic Activity. *Sol. Energy Mater. Sol. Cells* **2006**, *90*, 1773–1787. [[CrossRef](#)]
178. Bohle, D.S.; Spina, C.J. Cationic and Anionic Surface Binding Sites on Nanocrystalline Zinc Oxide: Surface Influence on Photoluminescence and Photocatalysis. *J. Am. Chem. Soc.* **2009**, *131*, 4397–4404. [[CrossRef](#)]
179. Coscia, U.; Ambrosone, G.; Lettieri, S.; Maddalena, P.; Rigato, V.; Restello, S.; Bobeico, E.; Tucci, M. Preparation of Microcrystalline Silicon–Carbon Films. *Sol. Energy Mater. Sol. Cells* **2005**, *87*, 433–444. [[CrossRef](#)]
180. Ruiz Peralta, M.D.L.; Pal, U.; Zeferino, R.S. Photoluminescence (PL) Quenching and Enhanced Photocatalytic Activity of Au-Decorated ZnO Nanorods Fabricated through Microwave-Assisted Chemical Synthesis. *ACS Appl. Mater. Interfaces* **2012**, *4*, 4807–4816. [[CrossRef](#)] [[PubMed](#)]
181. Mercado, C.; Seeley, Z.; Bandyopadhyay, A.; Bose, S.; McHale, J.L. Photoluminescence of Dense Nanocrystalline Titanium Dioxide Thin Films: Effect of Doping and Thickness and Relation to Gas Sensing. *ACS Appl. Mater. Interfaces* **2011**, *3*, 2281–2288. [[CrossRef](#)]
182. Knorr, F.J.; McHale, J.L. Spectroelectrochemical Photoluminescence of Trap States of Nanocrystalline TiO<sub>2</sub> in Aqueous Media. *J. Phys. Chem. C* **2013**, *117*, 13654–13662. [[CrossRef](#)]

183. Setaro, A.; Lettieri, S.; Diamare, D.; Maddalena, P.; Malagù, C.; Carotta, M.C.; Martinelli, G. Nanograined Anatase Titania-Based Optochemical Gas Detection. *New J. Phys.* **2008**, *10*, 053030. [[CrossRef](#)]
184. Williams, R.T.; Song, K.S. The Self-Trapped Exciton. *J. Phys. Chem. Solids* **1990**, *51*, 679–716. [[CrossRef](#)]
185. Varley, J.B.; Janotti, A.; Franchini, C.; Van de Walle, C.G. Role of Self-Trapping in Luminescence and p-Type Conductivity of Wide-Band-Gap Oxides. *Phys. Rev. B* **2012**, *85*, 081109. [[CrossRef](#)]
186. Pallotti, D.K.; Passoni, L.; Maddalena, P.; Di Fonzo, F.; Lettieri, S. Photoluminescence Mechanisms in Anatase and Rutile TiO<sub>2</sub>. *J. Phys. Chem. C* **2017**, *121*, 9011–9021. [[CrossRef](#)]
187. Mascaretti, L.; Russo, V.; Zoppellaro, G.; Lucotti, A.; Casari, C.S.; Kment, Š.; Naldoni, A.; Li Bassi, A. Excitation Wavelength- and Medium-Dependent Photoluminescence of Reduced Nanostructured TiO<sub>2</sub> Films. *J. Phys. Chem. C* **2019**, *123*, 11292–11303. [[CrossRef](#)]
188. Cavigli, L.; Bogani, F.; Vinattieri, A.; Faso, V.; Baldi, G. Volume versus Surface-Mediated Recombination in Anatase TiO<sub>2</sub> Nanoparticles. *J. Appl. Phys.* **2009**, *106*, 053516. [[CrossRef](#)]
189. Pallotti, D.K.; Orabona, E.; Amoruso, S.; Aruta, C.; Bruzzese, R.; Chiarella, F.; Tuzi, S.; Maddalena, P.; Lettieri, S. Multi-Band Photoluminescence in TiO<sub>2</sub> Nanoparticles-Assembled Films Produced by Femtosecond Pulsed Laser Deposition. *J. Appl. Phys.* **2013**, *114*, 043503. [[CrossRef](#)]
190. Setaro, A.; Bismuto, A.; Lettieri, S.; Maddalena, P.; Comini, E.; Bianchi, S.; Baratto, C.; Sberveglieri, G. Optical Sensing of NO<sub>2</sub> in Tin Oxide Nanowires at Sub-Ppm Level. *Sens. Actuators Chem.* **2008**, *130*, 391–395. [[CrossRef](#)]
191. Rex, R.E.; Yang, Y.; Knorr, F.J.; Zhang, J.Z.; Li, Y.; McHale, J.L. Spectroelectrochemical Photoluminescence of Trap States in H-Treated Rutile TiO<sub>2</sub> Nanowires: Implications for Photooxidation of Water. *J. Phys. Chem. C* **2016**, *120*, 3530–3541. [[CrossRef](#)]
192. McHale, J.L.; Rich, C.C.; Knorr, F.J. Trap State Photoluminescence of Nanocrystalline and Bulk TiO<sub>2</sub>: Implications for Carrier Transport. *MRS Proc.* **2010**, *1268*, EE03–EE08. [[CrossRef](#)]
193. Pallotti, D.; Orabona, E.; Amoruso, S.; Maddalena, P.; Lettieri, S. Modulation of Mixed-Phase Titania Photoluminescence by Oxygen Adsorption. *Appl. Phys. Lett.* **2014**, *105*, 031903. [[CrossRef](#)]
194. Pallotti, D.K.; Amoruso, S.; Orabona, E.; Maddalena, P.; Lettieri, S. Biparametric Optical Sensing of Oxygen by Titanium Dioxide. *Sens. Actuators B Chem.* **2015**, *221*, 515–520. [[CrossRef](#)]
195. Orabona, E.; Pallotti, D.; Fioravanti, A.; Gherardi, S.; Sacerdoti, M.; Carotta, M.C.; Maddalena, P.; Lettieri, S. On Mechanism of NO<sub>2</sub> Detection by ZnO Excitonic Luminescence. *Sens. Actuators B Chem.* **2015**, *210*, 706–711. [[CrossRef](#)]
196. Carotta, M.C.; Cervi, A.; Gherardi, S.; Guidi, V.; Malagu', C.; Martinelli, G.; Vendemiati, B.; Sacerdoti, M.; Ghiotti, G.; Morandi, S.; et al. (Ti, Sn)O<sub>2</sub> Solid Solutions for Gas Sensing: A Systematic Approach by Different Techniques for Different Calcination Temperature and Molar Composition. *Sens. Actuators B Chem.* **2009**, *139*, 329–339. [[CrossRef](#)]
197. Baratto, C.; Todros, S.; Faglia, G.; Comini, E.; Sberveglieri, G.; Lettieri, S.; Santamaria, L.; Maddalena, P. Luminescence Response of ZnO Nanowires to Gas Adsorption. *Sens. Actuators B Chem.* **2009**, *140*, 461–466. [[CrossRef](#)]
198. Lettieri, S.; Bismuto, A.; Maddalena, P.; Baratto, C.; Comini, E.; Faglia, G.; Sberveglieri, G.; Zanotti, L. Gas Sensitive Light Emission Properties of Tin Oxide and Zinc Oxide Nanobelts. *J. Non-Cryst. Solids* **2006**, *352*, 1457–1460. [[CrossRef](#)]
199. Lettieri, S.; Causà, M.; Setaro, A.; Trani, F.; Barone, V.; Ninno, D.; Maddalena, P. Direct Role of Surface Oxygen Vacancies in Visible Light Emission of Tin Dioxide Nanowires. *J. Chem. Phys.* **2008**, *129*, 244710. [[CrossRef](#)]
200. Lettieri, S.; Setaro, A.; Baratto, C.; Comini, E.; Faglia, G.; Sberveglieri, G.; Maddalena, P. On the Mechanism of Photoluminescence Quenching in Tin Dioxide Nanowires by NO<sub>2</sub> Adsorption. *New J. Phys.* **2008**, *10*, 043013. [[CrossRef](#)]
201. Trani, F.; Causà, M.; Lettieri, S.; Setaro, A.; Ninno, D.; Barone, V.; Maddalena, P. Role of Surface Oxygen Vacancies in Photoluminescence of Tin Dioxide Nanobelts. *Microelectron. J.* **2009**, *40*, 236–238. [[CrossRef](#)]
202. Valerini, D.; Creti, A.; Caricato, A.P.; Lomascolo, M.; Rella, R.; Martino, M. Optical Gas Sensing through Nanostructured ZnO Films with Different Morphologies. *Sens. Actuators B Chem.* **2010**, *145*, 167–173. [[CrossRef](#)]
203. Creti, A.; Valerini, D.; Taurino, A.; Quaranta, F.; Lomascolo, M.; Rella, R. Photoluminescence Quenching Processes by NO<sub>2</sub> Adsorption in ZnO Nanostructured Films. *J. Appl. Phys.* **2012**, *111*, 073520. [[CrossRef](#)]
204. Morandi, S.; Fioravanti, A.; Cerrato, G.; Lettieri, S.; Sacerdoti, M.; Carotta, M.C. Facile Synthesis of ZnO Nano-Structures: Morphology Influence on Electronic Properties. *Sens. Actuators B Chem.* **2017**, *249*, 581–589. [[CrossRef](#)]
205. Lettieri, S.; Gargiulo, V.; Alfè, M.; Amati, M.; Zeller, P.; Maraloiu, V.-A.; Borbone, F.; Pavone, M.; Muñoz-García, A.B.; Maddalena, P. Simple Ethanol Refluxing Method for Production of Blue-Colored Titanium Dioxide with Oxygen Vacancies and Visible Light-Driven Photocatalytic Properties. *J. Phys. Chem. C* **2020**, *124*, 3564–3576. [[CrossRef](#)]
206. Santara, B.; Giri, P.K.; Imakita, K.; Fujii, M. Evidence for Ti Interstitial Induced Extended Visible Absorption and Near Infrared Photoluminescence from Undoped TiO<sub>2</sub> Nanoribbons: An In Situ Photoluminescence Study. *J. Phys. Chem. C* **2013**, *117*, 23402–23411. [[CrossRef](#)]
207. Nakato, Y.; Akanuma, H.; Magari, Y.; Yae, S.; Shimizu, J.-I.; Mori, H. Photoluminescence from a Bulk Defect near the Surface of an *n*-TiO<sub>2</sub> (Rutile) Electrode in Relation to an Intermediate of Photooxidation Reaction of Water. *J. Phys. Chem. B* **1997**, *101*, 4934–4939. [[CrossRef](#)]
208. Nakamura, R.; Nakato, Y. Primary Intermediates of Oxygen Photoevolution Reaction on TiO<sub>2</sub> (Rutile) Particles, Revealed by in Situ FTIR Absorption and Photoluminescence Measurements. *J. Am. Chem. Soc.* **2004**, *126*, 1290–1298. [[CrossRef](#)] [[PubMed](#)]
209. Imanishi, A.; Okamura, T.; Ohashi, N.; Nakamura, R.; Nakato, Y. Mechanism of Water Photooxidation Reaction at Atomically Flat TiO<sub>2</sub> (Rutile) (110) and (100) Surfaces: Dependence on Solution PH. *J. Am. Chem. Soc.* **2007**, *10*. [[CrossRef](#)] [[PubMed](#)]

210. Vequizo, J.J.M.; Kamimura, S.; Ohno, T.; Yamakata, A. Oxygen Induced Enhancement of NIR Emission in Brookite TiO<sub>2</sub> Powders: Comparison with Rutile and Anatase TiO<sub>2</sub> Powders. *Phys. Chem. Chem. Phys.* **2018**, *20*, 3241–3248. [[CrossRef](#)]
211. Ma, S.; Reish, M.E.; Zhang, Z.; Harrison, I.; Yates, J.T. Anatase-Selective Photoluminescence Spectroscopy of P25 TiO<sub>2</sub> Nanoparticles: Different Effects of Oxygen Adsorption on the Band Bending of Anatase. *J. Phys. Chem. C* **2017**, *121*, 1263–1271. [[CrossRef](#)]
212. Onishi, H.; Iwasawa, Y. Dynamic Visualization of a Metal-Oxide-Surface/Gas-Phase Reaction: Time-Resolved Observation by Scanning Tunneling Microscopy at 800 K. *Phys. Rev. Lett.* **1996**, *76*, 791–794. [[CrossRef](#)]
213. Lettieri, S.; Pallotti, D.K.; Gesuele, F.; Maddalena, P. Unconventional Ratiometric-Enhanced Optical Sensing of Oxygen by Mixed-Phase TiO<sub>2</sub>. *Appl. Phys. Lett.* **2016**, *109*, 031905. [[CrossRef](#)]
214. Banerjee, S.; Dionysiou, D.D.; Pillai, S.C. Self-Cleaning Applications of TiO<sub>2</sub> by Photo-Induced Hydrophilicity and Photocatalysis. *Appl. Catal. B Environ.* **2015**, *176–177*, 396–428. [[CrossRef](#)]
215. Martin, S.T.; Herrmann, H.; Choi, W.; Hoffmann, M.R. Time-Resolved Microwave Conductivity. Part 1—TiO<sub>2</sub> Photoreactivity and Size Quantization. *J. Chem. Soc. Faraday Trans.* **1994**, *90*, 3315–3322. [[CrossRef](#)]
216. Martin, S.T.; Herrmann, H.; Hoffmann, M.R. Time-Resolved Microwave Conductivity. Part 2—Quantum-Sized TiO<sub>2</sub> and the Effect of Adsorbates and Light Intensity on Charge-Carrier Dynamics. *J. Chem. Soc. Faraday Trans.* **1994**, *90*, 3323–3330. [[CrossRef](#)]
217. Schneider, J.; Matsuoka, M.; Takeuchi, M.; Zhang, J.; Horiuchi, Y.; Anpo, M.; Bahnemann, D.W. Understanding TiO<sub>2</sub> Photocatalysis: Mechanisms and Materials. *Chem. Rev.* **2014**, *114*, 9919–9986. [[CrossRef](#)]
218. Dong, S.; Feng, J.; Fan, M.; Pi, Y.; Hu, L.; Han, X.; Liu, M.; Sun, J.; Sun, J. Recent Developments in Heterogeneous Photocatalytic Water Treatment Using Visible Light-Responsive Photocatalysts: A Review. *RSC Adv.* **2015**, *5*, 14610–14630. [[CrossRef](#)]
219. Fragalà, M.E.; Malandrino, G.; Giangregorio, M.M.; Losurdo, M.; Bruno, G.; Lettieri, S.; Amato, L.S.; Maddalena, P. Structural, Optical, and Electrical Characterization of ZnO and Al-Doped ZnO Thin Films Deposited by MOCVD. *Chem. Vapor Depos.* **2009**, *15*, 327–333. [[CrossRef](#)]
220. Gerischer, H. Electron-Transfer Kinetics of Redox Reactions at the Semiconductor/Electrolyte Contact. A New Approach. *J. Phys. Chem.* **1991**, *95*, 1356–1359. [[CrossRef](#)]
221. Wang, C.M.; Heller, A.; Gerischer, H. Palladium Catalysis of O<sub>2</sub> Reduction by Electrons Accumulated on TiO<sub>2</sub> Particles during Photoassisted Oxidation of Organic Compounds. *J. Am. Chem. Soc.* **1992**, *114*, 5230–5234. [[CrossRef](#)]
222. Hoffman, A.J.; Carraway, E.R.; Hoffmann, M.R. Photocatalytic Production of H<sub>2</sub>O<sub>2</sub> and Organic Peroxides on Quantum-Sized Semiconductor Colloids. *Environ. Sci. Technol.* **1994**, *28*, 776–785. [[CrossRef](#)]
223. Ollis, D. Heterogeneous Photoassisted Catalysis: Conversions of Perchloroethylene, Dichloroethane, Chloroacetic Acids, and Chlorobenzenes. *J. Catal.* **1984**, *88*, 89–96. [[CrossRef](#)]
224. Augugliaro, V.; Palmisano, L.; Sclafani, A.; Minero, C.; Pelizzetti, E. Photocatalytic Degradation of Phenol in Aqueous Titanium Dioxide Dispersions. *Toxicol. Environ. Chem.* **1988**, *16*, 89–109. [[CrossRef](#)]
225. Turchi, C. Mixed Reactant Photocatalysis: Intermediates and Mutual Rate Inhibition. *J. Catal.* **1989**, *119*, 483–496. [[CrossRef](#)]
226. Turchi, C. Photocatalytic Degradation of Organic Water Contaminants: Mechanisms Involving Hydroxyl Radical Attack. *J. Catal.* **1990**, *122*, 178–192. [[CrossRef](#)]
227. Jaeger, C.D.; Bard, A.J. Spin Trapping and Electron Spin Resonance Detection of Radical Intermediates in the Photodecomposition of Water at Titanium Dioxide Particulate Systems. *J. Phys. Chem.* **1979**, *83*, 3146–3152. [[CrossRef](#)]
228. Mao, Y.; Schoeneich, C.; Asmus, K.D. Identification of Organic Acids and Other Intermediates in Oxidative Degradation of Chlorinated Ethanes on Titania Surfaces En Route to Mineralization: A Combined Photocatalytic and Radiation Chemical Study. *J. Phys. Chem.* **1991**, *95*, 10080–10089. [[CrossRef](#)]
229. Draper, R.B.; Fox, M.A. Titanium Dioxide Photosensitized Reactions Studied by Diffuse Reflectance Flash Photolysis in Aqueous Suspensions of TiO<sub>2</sub> Powder. *Langmuir* **1990**, *6*, 1396–1402. [[CrossRef](#)]
230. Carraway, E.R.; Hoffman, A.J.; Hoffmann, M.R. Photocatalytic Oxidation of Organic Acids on Quantum-Sized Semiconductor Colloids. *Environ. Sci. Technol.* **1994**, *28*, 786–793. [[CrossRef](#)]
231. Lettieri, S.; Gargiulo, V.; Pallotti, D.K.; Vitiello, G.; Maddalena, P.; Alfè, M.; Marotta, R. Evidencing Opposite Charge-Transfer Processes at TiO<sub>2</sub>/Graphene-Related Materials Interface through a Combined EPR, Photoluminescence and Photocatalysis Assessment. *Catal. Today* **2018**, *315*, 19–30. [[CrossRef](#)]
232. Li, X.; Yu, J.; Jaroniec, M.; Chen, X. Cocatalysts for Selective Photoreduction of CO<sub>2</sub> into Solar Fuels. *Chem. Rev.* **2019**, *218*.
233. Pan, X.; Yang, M.-Q.; Fu, X.; Zhang, N.; Xu, Y.-J. Defective TiO<sub>2</sub> with Oxygen Vacancies: Synthesis, Properties and Photocatalytic Applications. *Nanoscale* **2013**, *5*, 3601. [[CrossRef](#)] [[PubMed](#)]
234. Katal, R.; Masudy-Panah, S.; Tanhaei, M.; Farahani, M.H.D.A.; Jiangyong, H. A Review on the Synthesis of the Various Types of Anatase TiO<sub>2</sub> Facets and Their Applications for Photocatalysis. *Chem. Eng. J.* **2020**, *384*, 123384. [[CrossRef](#)]
235. Xu, Q.; Zhang, L.; Yu, J.; Wageh, S.; Al-Ghamdi, A.A.; Jaroniec, M. Direct Z-Scheme Photocatalysts: Principles, Synthesis, and Applications. *Mater. Today* **2018**, *21*, 1042–1063. [[CrossRef](#)]
236. Chen, X.; Liu, L.; Yu, P.Y.; Mao, S.S. Increasing Solar Absorption for Photocatalysis with Black Hydrogenated Titanium Dioxide Nanocrystals. *Science* **2011**, *331*, 746–750. [[CrossRef](#)] [[PubMed](#)]
237. Naldoni, A.; Allietta, M.; Santangelo, S.; Marelli, M.; Fabbri, F.; Cappelli, S.; Bianchi, C.L.; Psaro, R.; Dal Santo, V. Effect of Nature and Location of Defects on Bandgap Narrowing in Black TiO<sub>2</sub> Nanoparticles. *J. Am. Chem. Soc.* **2012**, *134*, 7600–7603. [[CrossRef](#)] [[PubMed](#)]

238. Chen, X.; Liu, L.; Huang, F. Black Titanium Dioxide (TiO<sub>2</sub>) Nanomaterials. *Chem. Soc. Rev.* **2015**, *44*, 1861–1885. [[CrossRef](#)] [[PubMed](#)]
239. Zhou, X.; Liu, N.; Schmuki, P. Photocatalysis with TiO<sub>2</sub> Nanotubes: “Colorful” Reactivity and Designing Site-Specific Photocatalytic Centers into TiO<sub>2</sub> Nanotubes. *ACS Catal.* **2017**, *7*, 3210–3235. [[CrossRef](#)]
240. Hao, Z.; Chen, Q.; Dai, W.; Ren, Y.; Zhou, Y.; Yang, J.; Xie, S.; Shen, Y.; Wu, J.; Chen, W.; et al. Oxygen-Deficient Blue TiO<sub>2</sub> for Ultrastable and Fast Lithium Storage. *Adv. Energy Mater.* **2020**, *10*, 1903107. [[CrossRef](#)]
241. Liu, N.; Steinrück, H.-G.; Osvet, A.; Yang, Y.; Schmuki, P. Noble Metal Free Photocatalytic H<sub>2</sub> Generation on Black TiO<sub>2</sub>: On the Influence of Crystal Facets vs. Crystal Damage. *Appl. Phys. Lett.* **2017**, *5*. [[CrossRef](#)]
242. Pore, V.; Ritala, M.; Leskelä, M.; Areva, S.; Järn, M.; Järnström, J. H<sub>2</sub> S Modified Atomic Layer Deposition Process for Photocatalytic TiO<sub>2</sub> Thin Films. *J. Mater. Chem.* **2007**, *17*, 1361–1371. [[CrossRef](#)]
243. Liu, N.; Schneider, C.; Freitag, D.; Hartmann, M.; Venkatesan, U.; Müller, J.; Spiecker, E.; Schmuki, P. Black TiO<sub>2</sub> Nanotubes: Cocatalyst-Free Open-Circuit Hydrogen Generation. *Nano Lett.* **2014**, *14*, 3309–3313. [[CrossRef](#)]
244. Liu, N.; Häublein, V.; Zhou, X.; Venkatesan, U.; Hartmann, M.; Mačković, M.; Nakajima, T.; Spiecker, E.; Osvet, A.; Frey, L.; et al. “Black” TiO<sub>2</sub> Nanotubes Formed by High-Energy Proton Implantation Show Noble-Metal-co-Catalyst Free Photocatalytic H<sub>2</sub>-Evolution. *Nano Lett.* **2015**, *15*, 6815–6820. [[CrossRef](#)] [[PubMed](#)]
245. Liu, N.; Schneider, C.; Freitag, D.; Zolnhofer, E.M.; Meyer, K.; Schmuki, P. Noble-Metal-Free Photocatalytic H<sub>2</sub> Generation: Active and Inactive ‘Black’ TiO<sub>2</sub> Nanotubes and Synergistic Effects. *Chem. Eur. J.* **2016**, *5*. [[CrossRef](#)] [[PubMed](#)]
246. Liu, N.; Zhou, X.; Nguyen, N.T.; Peters, K.; Zoller, F.; Hwang, I.; Schneider, C.; Miehl, M.E.; Freitag, D.; Meyer, K.; et al. Black Magic in Gray Titania: Noble-Metal-Free Photocatalytic H<sub>2</sub> Evolution from Hydrogenated Anatase. *ChemSusChem* **2017**, *10*, 62–67. [[CrossRef](#)] [[PubMed](#)]
247. Wu, Q.; Huang, F.; Zhao, M.; Xu, J.; Zhou, J.; Wang, Y. Ultra-Small Yellow Defective TiO<sub>2</sub> Nanoparticles for co-Catalyst Free Photocatalytic Hydrogen Production. *Nano Energy* **2016**, *24*, 63–71. [[CrossRef](#)]
248. Kong, L.; Jiang, Z.; Wang, C.; Wan, F.; Li, Y.; Wu, L.; Zhi, J.-F.; Zhang, X.; Chen, S.; Liu, Y. Simple Ethanol Impregnation Treatment Can Enhance Photocatalytic Activity of TiO<sub>2</sub> Nanoparticles under Visible-Light Irradiation. *ACS Appl. Mater. Interfaces* **2015**, *7*, 7752–7758. [[CrossRef](#)]
249. Wang, L.; Cai, Y.; Liu, B.; Dong, L. A Facile Synthesis of Brown Anatase TiO<sub>2</sub> Rich in Oxygen Vacancies and Its Visible Light Photocatalytic Property. *Solid State Ion.* **2021**, *361*, 115564. [[CrossRef](#)]
250. Jiang, N.; Du, Y.; Liu, S.; Du, M.; Feng, Y.; Liu, Y. Facile Preparation of Flake-like Blue TiO<sub>2</sub> Nanorod Arrays for Efficient Visible Light Photocatalyst. *Ceram. Int.* **2019**, *45*, 9754–9760. [[CrossRef](#)]
251. Zheng, J.; Ji, G.; Zhang, P.; Cao, X.; Wang, B.; Yu, L.; Xu, Z. Facile Aluminum Reduction Synthesis of Blue TiO<sub>2</sub> with Oxygen Deficiency for Lithium-Ion Batteries. *Chem. Eur. J.* **2015**, *21*, 18309–18315. [[CrossRef](#)]
252. Ariyanti, D.; Mills, L.; Dong, J.; Yao, Y.; Gao, W. NaBH<sub>4</sub> Modified TiO<sub>2</sub>: Defect Site Enhancement Related to Its Photocatalytic Activity. *Mater. Chem. Phys.* **2017**, *199*, 571–576. [[CrossRef](#)]
253. Ullattil, S.G.; Narendranath, S.B.; Pillai, S.C.; Periyat, P. Black TiO<sub>2</sub> Nanomaterials: A Review of Recent Advances. *Chem. Eng. J.* **2018**, *343*, 708–736. [[CrossRef](#)]
254. Mun Wong, K.; Alay-e-Abbas, S.M.; Fang, Y.; Shaikat, A.; Lei, Y. Spatial Distribution of Neutral Oxygen Vacancies on ZnO Nanowire Surfaces: An Investigation Combining Confocal Microscopy and First Principles Calculations. *J. Appl. Phys.* **2013**, *114*, 034901. [[CrossRef](#)]
255. Ohno, T.; Sarukawa, K.; Matsumura, M. Crystal Faces of Rutile and Anatase TiO<sub>2</sub> Particles and Their Roles in Photocatalytic Reactions. *New J. Chem.* **2002**, *26*, 1167–1170. [[CrossRef](#)]
256. Lazzeri, M.; Vittadini, A.; Selloni, A. Structure and Energetics of Stoichiometric TiO<sub>2</sub> Anatase Surfaces. *Phys. Rev. B* **2001**, *63*, 155409. [[CrossRef](#)]
257. Yang, H.G.; Sun, C.H.; Qiao, S.Z.; Zou, J.; Liu, G.; Smith, S.C.; Cheng, H.M.; Lu, G.Q. Anatase TiO<sub>2</sub> Single Crystals with a Large Percentage of Reactive Facets. *Nature* **2008**, *453*, 638–641. [[CrossRef](#)]
258. Dinh, C.-T.; Nguyen, T.-D.; Kleitz, F.; Do, T.-O. Shape-Controlled Synthesis of Highly Crystalline Titania Nanocrystals. *ACS Nano* **2009**, *3*, 3737–3743. [[CrossRef](#)] [[PubMed](#)]
259. D’Arienzo, M.; Carbajo, J.; Bahamonde, A.; Crippa, M.; Polizzi, S.; Scotti, R.; Wahba, L.; Morazzoni, F. Photogenerated Defects in Shape-Controlled TiO<sub>2</sub> Anatase Nanocrystals: A Probe To Evaluate the Role of Crystal Facets in Photocatalytic Processes. *J. Am. Chem. Soc.* **2011**, *133*, 17652–17661. [[CrossRef](#)]
260. Pan, J.; Liu, G.; Lu, G.Q.M.; Cheng, H.-M. On the True Photoreactivity Order of {001}, {010}, and {101} Facets of Anatase TiO<sub>2</sub> Crystals. *Angew. Chem. Int. Ed.* **2011**, *50*, 2133–2137. [[CrossRef](#)]
261. Tachikawa, T.; Yamashita, S.; Majima, T. Evidence for Crystal-Face-Dependent TiO<sub>2</sub> Photocatalysis from Single-Molecule Imaging and Kinetic Analysis. *J. Am. Chem. Soc.* **2011**, *133*, 7197–7204. [[CrossRef](#)]
262. Wu, X.; Chen, Z.; Lu, G.Q.M.; Wang, L. Nanosized Anatase TiO<sub>2</sub> Single Crystals with Tunable Exposed (001) Facets for Enhanced Energy Conversion Efficiency of Dye-Sensitized Solar Cells. *Adv. Funct. Mater.* **2011**, *21*, 4167–4172. [[CrossRef](#)]
263. Dozzi, M.; Selli, E. Specific Facets-Dominated Anatase TiO<sub>2</sub>: Fluorine-Mediated Synthesis and Photoactivity. *Catalysts* **2013**, *3*, 455–485. [[CrossRef](#)]
264. Ong, W.-J.; Tan, L.-L.; Chai, S.-P.; Yong, S.-T.; Mohamed, A.R. Facet-Dependent Photocatalytic Properties of TiO<sub>2</sub>-Based Composites for Energy Conversion and Environmental Remediation. *ChemSusChem* **2014**, *7*, 690–719. [[CrossRef](#)] [[PubMed](#)]

265. Yu, J.; Low, J.; Xiao, W.; Zhou, P.; Jaroniec, M. Enhanced Photocatalytic CO<sub>2</sub>-Reduction Activity of Anatase TiO<sub>2</sub> by Coexposed {001} and {101} Facets. *J. Am. Chem. Soc.* **2014**, *136*, 8839–8842. [[CrossRef](#)]
266. D'Arienzo, M.; Dozzi, M.V.; Redaelli, M.; Credico, B.D.; Morazzoni, F.; Scotti, R.; Polizzi, S. Crystal Surfaces and Fate of Photogenerated Defects in Shape-Controlled Anatase Nanocrystals: Drawing Useful Relations to Improve the H<sub>2</sub> Yield in Methanol Photosteam Reforming. *J. Phys. Chem. C* **2015**, *119*, 12385–12393. [[CrossRef](#)]
267. Kashiwaya, S.; Toupance, T.; Klein, A.; Jaegermann, W. Fermi Level Positions and Induced Band Bending at Single Crystalline Anatase (101) and (001) Surfaces: Origin of the Enhanced Photocatalytic Activity of Facet Engineered Crystals. *Adv. Energy Mater.* **2018**, *8*, 1802195. [[CrossRef](#)]
268. Peng, Y.-K.; Tsang, S.C.E. Facet-Dependent Photocatalysis of Nanosize Semiconductive Metal Oxides and Progress of Their Characterization. *Nano Today* **2018**, *18*, 15–34. [[CrossRef](#)]
269. Zhang, L.; Shi, J.; Liu, M.; Jing, D.; Guo, L. Photocatalytic Reforming of Glucose under Visible Light over Morphology Controlled Cu<sub>2</sub>O: Efficient Charge Separation by Crystal Facet Engineering. *Chem. Commun.* **2014**, *50*, 192–194. [[CrossRef](#)]
270. Wang, S.; Chen, H.; Gao, G.; Butburee, T.; Lyu, M.; Thaweesak, S.; Yun, J.-H.; Du, A.; Liu, G.; Wang, L. Synergistic Crystal Facet Engineering and Structural Control of WO<sub>3</sub> Films Exhibiting Unprecedented Photoelectrochemical Performance. *Nano Energy* **2016**, *24*, 94–102. [[CrossRef](#)]
271. Li, R.; Zhang, F.; Wang, D.; Yang, J.; Li, M.; Zhu, J.; Zhou, X.; Han, H.; Li, C. Spatial Separation of Photogenerated Electrons and Holes among {010} and {110} Crystal Facets of BiVO<sub>4</sub>. *Nat. Commun.* **2013**, *4*, 1432. [[CrossRef](#)]
272. Michaelson, H.B. The Work Function of the Elements and Its Periodicity. *J. Appl. Phys.* **1977**, *48*, 6. [[CrossRef](#)]
273. Nørskov, J.K.; Bligaard, T.; Logadottir, A.; Kitchin, J.R.; Chen, J.G.; Pandelov, S.; Stimming, U. Trends in the Exchange Current for Hydrogen Evolution. *J. Electrochem. Soc.* **2005**, *5*. [[CrossRef](#)]
274. Kavitha, R.; Kumar, S.G. A Review on Plasmonic Au-ZnO Heterojunction Photocatalysts: Preparation, Modifications and Related Charge Carrier Dynamics. *Mater. Sci. Semicond. Process.* **2019**, *93*, 59–91. [[CrossRef](#)]
275. Truppi, A.; Petronella, F.; Placido, T.; Margiotta, V.; Lasorella, G.; Giotta, L.; Giannini, C.; Sibillano, T.; Murgolo, S.; Mascolo, G.; et al. Gram-Scale Synthesis of UV-Vis Light Active Plasmonic Photocatalytic Nanocomposite Based on TiO<sub>2</sub>/Au Nanorods for Degradation of Pollutants in Water. *Appl. Catal. B Environ.* **2019**, *243*, 604–613. [[CrossRef](#)]
276. Zhang, Z.; Li, A.; Cao, S.-W.; Bosman, M.; Li, S.; Xue, C. Direct Evidence of Plasmon Enhancement on Photocatalytic Hydrogen Generation over Au/Pt-Decorated TiO<sub>2</sub> Nanofibers. *Nanoscale* **2014**, *6*, 5217–5222. [[CrossRef](#)]
277. Tanaka, A.; Sakaguchi, S.; Hashimoto, K.; Kominami, H. Preparation of Au/TiO<sub>2</sub> with Metal Cocatalysts Exhibiting Strong Surface Plasmon Resonance Effective for Photoinduced Hydrogen Formation under Irradiation of Visible Light. *ACS Catal.* **2013**, *3*, 79–85. [[CrossRef](#)]
278. Zhang, Z.; Wang, Z.; Cao, S.-W.; Xue, C. Au/Pt Nanoparticle-Decorated TiO<sub>2</sub> Nanofibers with Plasmon-Enhanced Photocatalytic Activities for Solar-to-Fuel Conversion. *J. Phys. Chem. C* **2013**, *117*, 25939–25947. [[CrossRef](#)]
279. Chen, C.; Kuai, L.; Chen, Y.; Wang, Q.; Kan, E.; Geng, B. Au/Pt Co-Loaded Ultrathin TiO<sub>2</sub> Nanosheets for Photocatalyzed H<sub>2</sub> Evolution by the Synergistic Effect of Plasmonic Enhancement and co-Catalysis. *RSC Adv.* **2015**, *5*, 98254–98259. [[CrossRef](#)]
280. Bera, S.; Lee, J.E.; Rawal, S.B.; Lee, W.I. Size-Dependent Plasmonic Effects of Au and Au@SiO<sub>2</sub> Nanoparticles in Photocatalytic CO<sub>2</sub> Conversion Reaction of Pt/TiO<sub>2</sub>. *Appl. Catal. B Environ.* **2016**, *199*, 55–63. [[CrossRef](#)]
281. Lalitha, K.; Sadanandam, G.; Kumari, V.D.; Subrahmanyam, M.; Sreedhar, B.; Hebalkar, N.Y. Highly Stabilized and Finely Dispersed Cu<sub>2</sub>O/TiO<sub>2</sub>: A Promising Visible Sensitive Photocatalyst for Continuous Production of Hydrogen from Glycerol:Water Mixtures. *J. Phys. Chem. C* **2010**, *114*, 22181–22189. [[CrossRef](#)]
282. Li, L.; Xu, L.; Shi, W.; Guan, J. Facile Preparation and Size-Dependent Photocatalytic Activity of Cu<sub>2</sub>O Nanocrystals Modified Titania for Hydrogen Evolution. *Int. J. Hydrog. Energy* **2013**, *38*, 816–822. [[CrossRef](#)]
283. Xi, Z.; Li, C.; Zhang, L.; Xing, M.; Zhang, J. Synergistic Effect of Cu<sub>2</sub>O/TiO<sub>2</sub> Heterostructure Nanoparticle and Its High H<sub>2</sub> Evolution Activity. *Int. J. Hydrog. Energy* **2014**, *39*, 6345–6353. [[CrossRef](#)]
284. Minami, T.; Nishi, Y.; Miyata, T. Cu<sub>2</sub>O-Based Solar Cells Using Oxide Semiconductors. *J. Semicond.* **2016**, *37*, 014002. [[CrossRef](#)]
285. Luévano-Hipólito, E.; Torres-Martínez, L.M.; Sánchez-Martínez, D.; Alfaro Cruz, M.R. Cu<sub>2</sub>O Precipitation-Assisted with Ultrasound and Microwave Radiation for Photocatalytic Hydrogen Production. *Int. J. Hydrog. Energy* **2017**, *42*, 12997–13010. [[CrossRef](#)]
286. Huang, L.; Peng, F.; Wang, H.; Yu, H.; Li, Z. Preparation and Characterization of Cu<sub>2</sub>O/TiO<sub>2</sub> Nano-Nano Heterostructure Photocatalysts. *Catal. Commun.* **2009**, *10*, 1839–1843. [[CrossRef](#)]
287. Muscetta, M.; Andreozzi, R.; Clarizia, L.; Di Somma, I.; Marotta, R. Hydrogen Production through Photoreforming Processes over Cu<sub>2</sub>O/TiO<sub>2</sub> Composite Materials: A Mini-Review. *Int. J. Hydrog. Energy* **2020**, *45*, 28531–28552. [[CrossRef](#)]
288. Zhai, Q.; Xie, S.; Fan, W.; Zhang, Q.; Wang, Y.; Deng, W.; Wang, Y. Photocatalytic Conversion of Carbon Dioxide with Water into Methane: Platinum and Copper (I) Oxide Co-Catalysts with a Core-Shell Structure. *Angew. Chem. Int. Ed.* **2013**, *52*, 5776–5779. [[CrossRef](#)]
289. Xiong, Z.; Lei, Z.; Kuang, C.-C.; Chen, X.; Gong, B.; Zhao, Y.; Zhang, J.; Zheng, C.; Wu, J.C.S. Selective Photocatalytic Reduction of CO<sub>2</sub> into CH<sub>4</sub> over Pt-Cu<sub>2</sub>O TiO<sub>2</sub> Nanocrystals: The Interaction between Pt and Cu<sub>2</sub>O Cocatalysts. *Appl. Catal. Environ.* **2017**, *202*, 695–703. [[CrossRef](#)]

290. Sinatra, L.; LaGrow, A.P.; Peng, W.; Kirmani, A.R.; Amassian, A.; Idriss, H.; Bakr, O.M. A Au/Cu<sub>2</sub>O–TiO<sub>2</sub> System for Photocatalytic Hydrogen Production. A pn-Junction Effect or a Simple Case of in Situ Reduction? *J. Catal.* **2015**, *322*, 109–117. [[CrossRef](#)]
291. Cheng, W.-Y.; Yu, T.-H.; Chao, K.-J.; Lu, S.-Y. Cu<sub>2</sub>O-Decorated Mesoporous TiO<sub>2</sub> Beads as a Highly Efficient Photocatalyst for Hydrogen Production. *ChemCatChem* **2014**, *6*, 293–300. [[CrossRef](#)]
292. Zhen, W.; Jiao, W.; Wu, Y.; Jing, H.; Lu, G. The Role of a Metallic Copper Interlayer during Visible Photocatalytic Hydrogen Generation over a Cu/Cu<sub>2</sub>O/Cu/TiO<sub>2</sub> Catalyst. *Catal. Sci. Technol.* **2017**, *7*, 5028–5037. [[CrossRef](#)]
293. Choi, J.; Song, J.T.; Jang, H.S.; Choi, M.-J.; Sim, D.M.; Yim, S.; Lim, H.; Jung, Y.S.; Oh, J. Interfacial Band-Edge Engineered TiO<sub>2</sub> Protection Layer on Cu<sub>2</sub>O Photocathodes for Efficient Water Reduction Reaction. *Electron. Mater. Lett.* **2017**, *13*, 57–65. [[CrossRef](#)]
294. Majeed, I.; Nadeem, M.A.; Badshah, A.; Kanodarwala, F.K.; Ali, H.; Khan, M.A.; Stride, J.A.; Nadeem, M.A. Titania Supported MOF-199 Derived Cu–Cu<sub>2</sub>O Nanoparticles: Highly Efficient Non-Noble Metal Photocatalysts for Hydrogen Production from Alcohol–Water Mixtures. *Catal. Sci. Technol.* **2017**, *7*, 677–686. [[CrossRef](#)]
295. Uddin, M.T.; Nicolas, Y.; Olivier, C.; Jaegermann, W.; Rockstroh, N.; Junge, H.; Toupance, T. Band Alignment Investigations of Heterostructure NiO/TiO<sub>2</sub> Nanomaterials Used as Efficient Heterojunction Earth-Abundant Metal Oxide Photocatalysts for Hydrogen Production. *Phys. Chem. Chem. Phys.* **2017**, *19*, 19279–19288. [[CrossRef](#)]
296. Chen, C.-J.; Liao, C.-H.; Hsu, K.-C.; Wu, Y.-T.; Wu, J.C.S. P–N Junction Mechanism on Improved NiO/TiO<sub>2</sub> Photocatalyst. *Catal. Commun.* **2011**, *12*, 1307–1310. [[CrossRef](#)]
297. Chen, J.; Wang, M.; Han, J.; Guo, R. TiO<sub>2</sub> Nanosheet/NiO Nanorod Hierarchical Nanostructures: P–n Heterojunctions towards Efficient Photocatalysis. *J. Colloid Interface Sci.* **2020**, *562*, 313–321. [[CrossRef](#)]
298. Teter, D.M.; Hemley, R.J. Low-Compressibility Carbon Nitrides. *Science* **1996**, *271*, 53–55. [[CrossRef](#)]
299. Xu, Y.; Gao, S.-P. Band Gap of C<sub>3</sub>N<sub>4</sub> in the GW Approximation. *Int. J. Hydrog. Energy* **2012**, *37*, 11072–11080. [[CrossRef](#)]
300. Zheng, Y.; Lin, L.; Wang, B.; Wang, X. Graphitic Carbon Nitride Polymers toward Sustainable Photoredox Catalysis. *Angew. Chem. Int. Ed.* **2015**, *54*, 12868–12884. [[CrossRef](#)]
301. Wang, X.; Maeda, K.; Thomas, A.; Takanebe, K.; Xin, G.; Carlsson, J.M.; Domen, K.; Antonietti, M. A Metal-Free Polymeric Photocatalyst for Hydrogen Production from Water under Visible Light. *Nat. Mater.* **2009**, *8*, 76–80. [[CrossRef](#)]
302. Wang, A.; Wang, C.; Fu, L.; Wong-Ng, W.; Lan, Y. Recent Advances of Graphitic Carbon Nitride-Based Structures and Applications in Catalyst, Sensing, Imaging, and LEDs. *Nano-Micro Lett.* **2017**, *9*, 47. [[CrossRef](#)]
303. Acharya, R.; Parida, K. A Review on TiO<sub>2</sub>/g-C<sub>3</sub>N<sub>4</sub> Visible-Light-Responsive Photocatalysts for Sustainable Energy Generation and Environmental Remediation. *J. Environ. Chem. Eng.* **2020**, *8*, 103896. [[CrossRef](#)]
304. Wei, S.; Wang, F.; Yan, P.; Dan, M.; Cen, W.; Yu, S.; Zhou, Y. Interfacial Coupling Promoting Hydrogen Sulfide Splitting on the Staggered Type II G-C<sub>3</sub>N<sub>4</sub>/r-TiO<sub>2</sub> Heterojunction. *J. Catal.* **2019**, *377*, 122–132. [[CrossRef](#)]
305. Lin, Y.; Shi, H.; Jiang, Z.; Wang, G.; Zhang, X.; Zhu, H.; Zhang, R.; Zhu, C. Enhanced Optical Absorption and Photocatalytic H<sub>2</sub> Production Activity of G-C<sub>3</sub>N<sub>4</sub>/TiO<sub>2</sub> Heterostructure by Interfacial Coupling: A DFT+U Study. *Int. J. Hydrog. Energy* **2017**, *42*, 9903–9913. [[CrossRef](#)]
306. Zhou, B.-X.; Ding, S.-S.; Wang, Y.; Wang, X.-R.; Huang, W.-Q.; Li, K.; Huang, G.-F. Type-II/Type-II Band Alignment to Boost Spatial Charge Separation: A Case Study of g-C<sub>3</sub>N<sub>4</sub> Quantum Dots/a-TiO<sub>2</sub>/r-TiO<sub>2</sub> for Highly Efficient Photocatalytic Hydrogen and Oxygen Evolution. *Nanoscale* **2020**, *12*, 6037–6046. [[CrossRef](#)] [[PubMed](#)]
307. Sharma, K.; Sharma, V.; Sharma, S.S. Dye-Sensitized Solar Cells: Fundamentals and Current Status. *Nanoscale Res. Lett.* **2018**, *13*, 381. [[CrossRef](#)] [[PubMed](#)]
308. Zani, L.; Melchionna, M.; Montini, T.; Fornasiero, P. Design of Dye-Sensitized TiO<sub>2</sub> Materials for Photocatalytic Hydrogen Production: Light and Shadow. *J. Phys. Energy* **2021**. [[CrossRef](#)]
309. Chatterjee, D. Effect of Excited State Redox Properties of Dye Sensitizers on Hydrogen Production through Photo-Splitting of Water over TiO<sub>2</sub> Photocatalyst. *Catal. Commun.* **2010**, *11*, 336–339. [[CrossRef](#)]
310. Choi, S.K.; Yang, H.S.; Kim, J.H.; Park, H. Organic Dye-Sensitized TiO<sub>2</sub> as a Versatile Photocatalyst for Solar Hydrogen and Environmental Remediation. *Appl. Catal. B Environ.* **2012**, *121–122*, 206–213. [[CrossRef](#)]
311. Armaroli, N.; Balzani, V. Solar Electricity and Solar Fuels: Status and Perspectives in the Context of the Energy Transition. *Chem. Eur. J.* **2016**, *22*, 32–57. [[CrossRef](#)]
312. Warnan, J. Solar Electricity and Fuel Production with Perylene Monoimide Dye-Sensitized TiO<sub>2</sub> in Water. *Chem. Sci.* **2019**, *9*.
313. Manfredi, N.; Monai, M.; Montini, T.; Peri, F.; De Angelis, F.; Fornasiero, P.; Abboto, A. Dye-Sensitized Photocatalytic Hydrogen Generation: Efficiency Enhancement by Organic Photosensitizer–Coadsorbent Intermolecular Interaction. *ACS Energy Lett.* **2018**, *3*, 85–91. [[CrossRef](#)]
314. Watanabe, M. Dye-Sensitized Photocatalyst for Effective Water Splitting Catalyst. *Sci. Technol. Adv. Mater.* **2017**, *18*, 705–723. [[CrossRef](#)] [[PubMed](#)]
315. Huang, J.; Lei, Y.; Luo, T.; Liu, J. Photocatalytic H<sub>2</sub> Production from Water by Metal-free Dye-sensitized TiO<sub>2</sub> Semiconductors: The Role and Development Process of Organic Sensitizers. *ChemSusChem* **2020**, *13*, 5863–5895. [[CrossRef](#)] [[PubMed](#)]